A MOLECULAR DYNAMICS STUDY ON CEMENTITIOUS MATERIALS AND NANOCOMPOSITES

By

Ding Fan

A thesis Submitted to

University of Strathclyde

in Partial Fulfillment of the Requirement for

the Degree of Doctor of Philosophy

in Civil and Environmental Engineering

September 2018, Glasgow, United Kingdom

Declaration of Authenticity and Author's Rights

This thesis is the result of the author's original research. It has been composed by the author and has not been previously submitted for examination which has led to the award of a degree.

The copyright of this thesis belongs to the author under the terms of the United Kingdom Copyright Acts as qualified by University of Strathclyde Regulation 3.50. Due acknowledgement must always be made of the use of any material contained in, or derived from, this thesis.

Signed:

Date:

ACKNOWLEDGEMENT

I would first like to express sincere gratitude to my supervisor, Dr. Shangtong Yang, for his patient guidance and support through the period of doing this thesis. His knowledge and professional insights were of great help during this research.

I would also like to thank this friendly city, Glasgow. People make Glasgow, and Glasgow makes me. When I chose the university for my postgraduate study after I graduated from East China University of Science and Technology and Glasgow Caledonian University, Glasgow was my priority due to the attractive city and the friendly Scottish around me. It is my pleasure living here for five years and finishing this thesis in this city.

I would like to thank my colleagues at University of Strathclyde, including Zhiyuan Lin, Amy Romaniuk, Qianqian Jiang, Xun Xi and other friends in my department for their significant support to my research and life in Scotland. Particularly, thanks to Amy Romaniuk, who does the similar project with me and always gave me the best advice when I was struggling. I will remember and thanks all the best time we spent in Glasgow, Manchester, highland and Switzerland in my future life.

Thanks to Houston Rockets, the best basketball team I have loved from my childhood. Congratulations to James Harden for being the MVP in season 2017/2018. I have undergone all your losing and winning games during my PhD, and it is my pleasure to accompany the great 2017/2018 season in Houston history. It is my time now to share my delight with you at the end of my PhD. CHAMPIONSHIP HOUSTON ROCKETS!

Significantly, I would like to give my love and gratitude to my parents. They spent all their effort supporting me whatever the things went up or down during my whole life, especially during my PhD. I could not imagine I could reach this far without their

encouragement and support. I will do my best to return all my happiness to my family in my future life.

Finally, partial financial support from the European Commission Horizon 2020 Marie Sklodowska-Curie Research and Innovation Staff Exchange scheme through the grant 645696 (i.e. REMINE project) is gratefully acknowledged.

ABSTRACT

Cementitious materials, including cement composites, are the most used construction material in the world. With the development of nanotechnology in the last several decades, the properties of cementitious materials can be significantly improved by adding nanomaterials such as nanoparticles, nanofibers, nanotubes and graphene-based materials. Graphene oxide (GO) has been widely accepted as an ideal candidate in increasing various properties of cement, i.e., strength, toughness, durability, electrical conductivity etc. However, the strengthening mechanism and some fundamental behavior of this cementitious nanocomposite are still not very clear. Therefore, this thesis aims to carry out a comprehensive study in understanding of the micro-mechanism of GO-cement, based on the recent developed realistic atomic structure of Calcium Silicate Hydrate (C-S-H) and Molecular Dynamics (MD) method. A critical review on the state-of-the-art of the properties and nanomechanics of cementitious materials and composites as well as molecular dynamics method is provided. The interfacial shear transfer mechanism between the GO sheet and C-S-H in the GO-cement nanocomposite is examined; also, the shear strength and shearing fracture properties are quantitatively determined. Moreover, the mechanical properties for the basic particle of C-S-H and the interfaces between the C-S-H particles, including Young's modulus, strength, fracture energy, are determined which are also affected by amount of water molecules. The enhancing mechanism by adding GO in cement is simulated by MD method; the overall strength and fracture properties for the GO-cement composite are calculated and the cracking bridging effect is studied. Furthermore, experiments about the global mechanical properties of GO-cement are conducted by the in-situ SEM three-point bending test. The overall increase of the mechanical performance of GO-cement is confirmed. This study presents novel and comprehensive understanding of the GO-cement from nanoscale to macroscale.

Table of Contents

List of Figures

List of Tables

List of Symbols

a	acceleration
A	area
kb	Boltzmann constant
BO	bond order
Δ	coordination definition
γ	Coulomb parameters
Λ	de Broglie thermal wavelength
α	degree of hydration
ρ	density
r	distance
λ	energy parameter in reaxff
Fi	force
fi	force vector
G_F	fracture energy
μ	friction coefficient
ΔE	interfacial interaction energy
m	mass
α	multiplication factor
U	potential energy
P	pressure
rh	relative humidity
τ	shear stress
q	signed magnitudes of the charges
T	temperature
σ	tensile strength
ξ	thermostat variable
t	time
Esystem	total energy of the system
V	volume

Chapter 1.
Introduction

1.1 Background

Cementitious materials are the most used construction materials in the world, which have vast application in different sectors of Civil Engineering. Since the invention of modern cement, there has been considerable mass of research carried out in improving cement characteristics in terms of toughness, strength and durability. To improve the performance of cement, a variety of inclusions have been utilised to enhance mainly the mechanical properties of the cementitious materials. Recently, due to the application of nanotechnology, a variety of nanomaterials have been added in cement for enhanced or optimal properties, such as metal oxide or silica (Chen et al., 2012), nanofibres (Onuaguluchi et al., 2014) and nanotubes (Siddique and Mehta, 2014). It has been shown that the nano-inclusions can significantly improve the performance of cement/concrete in compressive strength from 10% to 100%, flexural strength from 10% to 50%, Young's modulus from 14% to 75%, etc.

Since the first successful isolation of an individual Graphene sheet (Geim et al., 2007), Graphene has been considered as an ideal nano-inclusion in numerous materials including cement. Alkhateb et al. (2013) perhaps first investigated the enhancement effect of Graphene on cement. They have conducted X-ray diffraction and atomic force microscopy test on GO (Graphene-oxide)-cement and provided the first simple GO C-S-H (Calcium-Silicate-Hydrate) MD model. Meanwhile, Graphene oxide, the oxidized form of Graphene, has attracted more attention due to

high dispersible property. Moreover, the functional groups on the Graphene sheets can react with cement and thus form a stronger interface between these two materials. This will eventually increase the global mechanical performance for the composite. For example, GO cement at 28 days with 0.06 wt% of GO content can increase the compressive strength by 72.7% and 0.04 wt% of GO content can increase the flexural strength by 67.1% (Lv et al., 2014b). This has demonstrated that GO has significant potential in enhancing the mechanical properties of the cementitious materials.

Other than understanding the global mechanical enhancement of cementitious nanocomposites, researchers have also studied the interfacial mechanisms between cement and nano-inclusion (Van Aardt and Visser, 1975) at the micro-/nano-scale. Different from other nano-inclusions, the interfacial property between GO and cement plays an important role in terms of both physical and chemical actions. Different advanced experimental technologies have been used in understanding the microscale properties of the nanocomposites, e.g., SEM, X-ray Diffraction (XRD), atomic force microscopy (AFM), resonant ultrasound spectroscopy (RUS), etc (Alkhateb et al., 2013).

To model the microscale behaviour of the GO-cement composite, molecular dynamics simulation method provides a unique approach. The first MD model of C-S-H (the main binding phase of cement) was perhaps established by (Pellenq et al., 2009), presenting the complex structure of C-S-H. The model contains the molecular system

of C-S-H which enables calculation of stress and deformation states under loading. Moreover, more MD models for C-S-H itself have been established with different structures, force fields, etc. in last several years (Shahsavari et al., 2011, Wu et al., 2011, Hou et al., 2014c). However, there have been very few MD models on GO C-S-H composites, making proper analysis and design of GO-cement based materials a major challenge.

1.2 Research Significance

The concrete industry has become one of the two largest producers of carbon dioxide (CO_2), producing about 5-6% of worldwide man-made emissions of the greenhouse gas (Initiative, 2002). To produce stronger and tougher yet greener cement/concrete, it is necessary to have a better understanding of the material-property relationship of the cementitious materials, especially at the fundamental micro-/nano-scale. The combination of high aspect ratio, small size, low density, and unique physical and chemical properties of GO makes it perfect candidate for reinforcing the cement-based materials. Generally, cementitious material is treated as homogenous materials on the macroscale for its mechanical properties study, but it becomes much more complicated and heterogeneous on micro-/nano-scale. On nanoscale, cement paste is made of various components of C-S-H and other phases, which possess challenges for obtaining the mechanical properties on such a small scale. However, MD provides a unique insight into determining the mechanical behavior of materials

on the atomic scale. The elasticity, plasticity and fracture of the GO-cement can all be determined through MD modeling, all of which cannot be obtained from experimental test at the micro-/nano-scale so far. The mechanical properties derived can then be upscaled to macroscale engineering properties which can help the engineers and scientists control and accurately predict the structural performance of the cementitious materials.

1.3 Aim and Objectives

This study aims to investigate the mechanical properties of GO-cement nanocomposite and model the properties through molecular dynamics method. The specific objectives of this research are listed as follows:

- To critically review the state-of-the-art of cementitious nanocomposites including microstructures, methods and underlying factors.
- To develop a realistic model for the basic unit (particle) of cement, i.e., C-S-H, and determine the mechanical properties including Young's modulus, strength, fracture energy, and the interfacial properties between these basic units as affected by different amount of water molecules.
- To examine the interfacial shear transfer mechanism between the GO sheet and C-S-H in the GO-cement nanocomposite and to quantitatively determine the shear strength and shearing fracture properties.

- To simulate the enhancement mechanism of adding GO in cement by MD method, calculate the overall strength and fracture properties for the GO-cement and study the cracking bridging effects at the nanoscale.
- To investigate the global mechanical properties of GO cement by in-situ SEM micro three-point bending test and experimentally confirm the overall enhancement by adding GO into cement.

1.4 Outline of The Thesis

This thesis is structured in seven chapters. Chapter 1 is the introduction of the thesis. Chapter 2 presents the literature review. In Chapter 3, the shearing mechanism between GO and C-S-H is simulated and the shear properties are quantitatively determined. Chapter 4 shows the mechanics of C-S-H globules and their interfaces in between which are essential for mesoscale modelling. Chapter 5 provides MD study of the GO C-S-H structures with different layers of GO. Moreover, the experiments on GO-cement in terms of three-point bending tests are presented and discussed in Chapter 6. Chapter 7 is the conclusions of this thesis, together with recommended future study related to this topic.

Chapter 2.
Literature Review

In this Chapter, the state-of-the-art of cementitious nanocompsites is critically reviewed. It starts from the nanomaterials that are available to be added in cement to the nanostructures of the C-S-H and the GO C-S-H composite including their interfaces. It is then followed by the introduction of the molecular dynamics method. Finally, the current research work which has been done is presented and discussed.

2.1 Nano-inclusions in Cementitious Materials

Nano inclusions have been recently used in cement or cementitious materials to enhance a variety of properties. The properties of some typical inclusions for reinforcing cement are shown in Table 2.1.

Table 2.1 Properties of typical materials for reinforced cement

Material	Elastic Modulus (GPa)	Tensile Strength (GPa)	Elongation at break (%)	Density (Kg/m^3)	Diameter/ thickness (nm)	Surface area (m^2/g)	Aspect ratio	Sources
Graphene	1000	～130	0.8	2200	～0.08	2600	6000-600,000	Lee et al. (2008);Stankovich et al. (2006)
GO	23-42	～0.13	0.6	1800	～0.67	700-1500	1500-45,000	Zhu et al. (2010); Dikin et al. (2007)
Carbon nanotube	950	11-63	12	1330	15-40	70-400	1000-10,000	Yu et al. (2000); Peigney et al. (2001)
Carbon nanofibre	600	2-8.7	-	1400-1600	60-200	20-75	250-2000	Burton et al. (2011);
Polymeric fibre (Polypropylene and Nylon)	3-5	0.3-0.9	18	900	18,000-30,000	0.225	160-1000	Wang et al. (1990); Pelisser et al. (2010)
Glass fibre	72	3.45	4.8	2540	5000-10,000	0.3	600-1500	Benmokrane et al. (1995); Trens et al. (1996)
Steel fibre	200	1.50	3.2	7800	50,000-900,000	0.02	45-80	Yao et al. (2003); Yazıcı et al. (2007)

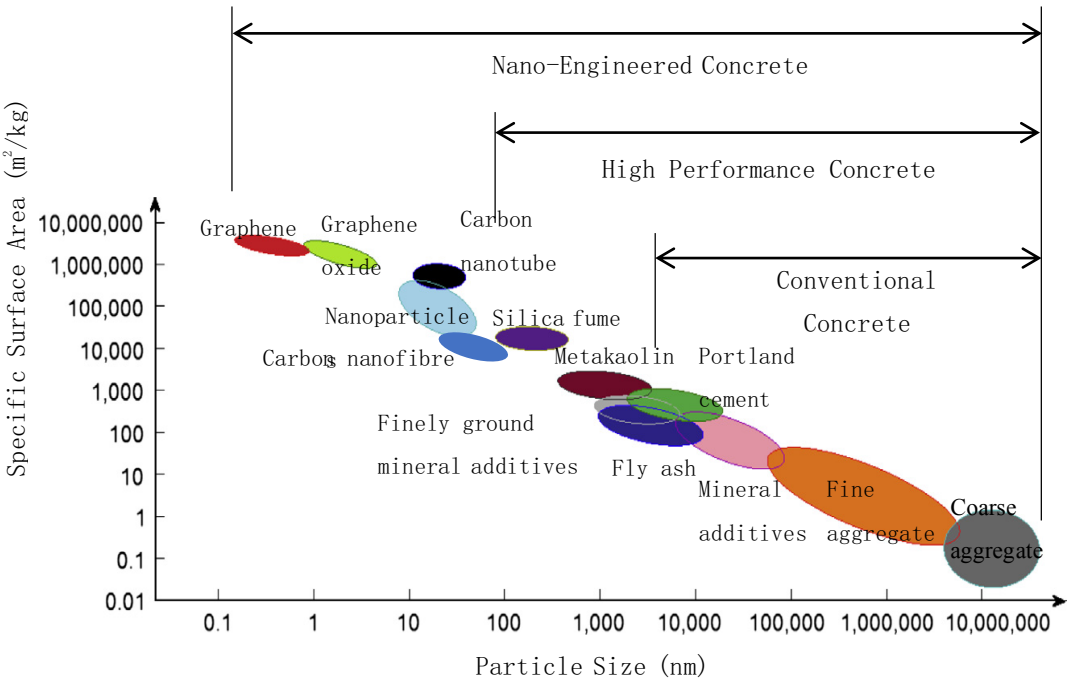

Figure 2.1 Comparison of nanomaterials with cementitious materials and aggregates in concrete. adapted from Chuah et al. (2014).

The properties of these materials, including elastic modulus and tensile strength, are much better than that of Portland cement. The tensile strength of cement is in the range of 2-8 MPa and elastic modulus in the range of 10-30 GPa (Raki et al., 2010). These materials contribute magnificently to the properties of concrete structures due to their significant elastic modulus or tensile strength. Other than the considerable properties, a big aspect ratio and great inherent strength are the preconditions for the enhancement of inclusion on cement. Developing after the mesoscale and macroscale materials of fibre-reinforced concrete, nanomaterials including nanoparticles, carbon nanotubes (CNTs) and GO began to show great capability on improving the properties of cement. The particle sizes of such nanomaterials compared to

cementitious materials are shown in Figure 2.1 Comparison of nanomaterials with cementitious materials and aggregates in concrete. adapted from Chuah et al. (2014).

Cement powder was identified as the best component to combine aggregates for concrete formation. However, the requirement of using cementitious materials containing fly ash and slag to improve the performance of concrete never stopped. With the recent and rapid development of nanotechnology and nanoscience of cement, the possibility of achieving high-performance concrete from enhancing the microscale of cement shows up. When it comes to nanotechnology of cement, the point of research focuses on C-S-H gel and the structure of cement hydrates, inclusions of nanomaterials (Raki et al., 2010) and interfacial properties. In this chapter, different types of nano-inclusion and their contribution to cement are listed.

2.1.1 Graphene

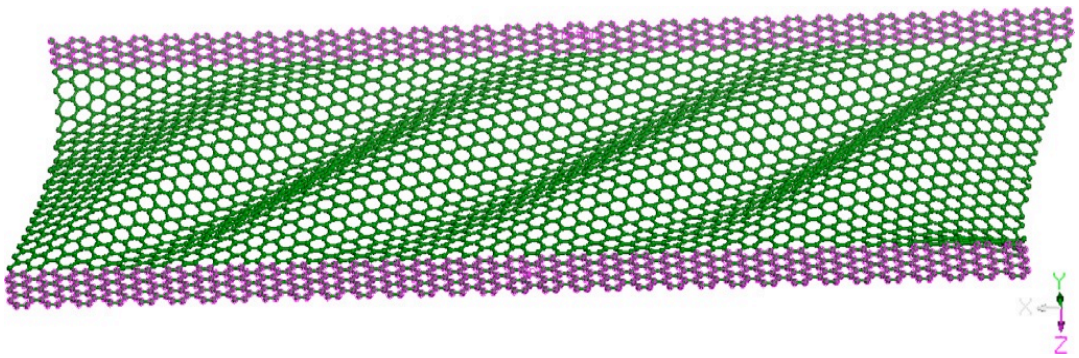

Figure 2.2 A rectangular zigzag graphene sheet modelled by Duan et al. (2011).

To be known as the strongest material in the world, Graphene was measured with a Young's Modulus of 1.0 TPa and intrinsic tensile strength of σ_{int} = 130 Gpa (Lee et

al., 2008) as a 2D-structure material presented in Figure 2.2, showing great potential in cement reinforcement on the microscale. Under such circumstances, Alkhateb et al. (2013) first performed several available experimental methods to assess the performance of Graphene nanoplatelets reinforcing cement. He focused on the materials genome, and the functionalized graphene platelets were dispersed by sonication in water to be examined the physical and chemical properties by atomic force microscopy (AFM) and the chemical composition by XRD. Furthermore, the

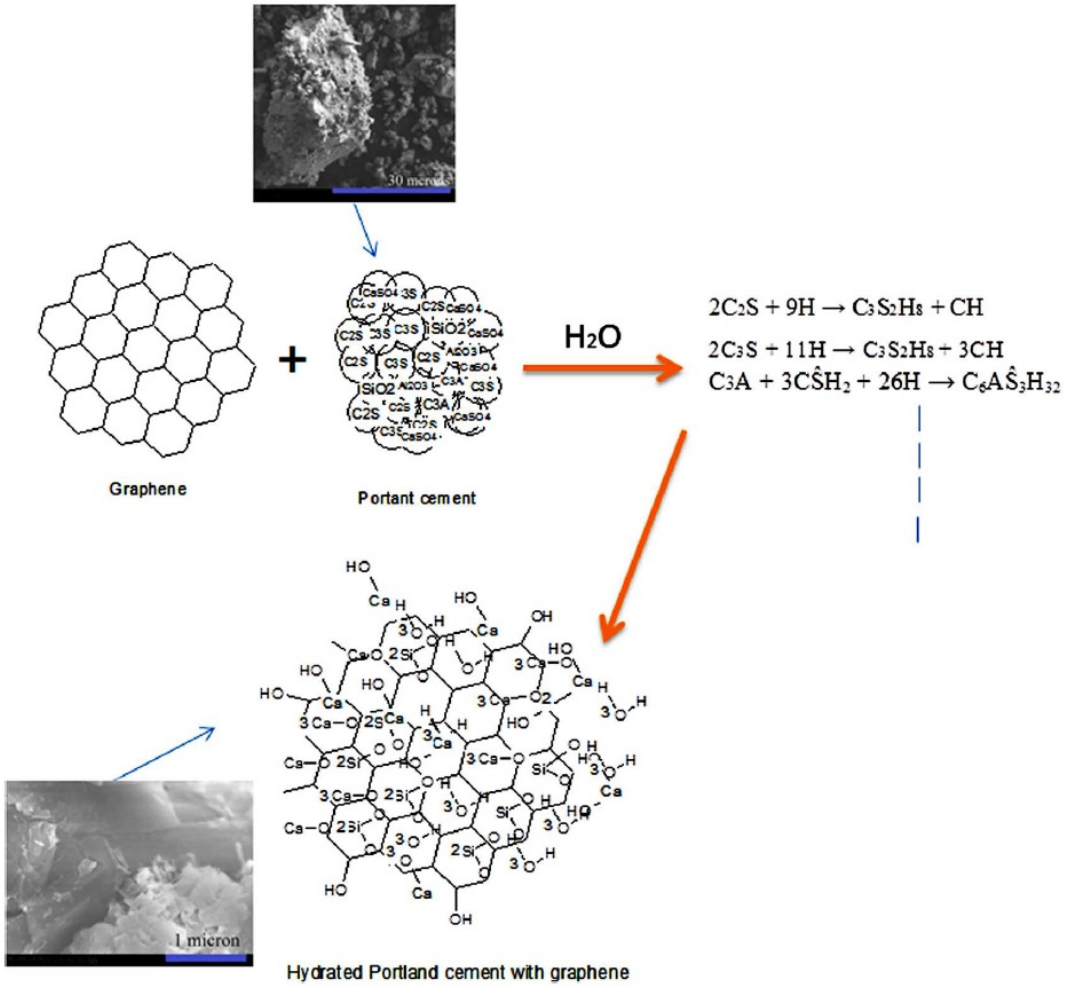

Figure 2.3 Schematic of possible hydrated graphene-cement nanocomposite structure stated by Sedaghat et al. (2014).

linear elastic properties of functionalized graphene reinforced cement were showed that Young's modulus of 22.8 Gpa and Shear modulus of 9.2 Gpa tested by Resonant Ultrasound Spectroscopy (RUS) outperformed pristine graphene reinforced cement of 19.7 Gpa and 8.1 GPa, as well as OPC of 18.5 Gpa and 6.7 Gpa. Although few results and pieces of evidence were contained, as a first research in the interface of graphene-reinforced cement, this paper provided a great start in this area and can lead further persuasive studies. Sedaghat et al. (2014) investigated the thermal diffusivity and electrical conductivity of hydrated graphene reinforced cementitious material with graphene/cement range from 0% to 10% and hydration temperature from 23℃ to 750℃, and with the increase dosages of graphene, the thermal diffusivity – temperature curve moved up along the thermal diffusivity axis, the resistivity reduced rapidly and conductivity increased exponentially. The findings also showed the improvement of graphene in the thermal properties of cement that graphene has potential in reducing thermal cracking in early age and enhancing durability on the macroscale. More details from XRD test and Rietveld analysis were presented in comparison to previous work, and the only drawback is the estimation of graphene-cement nanocomposite structure as shown in Figure 2.3.

2.1.2 Graphene Oxide

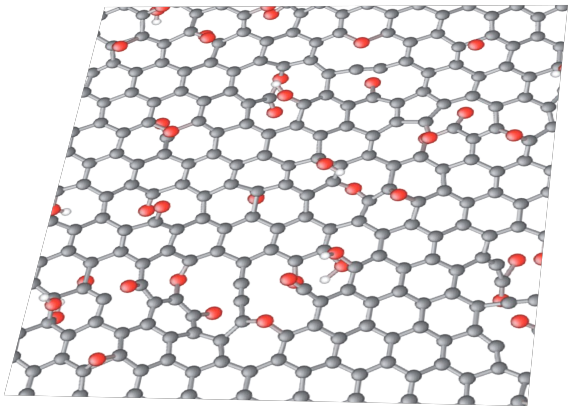

Figure 2.4 Model of graphene oxide stated by Bagri et al. (2010).

With a binding with carbonyl, epoxide, carboxyl and hydroxyl groups structure based on graphene as shown in Figure 2.4, graphene oxide can highly dispersible in water and present hydrophilic characteristic (Qiu et al., 2010). Compared to CNTs, graphene oxide has a larger surface area for C-S-H gel nucleation (Gong et al., 2014). Therefore, the inherent physical and chemical characteristics give graphene oxide so great potential that it can reinforce cement with reaction to C-S-H gel. With the reduction in mechanical properties possibly affected by the functionalized groups, graphene oxide performs a lower Young's modulus and tensile strength compared to graphene, which is Young's modulus of 32 Gpa and tensile strength of 130 Mpa still supply strong reinforcement to cement.

An early investigation made by Babak et al. (2014) showed that 1.5% content of ultrasonic GO increases 48% in tensile strength in cement due to the perfect dispersion and disappeared aggregates. As an early basic research containing few evidences of the interfacial stress transfer, it still stated the strong water absorption of graphene-oxide effects hydration of cement a lot by a simple comparison of 2.0 wt% GO at w/c ratio of 0.4 and 0.5, which showed 24.7% increase in tensile strength at w/c ratio of 0.5. Gong et al. (2014) tested 0.03wt% GO with w/c ratio of 0.5 compared to OPC with w/c ratio of 0.5. With the simple comparison and basic experiments, the results that GO produced 40% increase in tensile strength, reduced porosity and reduced the workability are achieved. As a perfect experimental report, it lacks strict and critical method in nanoscale and interfacial properties of GO cement.

Lv et al. (2013) provided that GO, which was prepared by oxidization and ultrasonication, can regulate flower shape crystals in cement mortar with the GO/cement ratio range from 0.01% to 0.03% and polyhedron shape with the GO/cement ratio range from 0.04% to 0.05%, furthermore, the hydration crystals of 0.03% GO under the range of 1 day to 90 days were observed. With the possible schematic diagram of regulation mechanism, the principle of the forming regulation was explained clearly. Although the remarkable increase contributed by 0.03% GO in tensile strength comes to 78.6%, flexural strength comes to 60.7% and

compressive strength comes to 38.9% was tested, the relationship of reinforcement and form of cement mortar on nanoscale hasn't been mentioned. To obtain more details with effects of GO on the formation of cement during hydration, Lv et al. (2014a) critically observed GO cement morphology with the GO weight ratio range from 0.01% to 0.06%. The concrete morphology of GO cement provided the growth process and formation mechanism clearly on the microscale, and it stated the flower-like clusters formed at low GO dosage and polyhedral crystals formed at high GO dosage. Furthermore, Lv et al. (2014b) supplemented the results of storage modulus, loss modulus and dissipation factor to the former researches, which suggested GO provides enhancement in strength, toughness and resists to cracking.

In an early stage, Pan et al. (2015) observed 15-33% increase in compressive strength and 41-59% increase in flexural strength with 0.05 wt% of graphene oxide. Due to the rise in the production of C-S-H, the surface area rises with the addition of GO. Surprisingly, Horszczaruk et al. (2015) first presented an investigation on cement nanocomposites of GO with special details. With sonicated 3 wt% GO mixed in cement, this cementitious material was tested by Infrared, Raman and X-ray diffraction techniques, and the bonds of carbon - hydroxyl groups and carbon - carboxyl groups showed obvious gap referenced to OPC.

2.2 Microstructure of the GO-cement Interface

With the development of advanced experimental method including SEM, FTIR and XRD, the morphology and chemical composition of cementitious materials with such nanoinclusion like GO can be observed directly so that it provides the opportunity for further research in such composites.

2.2.1 Morphology

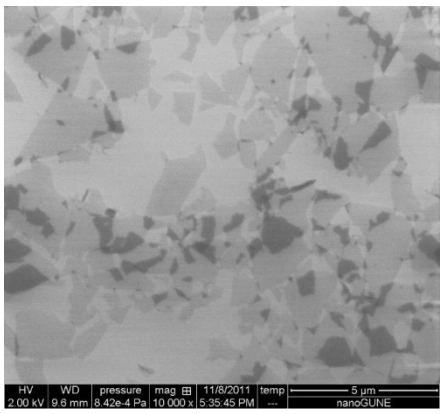

Figure 2.5 SEM image of Graphene oxide supplied by Graphenea

The morphology of a solid phase can be defined as its shape, form, or structure at the microscale, which is the scale of nanometres and micrometres (Jeff Thomas, 2008). The SEM image of Graphene Oxide sheets is shown in Figure 2.5 SEM image of Graphene oxide supplied by Graphenea . The morphology usually affects the properties on the macroscale more than the chemical composition of a particular material, which is appropriate for cement paste and cementitious materials. One of the significant parts in the microstructure of a pored material such as cementitious material is the morphology of the solid phases. The morphology of a specific solid phase is up to lots of causes containing the structure of crystals, forming mechanics,

temperature, and the space inside the material available for the phase to form or regular, which named are especially applicable to cementitious materials. Furthermore, the morphology of a solid phase can change over time in response to changes in its surrounding environment, as the period during hydration of a cement paste.

One of the primary reasons that the microstructure of cement is not precise or unpredictable is that the hydration of cement produces complex and extremely variable paste. The standard way to study composite materials is to break it down into individual stages or phases, then each isolated part is investigated. However, it is challenging to investigate cementitious materials due to the hydration process which impacts on the local factors and products different morphology of the phases on the surface. This is particularly characteristic of cementitious phase, which is by far the most critical hydration product.

With the sheet Graphene Oxide mixed in the cement, such cementitious composite shows an extraordinary transformation in its formation. Lv et al. (2014a) investigated the effect of GO on shapes of cement hydration crystals and their formation process with different dosages of GO nanosheets and 0.2% polycarboxylate superplasticiser for avoiding GO particle segregation. The SEM results showed that cement formed flower-like structures on the surface when the dosages of GO ranging from 0.01% to

0.04% and it formed polyhedral structures from rod-like crystals on the surface when the dosages of GO exceeded 0.05% shown as Figure 2.6.

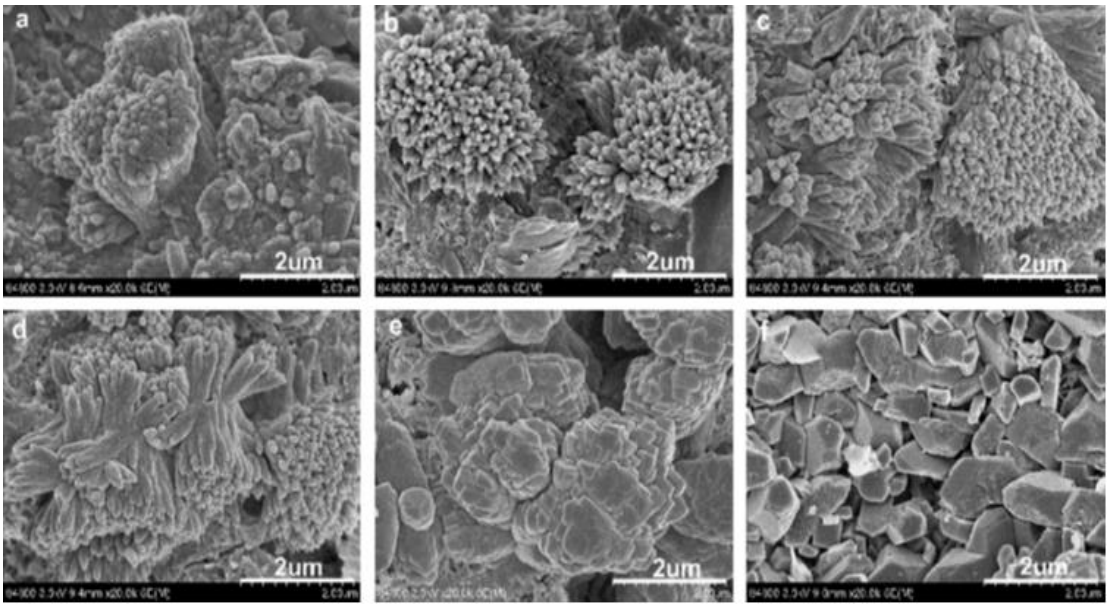

Figure 2.6 SEM images of hardened cement paste mixed with different dosages of GO nanosheets at 28 days: (a) GO 0.01%; (b) 0.02%; (c) 0.03%; (d) 0.04%; (e) 0.05%; and (f) 0.06% (w/c was 0.3 and PCs was 0.2% by weight of cement) (Lv et al., 2014a).

The flower-like crystal tended to be produced in the holes and cracks in the cement paste, filling the void and gap and forming network connections to a dense and cross-linked structure. It is evident that the flexural and compressive strength of cement paste are improved with the formation of such crystal.

2.2.2 Chemical composition

Cement gets its strength from chemical reaction mainly between the cement and water. The process is known as hydration. With GO added in cement, this process becomes more complicated that is best understood by first understanding the chemical composition of GO.

The chemical bonds and composition of graphite and graphite oxide were observed via FTIR spectra by Lv et al. (2014b) shown in Figure 2.7(a), including –OH, $–COO^{-}$, $–SO_3^{-}$ and –O– oxygen-containing groups, which are directed by the absorption peaks at 3300 cm^{-1} (–OH), 1735 cm^{-1} (–COOH), 1405 cm^{-1}, 1215 cm^{-1} and 1049 cm^{-1} (–O–), and 985 cm^{-1} ($–SO_3^{-}$). The FTIR spectrum of graphite shows absorption peaks at 1632 cm^{-1} (–C=C– double bond) and 1447 cm^{-1}, 1273 cm^{-1} and 1128 cm^{-1} (–C–C– single bond).

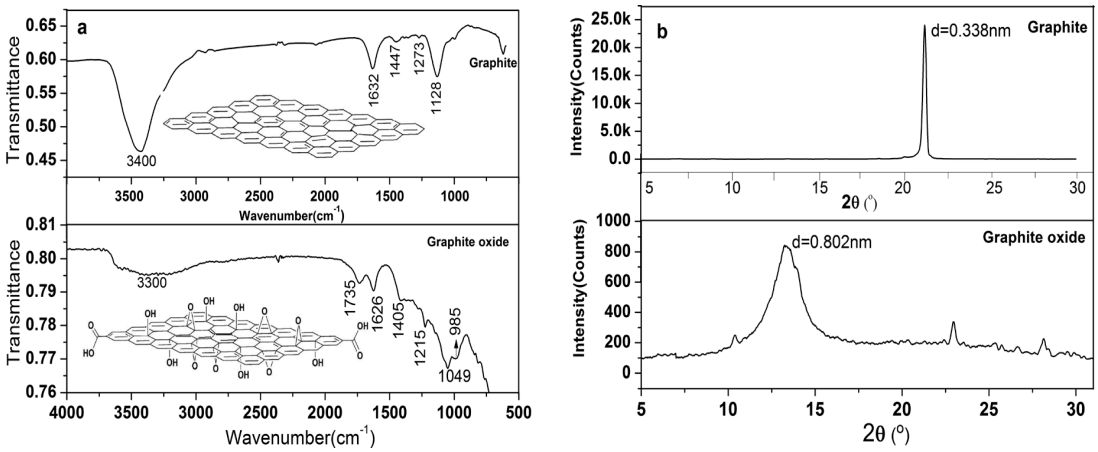

Figure 2.7 FTIR and XRD results of Graphene and Graphene Oxide provided by (Lv et al., 2014b).

The XRD results of the graphite and graphite oxide are shown in Figure 2.7(b), indicating that the interlayer distance in graphite oxide was expanded to 0.802 nm from 0.338 nm in graphite.

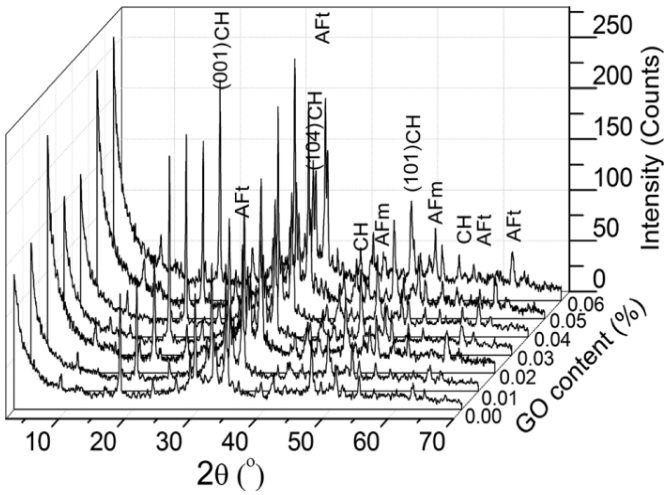

Figure 2.8 XRD results of GO cement with GO ranging from 0.00% to 0.06% (Lv et al., 2014b).

For the chemical composition of GO cement composite, XRD results of GO reinforced cement with different dosages of GO ranging from 0.00% to 0.06% by weight of cement are provided by Lv et al. (2014b) are shown in Figure 2.8. It can be seen that the intensity of the peaks increases with GO content increases. The rate of increase of the crystalline phases with increasing GO content is shown in Table 2.2. Calcium hydroxide, AFt and AFm increase with the dosage of GO is increasing. However, Lv et al. (2014a) provided neither many details on the reason of the increase in crystalline phases, nor the interaction between GO and these crystalline phases.

Table 2.2 Crystalline phases in cement with different dosages of GO.

GO content (wt/wt%)	Rate of increase of the crystalline phase (%)		
	CH	Aft	AFm

0.01	4.9	25.0	34.6
0.02	18.3	21.1	43.0
0.03	30.2	33.8	49.2
0.04	79.5	66.0	56.2
0.05	81.7	60.0	55.9
0.06	82.2	68.1	69.2

For the similar interaction as GO cement, the FT-IR spectrum of the acidified carbon nanotubes enhanced cement which produces the similar functionalized groups and bonds as GO cement composite presented by Li et al. (2005). Treated carbon nanotubes, treated carbon nanotubes reinforced cement (PCNT), carbon fibre reinforced cement (PCCF) and cement paste (PCC) are presented as curve 'a', 'b', 'c', 'd' of Figure 2.9, respectively. It is noteworthy that the peak at 1756 cm^{-1} in curve b (a positive shift of 22 cm^{-1} than the bands of CNTs, which corresponds the C=O bonds in carboxylic acids) shows the possible presence of carboxylate, while the disappearance of band at 3643 cm^{-1} (compared to the band in curve 'c' and 'd', which is OH^- of calcium hydroxide) shows the probable connection between COOH or C-OH groups in CNTs and calcium in calcium hydroxide. The shape from 1200 cm^{-1} to 400 cm^{-1} is quite different from that range of curve d, which indicates the C-S-H phases in PCNT are different from ones in PCC due to the interaction between the carboxyl and hydroxyl groups and C-S-H. This conclusion is based on the comparison of curve c and d. The appearance of bands at 3632, 3643, 3430, 1633, 1424, 977, 773, 678 and

457 cm^{-1} of PCCF, curve c, are similar to these of PCC, curve d, which indicates that no new phases form in PCCF.

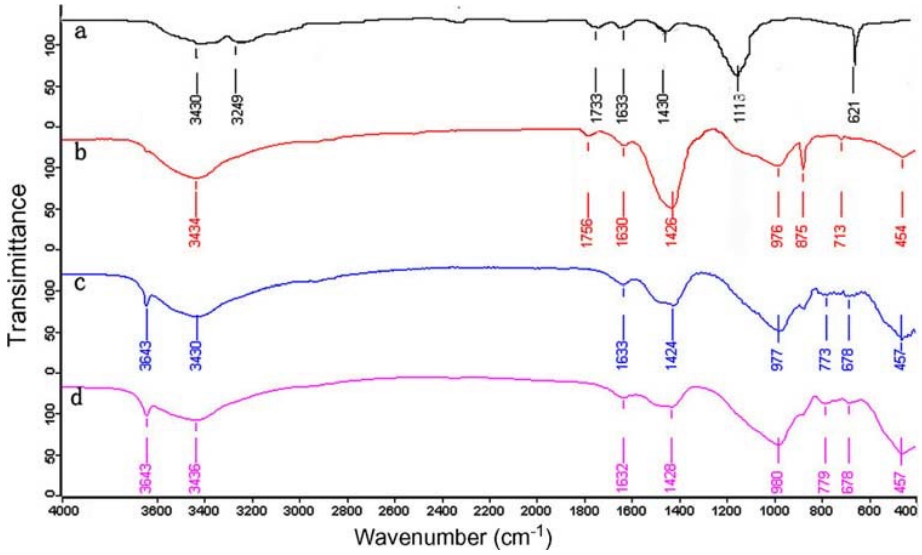

Figure 2.9 FTIR results of treated carbon nanotubes, treated carbon nanotubes reinforced cement, carbon fibre reinforced cement and cement paste (Li et al., 2005).

2.2.3 Nanostructure of GO Cement

Before studying GO cement nanostructure, the fundamental knowledge of nanostructure of GO, nanostructure of cement and their interface is the first thing to understand. As mentioned, when GO is oxidised from graphene, massive functional groups and deformations are generated on the basal graphene plane. Some original sp^2 carbon–carbon bonds are distorted by the reaction of functional groups which occupy the former carbon atoms a bit out of graphene plane forming an sp^3 hybrid carbon structure (Mkhoyan et al., 2009). Most sp^2 carbon bonds are still reserved and forming

a basal plane in GO, and the oxidised functional groups distribute both sides of the plane. However, the exact chemical structure of GO has been researched and debated for a long time, but there is no 'accurate' model has been defined (Dreyer et al., 2010).

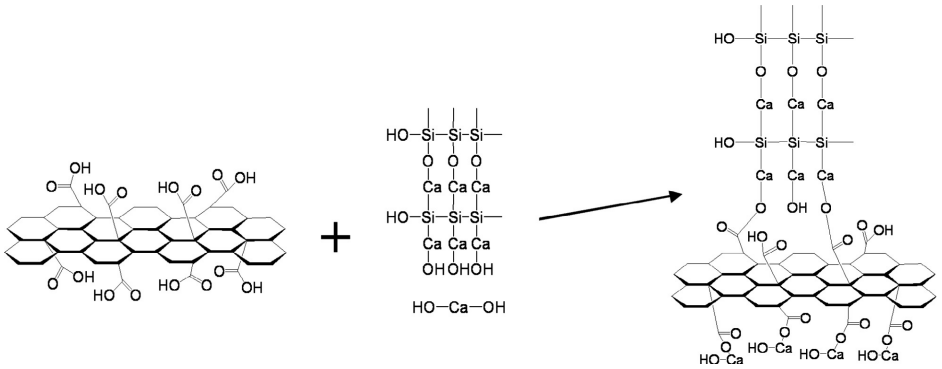

Figure 2.10 scheme of GO cement composite interface on nanoscale stated by Pan et al. (2015)

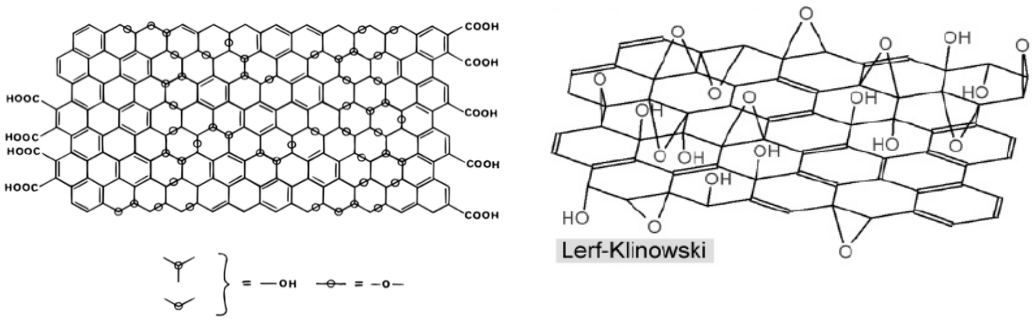

Figure 2.11 schematic of Lerf-Klinowski Graphene Oxide model.

Originally, GO models are presented as periodic, regular lattice structure. The earliest model proposed by Hofmann and Holst in 1939 consists of epoxy groups spreading across the basal plane with a general formula of C_2O (Hofmann and Holst, 1939). Ruess modifies this model in 1946 with hydroxyl group introduced into the lattice and modifies the hybridization of the basal plane to an sp^3 system which corrugates the GO

structure (Ruess, 1946). In 1957, Clauss and Boehm supplies GO structure with C=C bonds, ketone and enolic groups with carboxylic groups around the edges (Clauss et al., 1957). After a decade, Scholz-Boehm model corrugates carbon layers and removed the epoxide groups (Scholz and Boehm, 1969).

Yet most of the models have been displaced by a most recent model named by Lerf-Klinowski in 1998 (He et al., 1996, Lerf et al., 1998). Different from earlier models, Lerf-Klinowski model rejects the periodicity in the basal GO plane, and substitute with a nonstoichiometric amorphous due to distortions from the high fraction of cp^3 C-O bonds. The main functional groups attached to the basal plane consist of epoxy (C-O-C) and hydroxyl (C-OH) groups with carboxyl and carbonyl groups attached to the edges of the carbon structure, as shown in Figure 2.11. Further results achieved from nuclear magnetic resonance (NMR) experiment support this

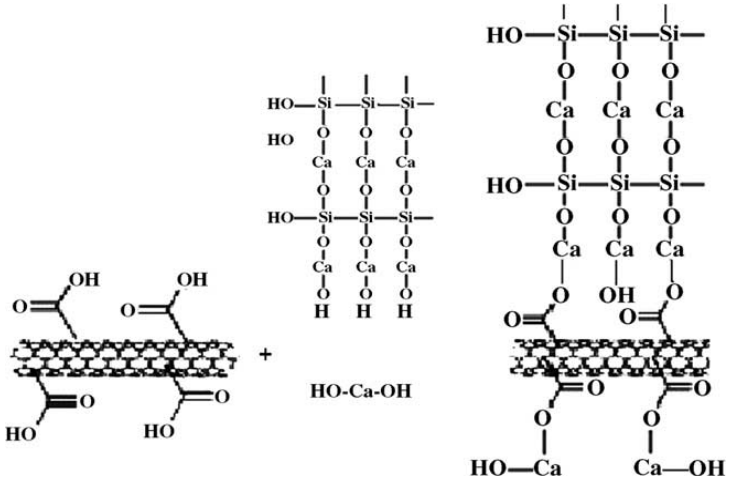

Figure 2.12 Scheme of treated carbon nanotube and cement interface on nanoscale stated by Li et al. (2005)

model make it become the most widely accepted GO model (Dreyer et al., 2010, Kim et al., 2010, Cai et al., 2008).

For the structure of GO cement, Pan et al. (2015) stated the scheme of GO reinforced cement shown in Figure 2.10. This scheme presents the interaction between hydration product of cement and Graphene Oxide to illuminate the significant enhancement of the cement matrix by GO. The oxygen in the carboxyl of GO acting as a connection between GO and calcium atoms in calcium silicate and calcium hydroxide by forming strong covalent bonds on the interface. This strong interfacial adhesion between C-S-H gel and GO increases the stress transfer efficiency from the cement matrix to GO sheets and cement matrix on the other side so that achieves the considerable improvement for the properties of cement matrix. This scheme is provided based on the previous work of acid-treated multi-walled carbon nanotubes reinforced cement shown as Figure 2.12 (Li et al., 2005).

For improving the reinforcement of carbon filaments on cement, a mixture of sulfuric acid and nitric acid is used to modify Multi-walled carbon nanotubes. After acidification, the multi-wall carbon nano tubes (MWCNTs) are given carboxyl functionalized groups, which provided a strong covalent force on the interface between the reinforcement and cement matrix in the composite. This chemical reaction takes place between the carboxyl groups and C-S-H or Calcium Hydroxide is presented by FT-IR analysis shown in Figure 2.9.

With the evidence of GO-cement interface shown in the chemical composition and this part, carboxyl and hydroxyl groups are reacting with C-S-H gel to form new interaction in the interface. The more understanding of the theory and scheme of GO and cement, the more exact model can be established to approach the real presentation of GO reinforced cement.

2.3 Calcium Silicate Hydrates (C-S-H)

C-S-H is main production of the hydration of Portland cement, and it is mainly responsible for the mechanical properties in cementitious materials. Different from the nanostructure of GO, the nanostructure of C-S-H not clear enough to achieve a straightforward structure so that it need to be provided from both direct and indirect study.

2.3.1 C-S-H gel

In this section, two main characteristics of C-S-H gel are reviewed, including Ca/Si ratio and water content.

2.3.1.1 C/S Ratio

Ca/Si ratio of C-S-H gel is one of the most important stoichiometric parameter, which defines different C-S-H phases. The C/S ratio of different C-S-H phases can be calculated by analysing the contents of calcium hydroxide and unreacted substances by analytical methods, e.g. thermos-gravimetric analysis, X-ray diffraction and TEM tests.

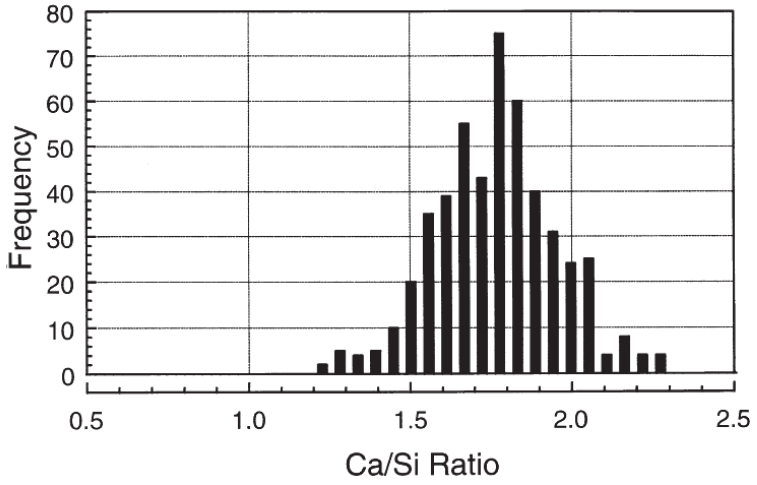

Figure 2.13 Ca/Si ratio frequency histogram for C-S-H in Portland cement pastes aged 1 day to 3 1/2 years (493 TEM microanalyses of C-S-H free of admixture with other phases) (Richardson, 1999).

The TEM result of C-S-H shows the frequency histogram of C/S ratio for X-ray microanalyses present hardened OPC pastes aged from one day to three and a half years is shown in Figure 2.13. A significant amount of data clarifies the possible value of C/S ratio in OPC pastes (hydrated at a temperature of 20 °C and W/C ratio is 0.4) from 1.2 to 2.3 with a mean value of 1.75. Furthermore, Richardson and Groves (1993) have verified the C/S ratio distributions change with C-S-H age that younger C-S-H in OPC presents a bimodal C/S ratio distribution and older C-S-H presents an uni-modal distribution, and Op C-S-H has a lower mean C/S ratio than Ip.

2.3.1.2 Water Content

It has been verified that water content in the C-S-H gel pore impacts the density of C-S-H relatively. The density of C-S-H is measured to be 2.604 Mg/m^3 by neutron

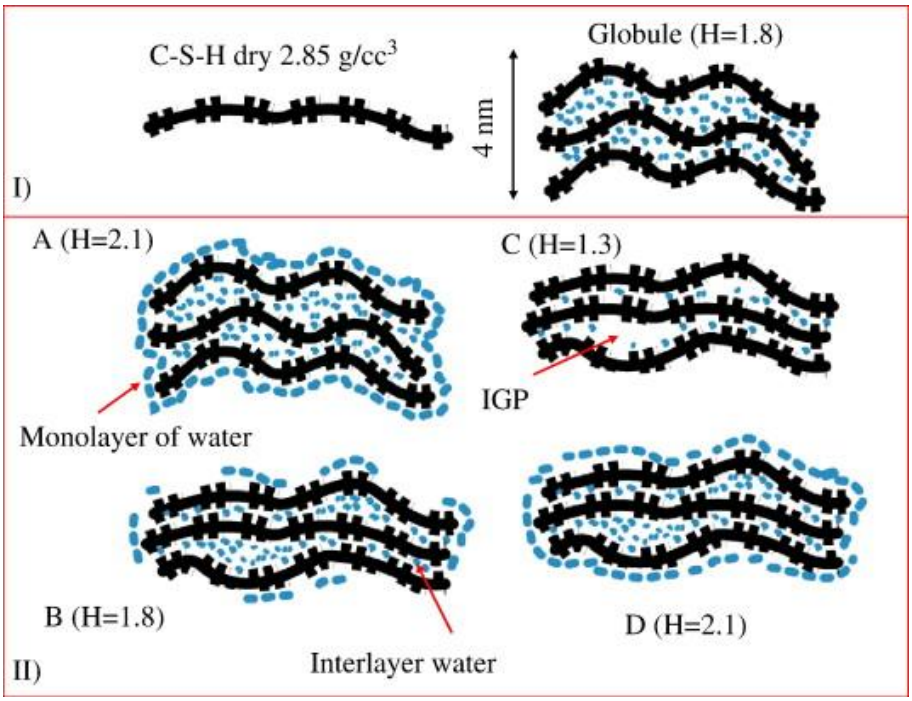

Figure 2.14 (I) Schematic of a C-S-H chain and a globule with water molecule (II) Schematic of a C-S-H globule with different water contents shows it is drying from 11% rh and rewetting to 11% rh (Jennings, 2008). H represents the H_2O/Si ratio.

and X-ray scattering with the chemical formula $C_{1.7}SH_{1.8}$(Allen et al., 2007), as a contrast, for the very first study of the density of d-dried C-S-H, the density of it is determined to be 2.85 Mg/m^3 by water pycnometry (Brunauer et al., 1958). Both values of density containing all the water molecules, both evaporable and non-evaporable within the C-S-H particles, but excluding the surface adsorbed water or the water molecules in the interface between C-S-H particles. An ideal testing method called ^1H nuclear magnetic resonance (NMR) is used to measure the porosity of C-S-H particles on nanoscale without any treatment before measurement such as drying the cement sample. Densification of C-S-H gel is an important characteristic

that C-S-H density is affected by both hydration degree (α) and w/c ratio, and it can be identified by NMR test that the "solid" density of C-S-H excluding of pore water decreases from ρ= 2.73 g/cm^3 at α≈ 0.4 to 2.65 g/cm^3 at α≈ 0.9, because the number of layers increases in the nano-crystalline aggregate, and "bulk" density, inclusive of gel pore water, increases from 1.8 g/cm^3 to 2.1 g/cm^3.

The evolution of C-S-H density for different water states is precise as shown in Figure 2.14 (Jennings, 2008). In section I, for the single layer of C-S-H without any water molecule, the density is 2.88 g/cm^3, while the density of C-S-H globule without water molecule on the surface is 2.602 cm^3. In section II, different samples of C-S-H gels with water molecules are listed. For model a, monolayer of water molecules are covered C-S-H globule and fill in both interlayer and IGP representing 11%rh. Partially evaporable water molecules then removed to characterize model b with density increases due to the reduction of monolayer water molecules. For model c, all the water molecules in the interlayer and on the surfaced are removed as d-dried state with density decreases. Model d represents the C-S-H globules with the water molecules added in again in the IGP and monolayer on the surface.

2.3.1.3 Mineral Analogues of C-S-H

There are two main mineral analogues which are known as Tobermorite and Jennite. These two mineral phases are introduced in details in this Section.

2.3.1.4 Tobermorite

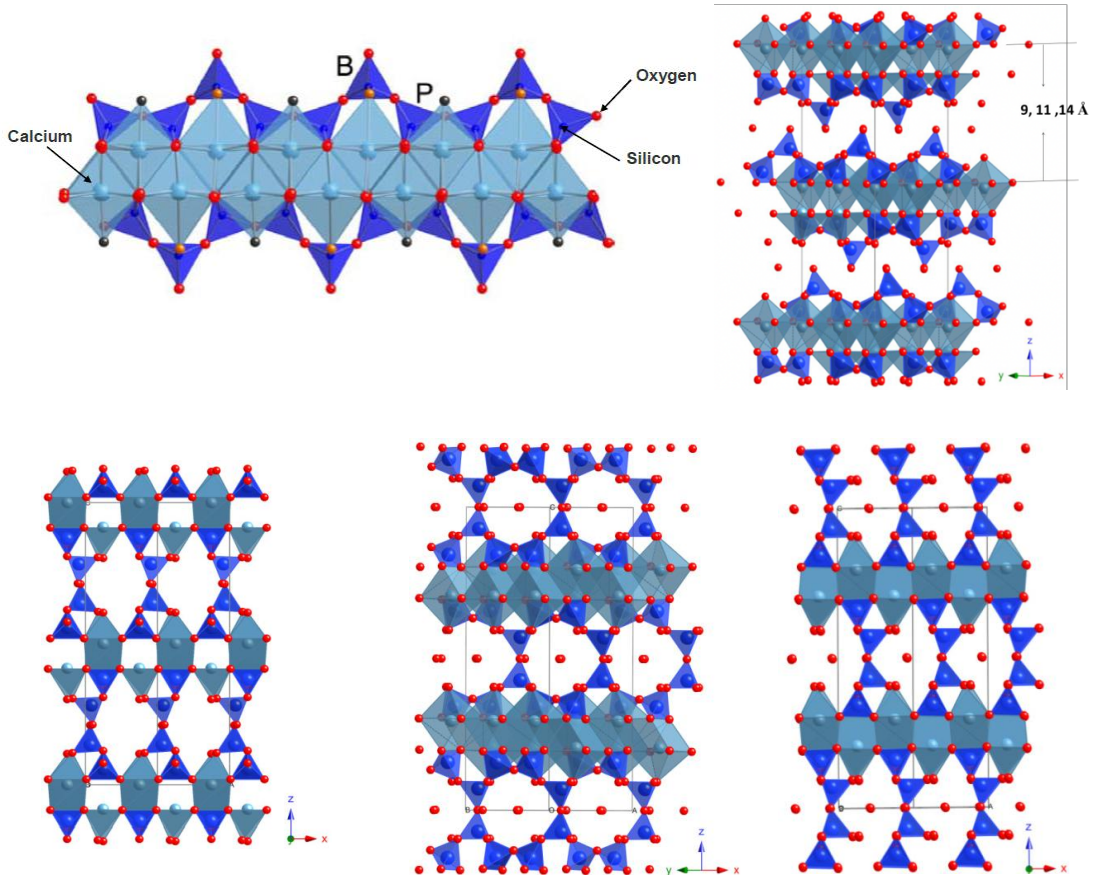

Figure 2.15 (a) A schematic of tobermorite layer presenting silicate chains sandwiching the Ca layer. And Hamid tobermorite 11 Å model along different directions: (b) [110] and (c) [010] Merlino tobermorite 11 Å model along different directions: (d) [110] and (e) [010] Red atom is oxygen, black atom is silicon, blue atom is calcium.

Tobermorite is a calcium silicate hydrate mineral that was first described in 1880 for an occurrence in Scotland, on the Isle of Mull. Different types of tobermorite are defined by the distance of two silicate layers: 9 Å, 11 Å or 14 Å Tobermorite, which depends on the different hydration degree (Shahsavari et al., 2009). The structure of

tobermorite is layered, e.g. 11 Å tobermorite is a layer composed of two layers of silicate chains sandwiching a calcium sheet. The structure of silicate chains in tobermorite is classified into Dreierketten chains as shown in Figure 2.15(a) that two paired tetrahedrons connected to Ca sheet and one tetrahedron is connected between the paired tetrahedrons are a bridge. Two closed silicate chains in different units are shifted by b/2 instead of linked head to head directly, while water molecules and calcium atoms can be placed in the interlayer. The Q_2 (Q_n means tetrahedrally coordinated Si atom with n=1, 2, 3, and 4 bridging oxygens) silicate chains are dominant, which is tested by NMR method, indicating the length of the silicate chain is infinite. Two different structures of 11 Å tobermorite are proposed that Hamid (1981) Å described 11 Å tobermorite as composed of independent layers and Merlino et al. (2001) announced 11 Å tobermorite is chemically bonded layers, which is the primary difference that one does not have the interlayer connection between two bridging tetrahedrons, but the other one has, as shown in Figure 2.15 (d),(f). While the calcium silicate backbone layer is structurally unchanged, Hamid tobermorite can have three different Ca/Si ratios, namely 0.67, 0.83 and 1 with chemical formula Ca_4 $[Si_6O_{14}(OH)_4].2H_2O$, Ca_5 $[Si_6O_{16}(OH)_2].2H_2O$ and Ca_6 $[Si_6O_{18}].2H_2O$. The Ca/Si ratio variation is caused by the adding the calcium atoms in the interlayer region; meanwhile, the protons in the hydroxyl groups should be removed to maintain the electronic neutrality. For tobermorite structure, the 2D

single silicate chain converter to 3D network structure by Q2 species changes to Q3 species. Moreover, multi-testing methods used to investigate thermal characteristics that tobermorite transformed by temperature: tobermorite 14Å turns into tobermorite 11 Å by heating to 80°C~100°C and further heating up to 300°C to turns into tobermorite 9 Å.

2.3.1.5 Jennite

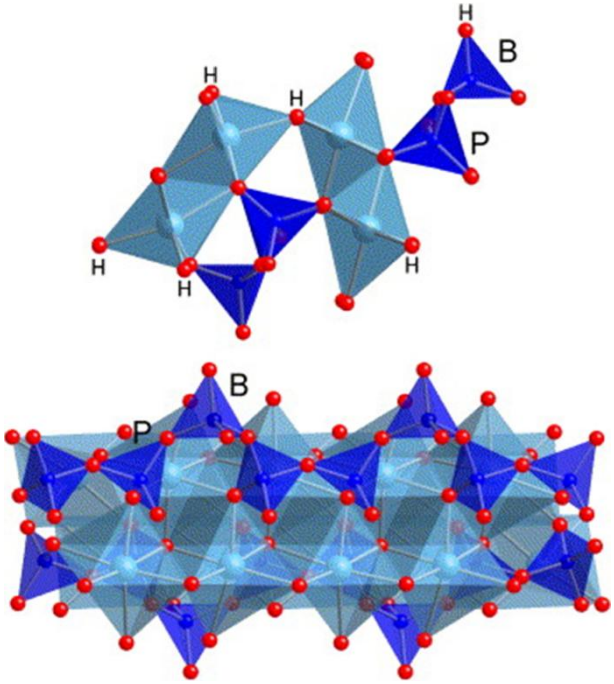

Figure 2.16 schematic diagram of jennite structure projected along [010] (top) and [100] (bottom). P is 'Paired' tetrahedron and B is 'bridging' tetrahedron

Jennite is a natural and rare silicate mineral analogous to C-S-H crystalline tobermorite which is suggested to be closely related to the structure of cement at late stages of hydration process (Taylor, 1966). ^{29}Si NMR indicates that it has single

silica chains with Ca/Si=1.5 (Komarneni et al., 1987), and Bonaccorsi et al. (2004) solved and defined the structure of jennite via single-crystal X-ray diffraction. Similar to tobermorite, jennite transforms into meta-jennite phase by heated and losses water. Different from tobermorite family, the bridging tetrahedral in the silica chain is connected to the calcium layer as shown in Figure 2.16. Similar to tobermorite, Ca^{+2} ion in the interlayer counterbalances the negatively charged layers in jennite. The chemical formula of jennite is $Ca_9Si_6O_{18}(OH)_6 \cdot 8H_2O$. The C/S ratio of jennite is about 1.5, which is higher than it in tobermorite and closer to the mean C/S ratio of the hydrated cement.

2.3.2 Models

2.3.2.1 Mesoscale structure

For the aspects of the water content, density and surface area, Jennings C-S-H model

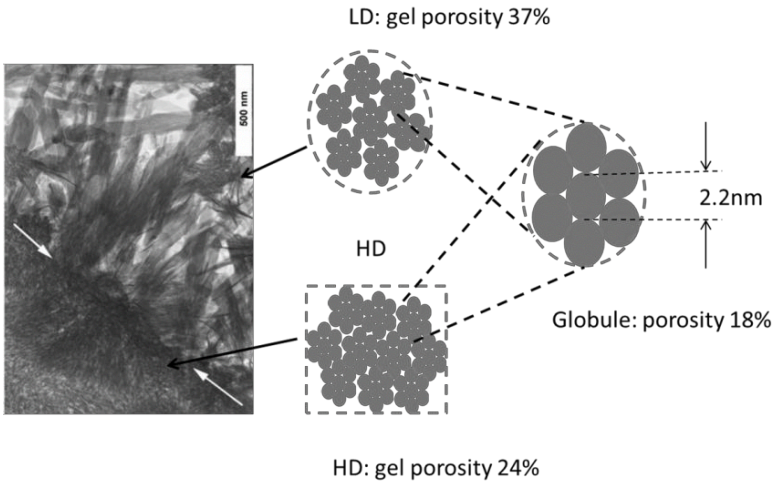

Figure 2.17 Schematic representation for the CM-I.

provides a comprehensive description of C-S-H gel (Jennings, 2000, Jennings, 2008). Jennings suggested that cement is composed of the C-S-H colloids on the nanoscale. The basic building unit is a colloid sphere with a diameter of 2.2 nm and density of 2.8g/cm^3. A more massive C-S-H globule is composed of seven agminate basic C-S-H units with a larger diameter of 5.6 nm, as shown in Figure 2.17. There are two main types of C-S-H gels in cement: high density (HD) and low density (LD), which has the porosity of 24% and 37% respectively, as a result of different effects on the package of the basic C-S-H units. The morphology of cement shown in Figure 2.17 presents the noodle-like outer products and dense inner composites, which can be regarded as the LD and HD phases. This distributes another view of cement research that it explains the contradictory results of surface area from other studies.

These two phases also demonstrate discrepancy in mechanical properties. Later Ulm performed extensive nano-indentation tests on different cement paste and the bimodal distribution of the elastic properties proved the presence of LD and HD phases of C-S-H gel (Constantinides and Ulm, 2004). But Ulm pointed that the packing efficiencies for two phases are 74% and 64%, which are corresponding to maximum for the sphere packing and closed-packed random packing respectively.

To improve the inner structure of the building block, Jennings took into consideration the layer molecular structure of tobermorite and Jennite and modified the basic building units. The density of globule (2.604g/cm^3) and the average

chemical composition of C-S-H ($C_{1.7}SH_{1.8}$) were achieved from the SANS and SAXS tests (Allen et al., 2007). As shown in Figure 2.18, the C-S-H is treated as an assembly of brick-shaped globules with a cross-section of 5nm rather than the sphere colloid.

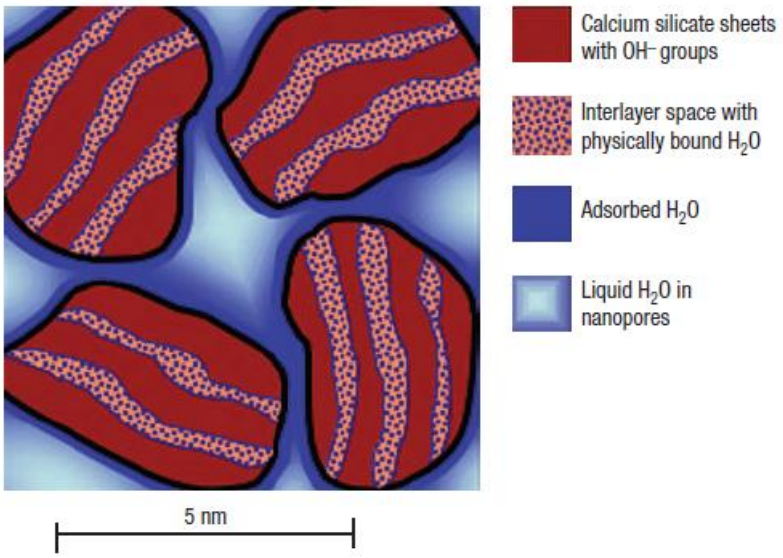

Figure 2.18 Schematic diagram for the CM-II model (Allen et al., 2007)

According to different humidity, the C-S-H globule can be distinguished into four states: the fully saturated globule with monolayer; partially saturated globule; saturated without monolayer water; d-dried state with evaporated water removed. These globules pack together and between the globules exist different spaces: the intra-globule spaces (IGP), the small gel pores (SGP), and the large gel pores (LGP), which have been discussed in section water and C-S-H density.

2.3.2.2 Atomic structure

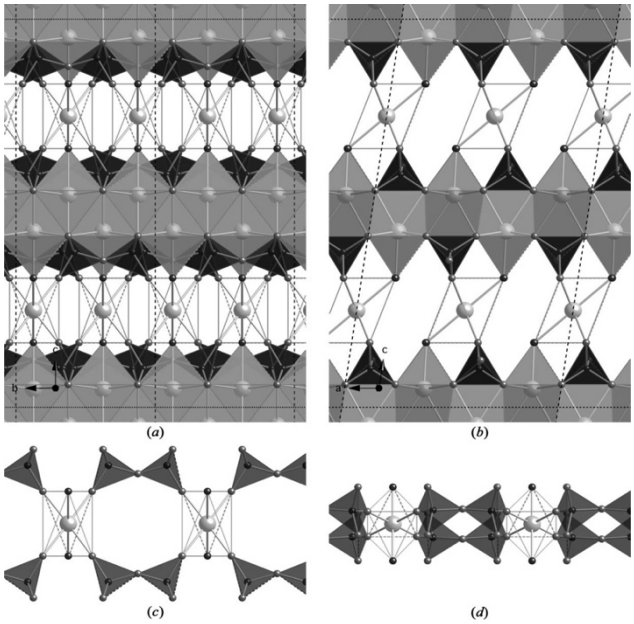

Figure 2.20 A hypothetical dimer derived from a clinotobermorite named in T2_ac. (a) a axis view. (b) b axis view (c) (d) The relationship of interlayer Ca with silicate tetrahedra

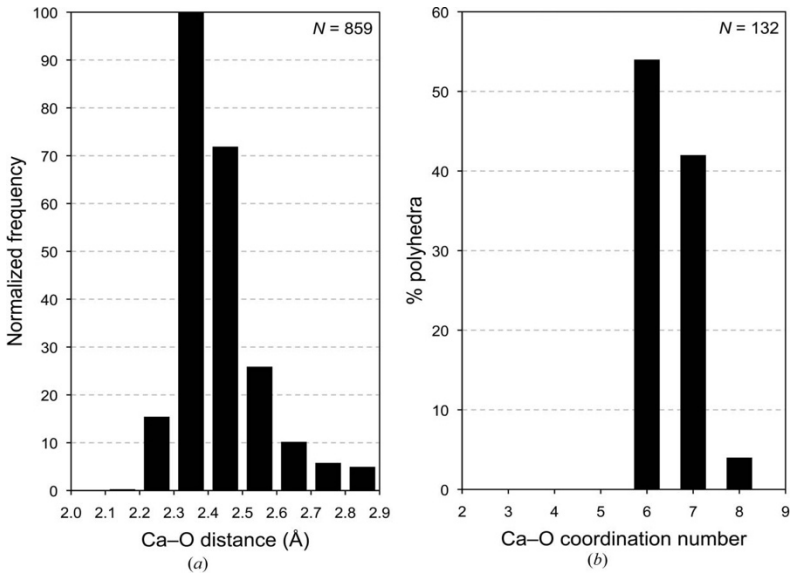

Figure 2.19 (a) Normalized frequency histogram for Ca-O distances presented in 35 crystalline C-S-H phases structures. (b) Histogram that shows the percentage of the Ca atoms in these phases that are coordinated to different numbers of O atoms.

Model structures for C-(A)-S-H(I) were supplied by Richardson (2014), which is a structurally imperfect form of 14 Å tobermorite that has variable composition and length of (alumina)silicate anions. Based on the results from ^{29}Si NMR data, it shows that there are no interlayer calcium ions when the silicate chains are of an infinite length, and that one is added for each tetrahedral 'bridging' site that is vacant. None of the C-S-H structural models for a dimer is started with an orthotobermorite structure. An indispensable index for C-S-H model is the Ca-O coordination number

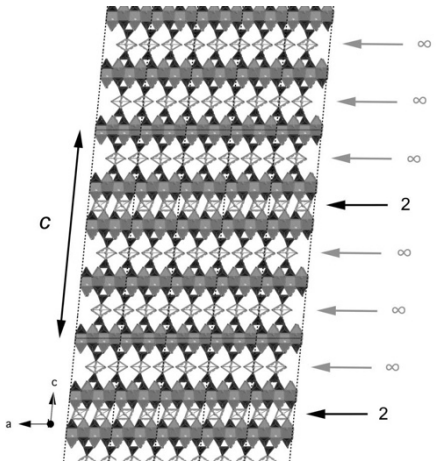

Figure 2.21 View along b axis of a hypothetical 'undecamer' derived from a staggered-chain clinotobermorite named T11_14sc.

is provided as well shown in Figure 2.19 that none of the Ca atoms in all the C-S-H phases in real consequences have the coordination to oxygen atoms less than six, which happens in some C-S-H MD structures.

Two of the C-S-H models are shown in Figure 2.20 and Figure 2.21. T2_ac is a double-chain Tobermorite-based monoclinic structure, derived from Merlino et al.

(2000) in which all the interlayer Ca atoms are in octahedral coordination with oxygen atoms in silicate chains. T11_14sc is also a Tobermorite-based monoclinic structure but the mean length of silicate chains is 11 Å, and the layer spacing is 14 Å.

2.4 Molecular Dynamics (MD) method

Based on the understanding of GO and cement nanostructure, it is possible to build the realistic models of C-S-H or GO C-S-H. For describing the physical movement of atoms in a given system during a period (Frenkel and Smit, 2001), Molecular dynamics is used as a perfect numerical computational tool to realise it.

MD is a method of computational physics which solves the classical n-body problem numerically in discrete time steps. Generally, a complete MD simulation needs three steps (Haile, 1992):

(1st) model an initiating start scenario

(2nd) compute the movements of the individual particles and

(3rd) analyse the simulation data for the desired physical properties.

It calculates the energy of a system by solving Newton's equations of motion:

$$m_i \ddot{r}_i = f_i \quad f_i = -\frac{\partial r_i}{\partial t} \tag{2-1}$$

and calculates the evolution in time of a system in a finite temperature as well. The physical properties depend on the location and velocities of particles, and MD requires starting structure, force field, and atom definition. Force field, also known as potential energy profile, is calculated from a classical potential function, $\Phi(r_{i1},r_{i2},...,r_{iN})$, which describes the potential energy of atom i in a system in terms of its position relative to all other atoms in the system. Here r_{ij} is a vector representing the separation between atoms i and j. This potential function in most cases contains fitting parameters which are fitted so that systems simulated using the potential represent a real material.

This potential function can be used to calculate the force acting on atom i:

$$F_i = \nabla\Phi\left(\sum_j r_{ij}\right) \tag{2-2}$$

The acceleration of atom i can be calculated from Newton's second law:

$$a_i = {}^{F_i}/_{m_i} = \frac{d^2 r_i}{dt^2} \tag{2-3}$$

Given the positions and velocities of a system of atoms, over a short timestep, Δt, this equation of motion can be integrated to calculate the new positions of atoms in the system at a time $t + \Delta t$.

The basic algorithm is as follows:

1. Calculate forces on each atom based on the potential function.

2. Integrate the equations of motion to calculate the positions and velocities of the atoms at time t + Δt. Now repeat from step 1.

Atoms could be approximated as classical particles as long as the de Broglie thermal wavelength (Yan, 2000), Λ, is small in comparison with the nearest neighbour distance in the system. The de Broglie thermal wavelength is:

$$\Lambda = \sqrt{\frac{2\pi h^2}{M k_B T}} \tag{2-4}$$

where M is the atomic mass and T is the temperature of the system. The classical potential approximation is valid for most materials, and Reaxff is used in this thesis.

2.4.1 Boundary

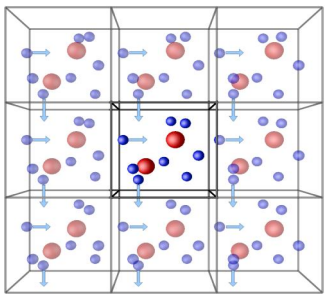

Figure 2.22 Schematic of a system with periodic boundary conditions.

To obtain the bulk propertied from MD simulations, it is essential to account for the edge effects. One way of eliminating these edge effects is to simulate an extensive system to ensure that the surfaces and edges have only a small influence on the properties. Due to computational expenses, this method is not feasible. The use of periodic boundary conditions facilitates the simulation of an infinitely large system

while being computationally efficient. The simulation box is replicated throughout space to form an infinite large system, as shown in Figure 2.22 (Le Roux and Petkov, 2010). During the simulation, when the position of a particle in one box is updated, this change is replicated on that particle in all the boxes. The edges of a simulation box containing a system of atoms are described by three vectors; a, b, and c. Periodic boundary conditions are imposed by replicating atoms in the system periodically. For any atom located at r in the system, the atom is replicated at locations ,r_{lmn}, given by:

$$r_{lmn} = r + la + mb + nc \tag{2-5}$$

where l, m, and n are integers in the range $[-\infty, +\infty]$. During simulating the atom present inside the simulation box moved towards one edge, it reappears from the opposite edge with same velocity.

If the potential function used is infinite ranged, then the number of pair interactions becomes infinite as any atom, i, in the simulated system will interact with an infinite number of images of another atom, j, in the central cell. To avoid having to compute an infinite number of atomic pair interactions, the following condition is implemented. Consider an atom, i, in the central cell. For each atom j (where $j \neq i$), atom i only interacts with one atom in the set [j,j_1,j_2,j_3,...], where j_1,j_2,j_3,... are periodic images of atom j. Out of the set [j, j_1,j_2,j_3,...], i interacts with the atom or image which it is closest to. This is known as the minimum image criterion. This criterion is often implemented by simply using a truncated or short ranged potential function with a limited range R_c.

As long as one is using a truncated potential and a square cell of length L, then the minimum image criterion is exact if $R_c < L/2$. Note that many types of potential function have infinite range in theory. For the simulations presented in this thesis, Reaxff is us ed.

2.4.2 Neighbour Lists

Since every of the n particles needs to interact with every other particle in a simulation step, there are

$$\binom{n}{2} = \frac{n(n-1)}{2} \in \mathcal{O}(n^2) \tag{2-6}$$

forces to be calculated. Especially for short range potentials with cut-off radii, $\mathcal{O}(n^2)$ inter-actions have to be checked, but only few of them actually make a contribution. Therefore, MD simulators usually implement a neighbour list strategy for these forces, i.e. a list of particles within the distance r_{neigh} (of e.g. $r_{neigh} = 2\ r_c$) is kept for every particle for some time-steps. The slower the interaction sphere of the particles move out of that radius r_{neigh}, the longer can the neighbour list be kept. Assuming a fixed r_{neigh} and that the macroscopic density of the particles has an upper bound, there can only be a limited number of particles within the neighbour list radius for each of the n particles, thus, reducing the complexity of pure force computation to $\mathcal{O}(n)$. While this consumes $\mathcal{O}(n)$ extra memory, it is of course a better method than the naive $\mathcal{O}(n^2)$ one for a sufficient large number of particles.

2.4.3 Potential Forms

Potential function acts as a significant role in MD simulations. The potential function calculates the force which is also the acceleration of each atom or particle, and it also turns back to determine the velocity and position of each atom or particle so that it is essential to make sure the potential function is appropriately defined and verified. Potential function is used to describe the interaction between atoms in an MD system by the assumption of mathematical descriptions. All the parameters in the potential function is achieved by quantum mechanical measurement and experimental data, and different kinds of MD systems can be defined by various potential functions.

Quantum mechanics (QM) based methods provide a better description of the interactions in a system with many particles. However, doing purely QM based calculations on a large system becomes computationally unfeasible. In order to reduce the fully quantum descriptions to a potential function description involves the Born-Oppenheimer approximation, which allows the energy of the system to be written as a product of mutually independent functions of nuclear and electron coordinates (Leach, 2001). Additionally, the nuclei of the atoms could be treated as point particles which follow Newtonian dynamics. In MD, the position and configuration of electrons within the shell of atoms are ignored and focus is entirely on the energy due to the position of nuclei with respect to each other. This facilitates the

use of MD to simulate large molecular systems. The molecular force fields employed in MD algorithm are in general empirical fits to quantum mechanical calculations. In certain cases the molecular dynamics algorithm is able to provide results as good as the highest quantum mechanical calculations, for a fraction of computer time (Leach, 2001).

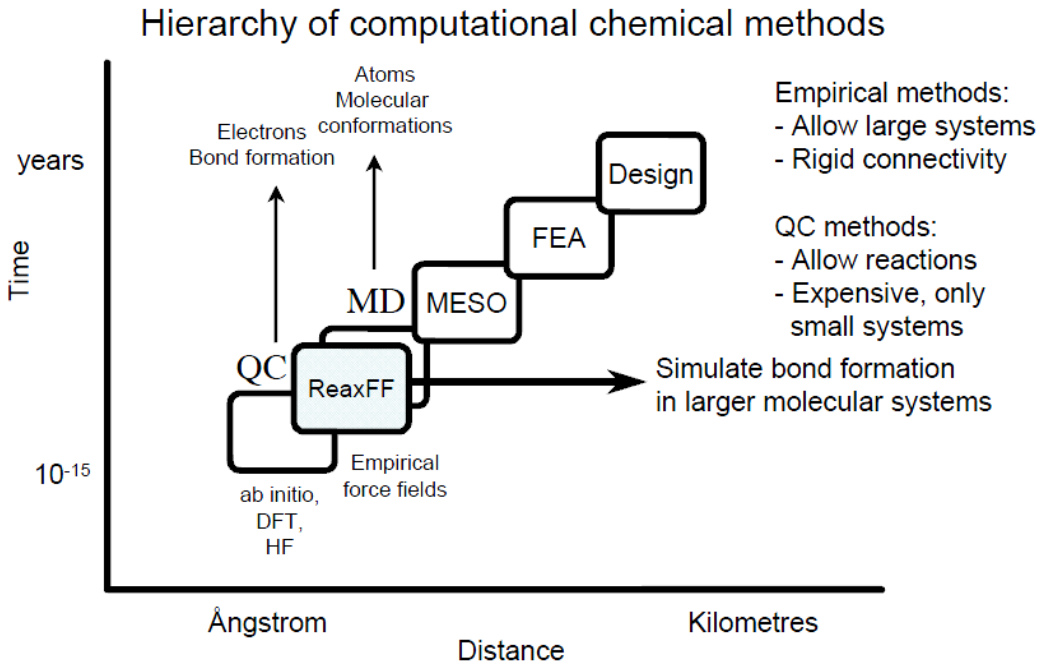

Figure 2.23 Position of ReaxFF in the computational chemical hierarchy (van Duin, 2003).

Most potential functions, also known as force fields, used are empirical in nature and consist of bonded (chemical bonds, bond angles, bond dihedrals) and non-bonded (van der Waals) interactions. Given that at least a weak non-bonded interaction exists between all the particles in the system, accounting for all those interactions could sometimes act as a bottleneck during MD simulations. Because of the predefined

bonding arrangements, they cannot model the chemical bond formation and breakage that occurs during the simulation. To overcome this shortcoming of the empirical potential functions, there exists another class of potential functions which are based on bond order. In this dissertation, one type of potential functions has been used, which is ReaxFF.

ReaxFF plays a role in bridging the gap between quantum chemical (QC) and empirical force field (EFF) based computational chemical methods (Figure 2.23). Even though QC methods are in general applicable to all chemical systems, regardless of connectivity, the computational expense makes them inapplicable for large systems with atoms more than 100. EFF methods describe the relationship between energy and geometry with a set of relatively simple potential functions. EFF methods describe molecular or condensed phase systems by simple harmonic equations that describe the stretching and compression of bonds and the bending of bond angles, usually augmented by van der Waals potential functions and Coulomb interactions to describe non-bonded interactions. Due to relative computational simplicity, the EFF force field is efficient in simulating the large system with millions of particles. EFF methods have been very successful in describing physical interactions in and between molecules and condensed phase systems. The force field obtained from the fitting procedure reduces its reliability as compared with the original QC description, which restricts the transferability of the EFF method. It is

the reason that these EFF methods cannot describe reactive systems, and in most cases the shape of the potential functions applied in these methods, like the aforementioned harmonic description of the bond length/bond energy relationship, would make it impossible to find parameter values that accurately describe bond energy towards the dissociation limit.

ReaxFF aims to provide a transferable potential, applicable to a wide range of chemical environments. To ensure its transferability, the following general guidelines have been adopted in its development:

1. No discontinuities in energy or forces, even during reactions.

2. Each element is described by just one force field atom type. The ReaxFF metal oxide oxygen is described by the same parameters as the ReaxFF oxygen in organic molecules.

3. No pre-definition of reactive sites is necessary using ReaxFF. Although it is possible to drive reactions using restraints, this is not required; given the right temperature and chemical environment reactions will happen automatically.

The Reactive force field provides an advanced description of the interaction between Ca, Si, O and H atoms in the C-S-H gel. The short-range interactions for the ReaxFF force field are determined by a bond length-bond order scheme so that the bonds can be broken and formed, with the potential energy transforming into a smooth state

(Brenner et al., 2002). On the other hand, the long-range coulombic interactions are determined by a 7th order taper function, with an outer cut off the radius of 10 Å. The Reactive Force field has been widely utilized in silica-water interfaces (Leroch and Wendland, 2012), calcium silicate hydrate gel (Manzano et al., 2013) and nano-crystals (Lau et al., 2010). The parameters of the force field for Ca, Si, O and H can be directly obtained from the table of the supporting information section.

Similar to empirical nonreactive force fields, the reactive force field divides the system energy up into various partial energy components (Van Duin et al., 2001):

$$E_{system} = E_{bond} + E_{over} + E_{under} + E_{lp} + E_{val} + E_{pen} + E_{tors} + E_{conj} + E_{vdwaals} + E_{coulomb} \quad (2\text{-}7)$$

, where E_{bond}, E_{over}, E_{val}, E_{tor}, $E_{vdWalls}$ and $E_{Coulomb}$ are general energy term used in all the ReaxFF system. The fundamental difference between ReaxFF and empirical force fields is that ReaxFF does not use fixed connectivity assignments for the chemical bonds. Instead the bond order, BO', is calculated directly from the instantaneous interatomic distances r_{ij} in Eq.2-8, which are updated continuously. This allows for the creation and dissociation of bonds during a simulation. The bond energy (E_{bond}) is determined solely from BO as in Eq.2-9. As the bond order BO turns to zero, the bond energy gradually transforms to zero, implying no discontinuity of the bond dissociation.

$$\mathrm{BO'}_{ij} = \mathrm{BO'^{\sigma}}_{ij} + \mathrm{BO'^{\pi}}_{ij} + \mathrm{BO'^{\pi\pi}}_{ij} = \exp\left[p_{bo,1}\left(\frac{r_{ij}}{r_0^{\sigma}}\right)^{p_{bo,2}}\right] + \exp\left[p_{bo,3}\left(\frac{r_{ij}}{r_0^{\pi}}\right)^{p_{bo,4}}\right] + \exp\left[p_{bo,5}\left(\frac{r_{ij}}{r_0^{\pi\pi}}\right)^{p_{bo,6}}\right] \quad (2\text{-}8)$$

$$E_{bond} = -D_e^{\sigma} BO_{ij}^{\sigma} exp\left[p_{be,1}\left(1-\left(BO_{ij}^{\sigma}\right)^2\right)\right] - D_e^{\pi} BO_{ij}^{\pi} - D_e^{\pi\pi} BO_{ij}^{\pi\pi} \quad (2\text{-}9)$$

Lone pairs on heteroatoms such as oxygen atoms can affect dramatically the response of these atoms to over- and under-coordination. Furthermore, the presence of these lone electron pairs influences the valence angles around atoms. In addition, by delocalizing, they can contribute to the stability of conjugated systems. Eq.2-10 describes the deviation of the number of lone pairs around an atom from the number of lone pairs at normal coordination (2 for oxygen, 0 for silicon and hydrogen).

$$E_{lp} = \frac{p_{lp}\Delta_{lp,1}}{1+\exp\left(-75\Delta_{lp,1}\right)} \quad (2\text{-}10)$$

For an over-coordinated atom ($\Delta > 0$), 2-11 imposes an energy penalty on the system. The form of Eq.2-11 ensures that E_{over} will quickly vanish to zero for under-coordinated systems ($\Delta < 0$).

$$E_{over} = p_{lp}\Delta_l \frac{1}{1+\exp\left(\Delta_l\lambda_6\right)} \quad (2\text{-}11)$$

For an under-coordinated atom ($\Delta < 0$), the energy contribution is taken account for the resonance of the π-electron between attached under-coordinated atomic centers. This is described in Eq.2-12:

$$E_{under} = -p_{under}\frac{1-\exp(\lambda_7\Delta_i)}{1+\exp(-\lambda_8\Delta_j)} f_6(\mathrm{BO}_{ij,\pi}\Delta_j) \quad (2\text{-}12)$$

Just as for bond terms, it is important that the energy contribution from valence angle terms goes to zero as the bond orders in the valence angle goes to zero. Eq.2-13 is used to calculate the valence angle energy contribution.

$$E_{val} = f_7(\mathrm{BO}_{ij}) f_7(\mathrm{BO}_{jk}) f_8(\Delta_j) \left\{ k_a - k_a exp\left[-k_b \left(\theta_0 - \theta_{jkl} \right)^2 \right] \right\} \quad (2\text{-}13)$$

To reproduce the stability of systems with two double bonds sharing an atom in a destabilizes, like allene, an additional energy penalty, as described in Eq.2-14, is imposed.

$$E_{pen} = \lambda_{19} f_9(\Delta_j) exp\left[-\lambda_{20} \left(\mathrm{BO}_{ij} - 2 \right)^2 \right] exp\left[-\lambda_{20} \left(\mathrm{BO}_{jk} - 2 \right)^2 \right] \quad (2\text{-}14)$$

Just as with angle terms we need to ensure that dependence of the energy of torsion angle ω_{ijkl} accounts properly for BO smaller than 0 and for BO greater than 1. This is done by Eq.2-15.

$$E_{tors} = f_{10}\left(\mathrm{BO}_{ij}, \mathrm{BO}_{jk}, \mathrm{BO}_{kl} \right) \sin\theta_{ijk} \sin\theta_{jkl} \langle \frac{1}{2} V_2 exp\{ p_l [\mathrm{BO}_{jk} - 3 + f_{11}(\Delta_j, \Delta_j)] \} \rangle \quad (2\text{-}15)$$

Eq.2-16 describes the contribution of conjugation effects to the molecular energy.

$$E_{conj} = f_{12}\left(\mathrm{BO}_{ij}, \mathrm{BO}_{jk}, \mathrm{BO}_{kl} \right) \lambda_{26} \left[1 + \left(\cos^2 \omega_{ijkl} - 1 \right) \sin\theta_{ijk} \sin\theta_{jkl} \right] \quad (2\text{-}16)$$

In addition to valence interactions which depend on overlap, there are repulsive interactions at short interatomic distances due to Pauli principle ortho-gonalization

and attraction energies at long distances due to dispersion. These interactions, comprised of van der Waals and Coulomb forces, are included for all atom pairs, thus avoiding awkward alterations in the energy description during bond dissociation. In this respect, ReaxFF is similar in spirit to the central valence force fields that were used earlier in vibrational spectroscopy. To account for the van der Waals interactions we use a distance-corrected Morse-potential (Eq.2-17). By including a shielded interaction, excessively high repulsions between bonded atoms (1-2 interactions) and atoms sharing a valence angle (1-3 interactions) are avoided.

$$E_{vdwaals} = D_{ij}\left\{exp\left[1-\frac{f_{13}(r_{ij})}{r_{vdw}}\right]-2exp\left[\frac{1}{2}\alpha_{ij}\left(1-\frac{f_{13}(r_{ij})}{r_{vdw}}\right)\right]\right\} \quad (2\text{-}17)$$

As with the van der Waals interactions, Coulomb interactions are taken into account between all atom pairs. To adjust for orbital overlap between atoms at close distances a shielded Coulomb potential is used.

$$E_{coulomb} = \mathrm{C}\frac{q_i q_j}{[r_{ij}^3+\left(\frac{1}{\gamma_{ij}}\right)^3]^{1/3}} \quad (2\text{-}18)$$

Atomic charges are calculated using the Electron Equilibration Method (EEM) approach (Janssens et al., 1995).

2.4.4 Energy Minimization

Energy minimization is the process of looking for an arrangement in the space of a collection of atoms where, according to some computational model of chemical

bonding, the net inter-atomic force on each atom is acceptably close to zero, and the position on the potential energy surface is a stationary point. Typical minimize methods are introduced: the energy minimization algorithms, Steepest Descent and Conjugate Gradients method (Knyazev and Lashuk, 2007), all of which are derivatives of the potential energy. For the force of each atom (F), it is the negative derivative of the potential energy (U) over the inter-atomic distance (r) shows as follows:

$$\mathrm{F} = -\frac{\partial \mathrm{U}}{\partial \mathrm{r}} \tag{2-19}$$

The potential energy of a hole system can be expressed by taylor series expansion as:

$$\mathrm{U}(\mathrm{r}+\delta\mathrm{r}) = U(r) + \frac{\partial U}{\partial r}\delta r + \frac{1}{2!}\frac{\partial^2 U}{\partial r^2}(\delta r)^2 + \cdots \tag{2-20}$$

And the first two items or first three items are generally chosen to express potential energy, and the first derivative is called the gradient vector (g), and the second derivative is called Hessian matrix (H). For steepest descent method, the first two items in Eq.2-14 is chosen to be approached to the potential energy. In this algorithm, the way to determine the steepest descent direction is to employ a line search or an arbitrary step size for each iteration step. The net force of each atom is calculated from the expression of potential energy, and the position of each atom is calculated according to:

$$r_i^j = r_i^{j-i} + \alpha_m \cdot F_i \tag{2-21}$$

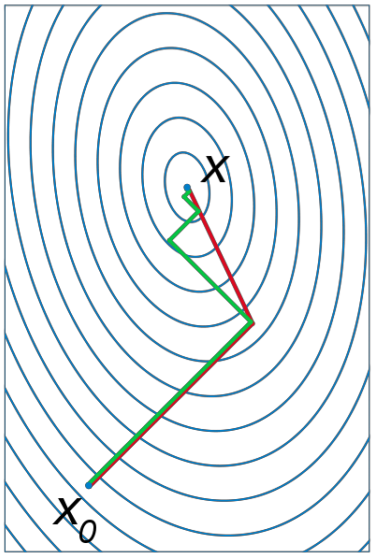

Figure 2.24 The schematic diagram of the convergence of gradient descent (in green line) and conjugate gradient (in red line) for energy minimization of a quadratic function for a linear system.

The procedure is repeated for every time step (j) until the force (F) on each atom reaches zero, where i is the atom number, j is the time step, α_m is the multiplication factor, F_i is the net force on an atom at that time step. In this method, directions of the consecutive steps in the iterative process are vertical to each other (as shown in Figure 2.24).

The advantage of the steepest descent method is that it is very efficient when the original structure is extremely different from the structure after energy minimization, such as a large gradient of potential energy shows up. On the other hand, the disadvantage is evident that when the structure is close to approaching the minimum energy, it is inefficient due to the smaller gradient of potential energy. These algorithms are also numerically stable that the potential energy of the whole system

keeps decreasing for an appropriate assumption of α_m. Therefore, it can be used with the conjugate gradient method, which works more efficient.

The conjugate gradient method works more effective when the gradient of the potential energy is smaller compared to the steepest descent method. In this method, the successive search directions are made conjugate, i.e., the step directions are made orthogonal to its preceding search vector. The residuals calculated in the method of conjugate gradient methods (as shown in Figure 2.24) are orthogonal to preceding directional search vectors. Energy minimization using this method has lesser steps compared to the steepest gradient methods.

2.4.5 Ensembles

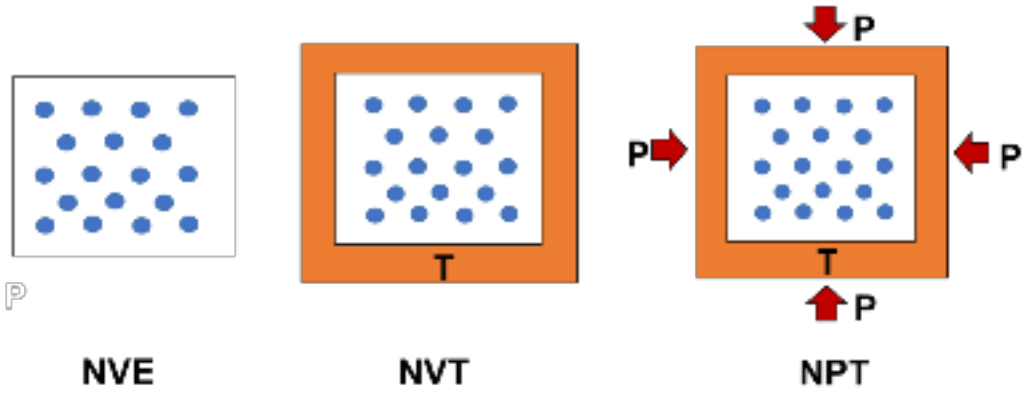

Figure 2.25 Schematic of NVE, NVT and NPT ensembles

An ensemble is an idealisation consisting of a large number of virtual copies of a system that represents a possible state the real system might be in. In other words, a

statistical ensemble is a probablility distribution for the state of the system. It is a valuable method of achieving system averages from numerous states which may happen. Generally, there are three types of ensembles applied in MD simulations, which are NVE, NVT and NPT, where N is the number of atoms (particles) in the whole system, E is the total system energy, V is the system volume, T is the temperature of the system and P is the pressure. Figure 2.25 shows the schematic of VE, NVT and NPT ensembles as follows:

2.4.5.1 NVT Ensemble

Constant temperature can be achieved in molecular dynamics by implementing a Nose-Hoover Thermostat (Hoover, 1985, Nosé, 1984). Implementing this will produce the same conservation laws as the canonical ensemble. In this ensemble the number of atoms in the system is conserved as is the volume, temperature, and total momentum of the system. The thermostat is implemented by introducing an additional degree of freedom, s, into the system. The interaction between the physical system and the virtual degree of freedom, s, can be reduced to a rescaling of the real time variable t' to a virtual time variable, t:

$$dt = s(t')dt' \tag{2-22}$$

The virtual variables t, r_i, and p_i are then related to real variables t, r_i, and p_i as follows:

$$\mathrm{r}_i' = \mathrm{r}_i \tag{2-23}$$

$$\mathrm{P}_i' = \frac{P_i}{s} \tag{2-24}$$

$$\mathrm{t}' = \int_0^t \frac{dt\prime}{s} \tag{2-25}$$

The following Lagrangian is then proposed for the system:

$$\mathrm{L} = \frac{1}{2}\sum_i^N m_i s^2 \dot{r}_i' - \Phi(r) + \frac{Q}{2}\dot{s}^2 + gkT\ln s \tag{2-26}$$

Here Q is a parameter with units of energy×(time)^2 which acts like an effective mass for the degree of freedom s. The number of degrees of freedom in the system is g, T is an externally set temperature, and k is Boltzmann's constant. We can now derive the equations of motion for this Lagrangian using the Lagrangian equation:

$$\frac{d}{dx}\left(\frac{\partial L}{\partial \dot{A}}\right) = \frac{\partial L}{\partial A\prime} \tag{2-27}$$

We then obtain the equations of motion:

$$\ddot{\mathrm{r}} = -\frac{1}{m_i s^2}\frac{\partial \Phi}{\partial r_i} - \frac{2\dot{s}}{s}\dot{r}_i \tag{2-28}$$

$$\mathrm{Q}\ddot{s} = \sum_i^N m_i s \dot{r}_i^2 - \frac{gkT}{s} \tag{2-29}$$

This system can be shown to produce the same conservation laws as the canonical ensemble (Hoover, 1985, Nosé, 1984). Momentum is also conserved using this thermostat. The Hamiltonian for this system is given by:

$$\mathcal{H} = \sum_i^N \frac{P_i^2}{2m_i s^2} + \Phi(r) + \frac{P_s^2}{2Q} + gkT \ln s \qquad (2\text{-}30)$$

T he variable s was interpreted by Nosé as a time-scaling variable. Hoover switched back to real time by replacing p_i in equation 3.35 with sp_i (Hoover, 1985). By introducing the variable $\xi = p_s/Q$, the variable s is eliminated from the equations of motion. Hoovers equations of motion were:

$$\dot{P}_i = \dot{F}_i - \xi P_i \qquad (2\text{-}31)$$

$$\dot{\xi} = \frac{2}{Q}\left(\frac{P_i^2}{m_i} - \frac{gkT}{2}\right) \qquad (2\text{-}32)$$

The alteration to the dynamics of the real system depends on the thermostat variable, ξ, and the dynamics of ξ depends on the difference between the current system kinetic energy and the desired system kinetic energy. Rewriting Eq.2-31 in terms of velocity rather than momentum, we get:

$$\dot{v}_i = \frac{F_i}{m_i} - \xi v_i \qquad (2\text{-}33)$$

At each time step in a simulation, the following calculation must be performed by numerical integration:

$$v_i(t + \Delta t) = v_i(t) + \int_t^{t+\Delta t} \frac{F_i}{m_i} dt - \int_t^{t+\Delta t} -\xi v_i dt \qquad (2\text{-}34)$$

This is easy to implement in existing molecular dynamics codes as the first integral on the right hand side of Eq.2-34 is the integral which is calculated in a molecular dynamics simulation without a thermostat. To imple ment the Nosé-Hoover

Thermostat, the volocities can simply be adjusted at each time step by adding a term, Δv_i^{Nose}, to the velocity of each particle in the system. This term, Δv_i^{Nose}, is simply the second integral term in Eq.2-34:

$$\Delta v_i^{Nose} = -\int_t^{t+\Delta t} \xi v_i dt \tag{2-35}$$

The NVT ensemble was used for some calculations reported in this thesis. Whenever simulations are carried out at constant volume with a Nosé-Hoover Thermostat implemented to preserve temperature, the simulation is carried out in the NVT ensemble.

2.4.5.2 NPE and NPT Ensembles

The Parrinello-Rahman method (Parrinello and Rahman, 1981) can be used to create an NPE ensemble, in which the total number of atoms in the system, the pressure, the total energy, and the total momentum of the system are conserved. When used in combination with a Nosé-Hoover Thermostat, an NPT ensemble is produced, in which the number of atoms in the system is conserved as well as the pressure, temperature, and total momentum of the system.

In this method we write the positions of all atoms in terms of fractional coordinates α_i, β_i, and γ_i. The system cell containing the atoms is a parallelepiped defined by three vectors a, b, and c. The real space coordinates of the atoms are then given by:

$$r_i = \alpha_i a + \beta_i b + \gamma_i c \tag{2-36}$$

If a boxmatrix is defined, h, given by h = [a, b, c], and a fractional coordinate vector $s_i = (\alpha_i, \beta_i, \gamma_i)$, the above relation simplifies to:

$$r_i = hs_i \tag{2-37}$$

The 9 variables which make up the matrix h are now treated as additional degrees of freedom. The following Lagrangian is now proposed:

$$\mathrm{L} = \frac{1}{2}\sum_i^N m_i \dot{s_i}' h' h \dot{s_i} - \sum_i^N \Phi_i\left(\{r_j\}\right) + \frac{1}{2} WTr\dot{h}'\dot{h} - PV \tag{2-38}$$

where P is the hydrostatic pressure and V is the volume of the system. Here Φ_i is the potential energy of atom i and it is a funtion of the set of the set of all atomic positions which is denoted (Bauchy et al.). h' and s' denote the transposes of h and s respectively. From this we can use the Lagrangian equation to get the following equations of motion:

$$\ddot{s_i} = -\sum_{j\neq \mathrm{i}} m_i^{-1}\left(\frac{1}{r_{ij}}\frac{d\Phi(\{r_j\})}{dr_{ij}}\right)\left(s_i - s_j\right) - G^{-1}\dot{G}\dot{s_i} \tag{2-39}$$

$$\mathrm{W}\ddot{h} = (\Pi - \mathrm{P})V\mathrm{h}'^{-1} \tag{2-40}$$

Here Π is a matrix whose components, $\Pi_{\alpha\beta}$, are given by:

$$\mathrm{V}\Pi_{\alpha\beta} = \sum_i m_i v_{i,\alpha} v_{i,\beta} - \frac{\partial \Phi}{\partial h_{\alpha\beta}} h'_{\delta\beta} \tag{2-41}$$

where G = h'h. Here $v_{i,\alpha}$ and $v_{i,\beta}$ are components of the velocity of particle i and thus:

$$v_{i,\alpha} = h_{\alpha,\delta} s_{i,\delta}^{\cdot} \tag{2-42}$$

where $s_{i,\delta}^{\cdot}$ is the δ component of the $\dot{s}$ vector. Note that in the last two equations we have assumed the convention of implicit summation over repeated indices. The Hamiltonian for this system is:

$$\mathcal{H} = \frac{1}{2}\sum_i^N m_i \dot{s_i'} h' h \dot{s_i} + \sum_{i=1}^N \sum_{j>1}^N \Phi(r_{ij}) + \frac{1}{2} W T r \dot{h'} \dot{h} + PV \tag{2-43}$$

At temperature, T, the term containing W contributes just $9/2k_BT$ to the total Hamiltonian while the atomic degrees of freedom contribute $3N/2k_BT$. The W term is therefore negligible and the Hamiltonian can be approximated as the enthalpy of the system:

$$\mathcal{H} \approx \mathrm{H} = \mathrm{E} + \mathrm{PV} \tag{2-44}$$

For the work presented in this thesis, the NPT ensemble was occasionally used to allow systems to relax to their equilibrium volume and shape at a given temperature. Whenever a simulation is carried out at constant pressure and a Nosé-Hoover Thermostat is used to preserve temperature, then the simulation is carried out in the NPT ensemble.

2.4.6 MD algorithm

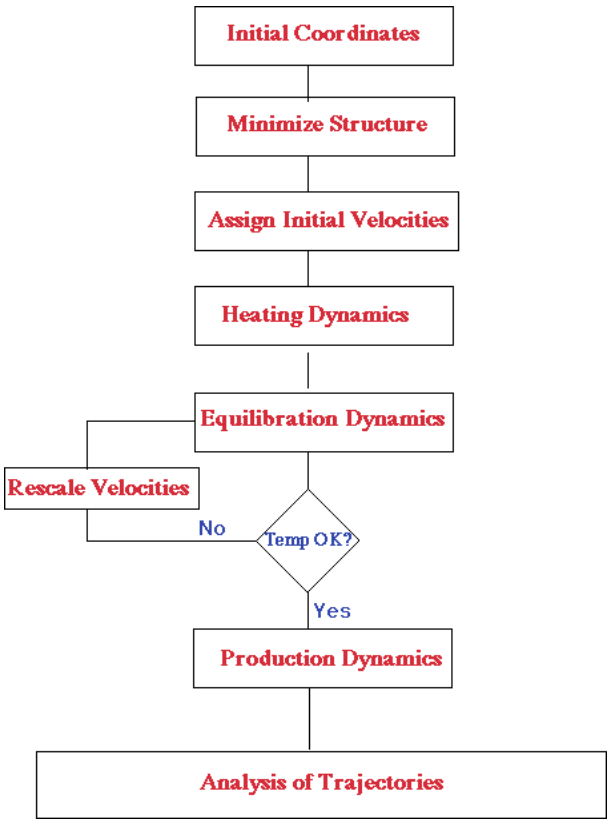

Figure 2.26 Flow chart of the MD algorithm.

The basic MD algorithm is demonstrated in Figure 2.26. To begin a molecular dynamics simulation, an initial configuration of the system, a starting point, or t=0 should be selected. The choice of the initial configuration must be done carefully as this can influence the quality of the simulation. It is often good to choose a configuration close to the state that you wish to simulate. As to the C-S-H analogue, the crystal structure of tobermorite 11 Å, obtained from the NMR and XRD experiment, is set as the initial structure.

Before starting a molecular dynamics simulation, it is necessary to operate energy minimization on the structure to remove any strong van der Waals or Coulombic interactions. Otherwise, it leads to local structural distortion and results in an unstable simulation. Subsequently, initial velocities at a low temperature are assigned to each atom of the system and Newton's equations of motion are integrated to propagate the system in time.

2.4.6.1 Verlet Algorithm

Application of Verlet algorithm in molecular dynamics was popularized in the 1960s (Verlet, 1967). This method uses the positions 'r' and accelerations of the atoms at time 't' along with the positions at time 't-Δt' in order to calculate the new position at time 't+Δt'. Using Taylor series expansion, position at time 't+Δt' and 't-Δt' can be written as,

$$\mathrm{r(t+\ \Delta t)} = r(t) + v(t)\Delta t + \frac{1}{2}a(t)\Delta t^2 \quad (2\text{-}45)$$

$$\mathrm{r(t-\ \Delta t)} = r(t) - v(t)\Delta t + \frac{1}{2}a(t)\Delta t^2 \quad (2\text{-}46)$$

where v is the velocity and a is the acceleration. Taking a sum of the two equations, the updated position in terms of previous position and accelerations can be written as,

$$\mathrm{r(t+\Delta t)} = r2(t) - r(t-\Delta t) + \frac{1}{2}a(t)\Delta t^2 \quad (2\text{-}47)$$

It is evident from the equation that explicit computations of velocities are not required. While it is simple to implement and computation resource friendly, this method is not very accurate.

2.4.6.2 Velocity Verlet Algorithm

One of the more commonly used numerical integration methods used in MD simulations is the velocity Verlet algorithm (Swope et al., 1982). As the name indicates, it is a variation of the Verlet algorithm discussed earlier. In this method, the velocities 'v' and positons 'r' at time 't+Δt' are given by,

$$\mathrm{v}(\mathrm{t}+\ \Delta\mathrm{t}) = \ v(t) + \frac{1}{2}[a(t) + a(t+\Delta\mathrm{t})]\Delta t \tag{2-48}$$

$$\mathrm{r}(\mathrm{t}+\ \Delta\mathrm{t}) = \ r(t) + v(t)\Delta\mathrm{t} + \frac{1}{2}a(t)\Delta\mathrm{t}^2 \tag{2-49}$$

This algorithm produces updated positions and velocities of the atoms without compromising on the precision, which occurs in the original Verlet method. The velocity Verlet algorithm has been implemented in LAMMPS (Plimpton, 1995) and is used in this dissertation. More discussion on LAMMPS will be presented in a different section.

2.4.6.3 Pressure and Temperature calculation

In case of atoms, all particles are assumed to have no other degrees of freedom than their translational movements in every dimension, so that the equi-partition theorem

can be used to calculate the temperature T in a d-dimensional system (usually d = 3) of n particles.

$$\frac{1}{n}\sum_{i=0}^{n-1}\frac{m_i}{2}v_i^2 = \frac{d}{2}k_B T \tag{2-50}$$

$$\Rightarrow \ \mathrm{T} = \frac{1}{dk_B n}\sum_{i=0}^{n-1} m_i v_i^2 \tag{2-51}$$

Knowing the positions $\underset{\mathrm{r}}{\rightarrow}$ and forces $\underset{\mathrm{F}}{\rightarrow}$ of all n (identical[1]) particles, the virial Φ is defined as:

$$\Phi = \sum_{i=0}^{n-1}\sum_{j=i+1}^{n-1}\left\langle \underset{r_i}{\rightarrow} - \underset{r_j}{\rightarrow}, \underset{F}{\rightarrow}\left(\underset{r_i}{\rightarrow} - \underset{r_j}{\rightarrow}\right)\right\rangle \tag{2-52}$$

Using this virial Φ, the current pressure p in a system of dimensionality d with volume V can be calculated by (Plimpton, 1995):

$$\mathrm{p} = \frac{1}{V}\left(nk_B T + \frac{\Phi}{d}\right) \tag{2-53}$$

2.5 MD Modelling of C-S-H and nanocomposites

To establish the model of GO reinforced cement in molecular dynamics method, the most basic knowledge of the model needs to be fully understood with details, which can be classified to three parts: cement, graphene oxide and the interface of cement and GO.

2.5.1 Pellenq's MD model on C-S-H

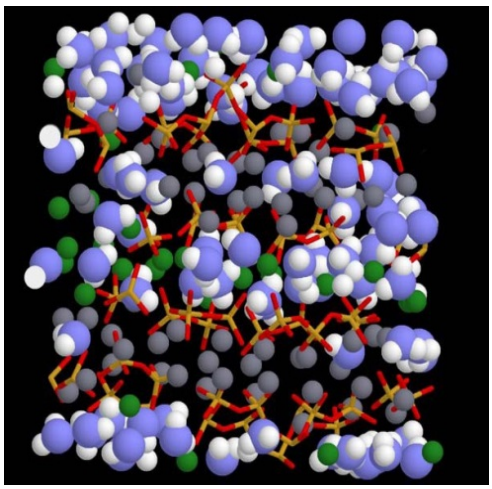

Figure 2.27 Model of cement provided by Pellenq et al. (2009).

As been mentioned before, C-S-H gel is the primary portion of cement hydration products, and it undertakes most of cohesion and strength in cementitious structures. Pellenq and Van Damme (2004) first provided initial research of the factors for controlling the setting and hardening of cement paste on atoms and molecular scale. As C-S-H gel is not perfect crystalline, it is consisted of various elements and pores. Has been studied for years and years, over 30 crystalline model of C-S-H structures were identified (Manzano et al., 2007, Richardson and Groves, 1992, Richardson, 2004, Taylor, 1986), and a little researches reveal an amorphous model (Van Damme and Gmira, 2006). 14 Å tobermorite and jennite are most common crystalline phases presented in the knowledge of C-S-H gel structure, whereas the model of amorphous structure for C-S-H gel is tremendously challenging to establish with little obtainable knowledge in the literature. Generally, C-S-H gel is defined by the calcium-silicon

(Ca/Si) ratio ranging from 0.6 to 2.3 (Selvam et al., 2009). Tobermorite owns a molecular structure with a Ca/Si ratio of 0.83 and density of 2.18g/cm^3, and Jennite has a Ca/Si ratio of 1.5 and a density of 2.27 g/cm^3. Taylor (1997) provided models of two important C-S-H minerals: 14 Å tobermorite with chemical formula $Ca_5Si_6O_{16}(OH)_2 \cdot 7H_2O$ and Jennite with formula $Ca_9Si_6O_{18}(OH)_6 \cdot 8H_2O$. Based on that, Richardson (1999) suggested two models to classify C-S-H structure that one is tobermorite/jennite (T/J) model and the other one is tobermorite/calcium hydroxyl (T/CH) model. The T/J model is jennite domains follow assembled tobermorite regions, and the T/CH model is consisted of layers containing tobermorite sandwiched between calcium hydroxyl, which provides a higher Ca/Si ratio than tobermorite.

Allen et al. (2007) measured the composition and solid density of C-S-H gel is 2.604 g/cm^3 by combining small-angle neutron and X-ray scattering data and exploiting the hydrogen/deuterium neutron isotope effect both in water and methanol, and achieve the formula $(CaO)_{1.7}(SiO_2)(H_2O)_{1.80}$. According to the previous reasonable results, Pellenq et al. (2009) suggests the first model of C-S-H molecular structure by molecular dynamics simulations. His model is based on a mean value of 1.7 for Ca/Si ratio from Richardson (1999) and repeat of the 11 Å tobermorite crystalline structure. To match the Ca/Si value in the simulation of C-S-H (Figure 2.27), short silica chains are connected between calcium and silicon dioxide based on the ^{29}Si nuclear magnetic resonance (NMR) (Cong and Kirkpatrick, 1996, Ayuela et al., 2007). Moreover, an

appropriate amount of H_2O molecular is added to provide a realistic density of 2.6 g/cm^3. In the meantime, a force field called "CSHFF", which is typically adopted to C-S-H model, supplied from this study. To verify CSHFF in C-S-H model, Shahsavari et al. (2011) compared different force field with DFT results and various mechanical properties are achieved via using different force fields. Based on the 'milestone' model, various possible test on nanoscale of cement can be realised via simulation (Hou et al., 2014b, Hou et al., 2014c).

2.5.2 Hou's MD model on C-S-H

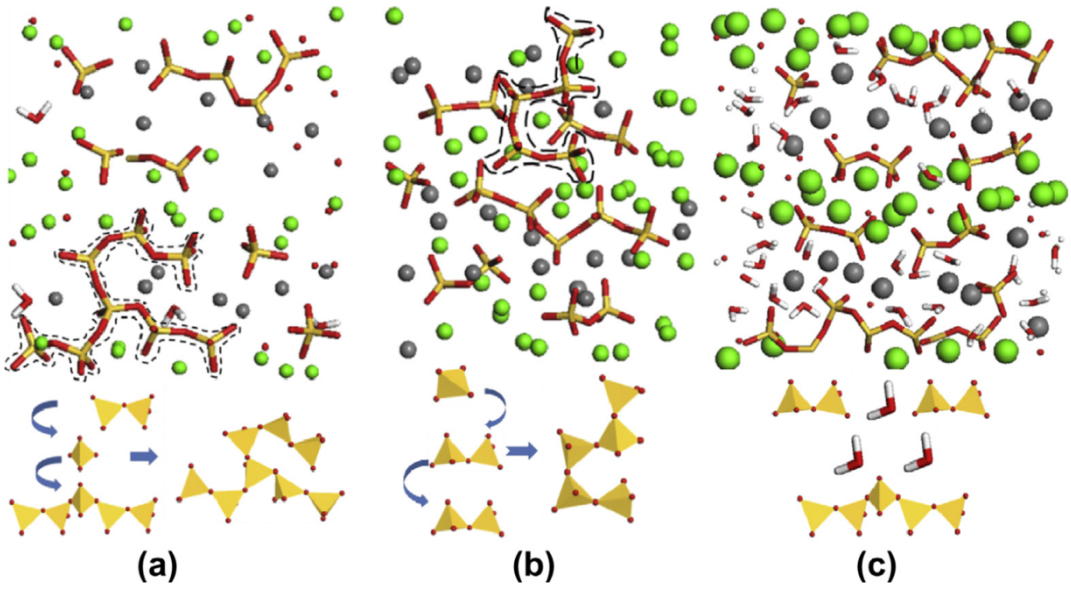

Figure 2.28 Morphology change of silicate chain: (a) polymerization in the dry sample (b) polymerization in the sample with water/Ca =0.3 (c) morphology of the silicate chain in the saturated state.

Based on the Pellenq's model, Hou has simulated the properties of C-S-H and analysed the chemical bonds in the C-S-H structure using multi-force fields

including CSHFF and ReaxFF (Hou et al., 2014d, Hou et al., 2014c, Hou et al., 2015, Hou et al., 2014a).

The morphology of silicate chains with different water contents in C-S-H models is shown in Figure 2.28. In the dry state, bridging silicate tetrahedrons linked with the surrounding monomers and connected with neighbouring tetrahedrons. When the water/Ca ratio reaches 0.3, two dimers and one monomer can be linked together to form a longer silicate chain cross the interlayer space. In the saturated samples, Q_1 is the dominant phase and dimer structures develop in an orderly fashion, and water molecules block the silica chains to link together.

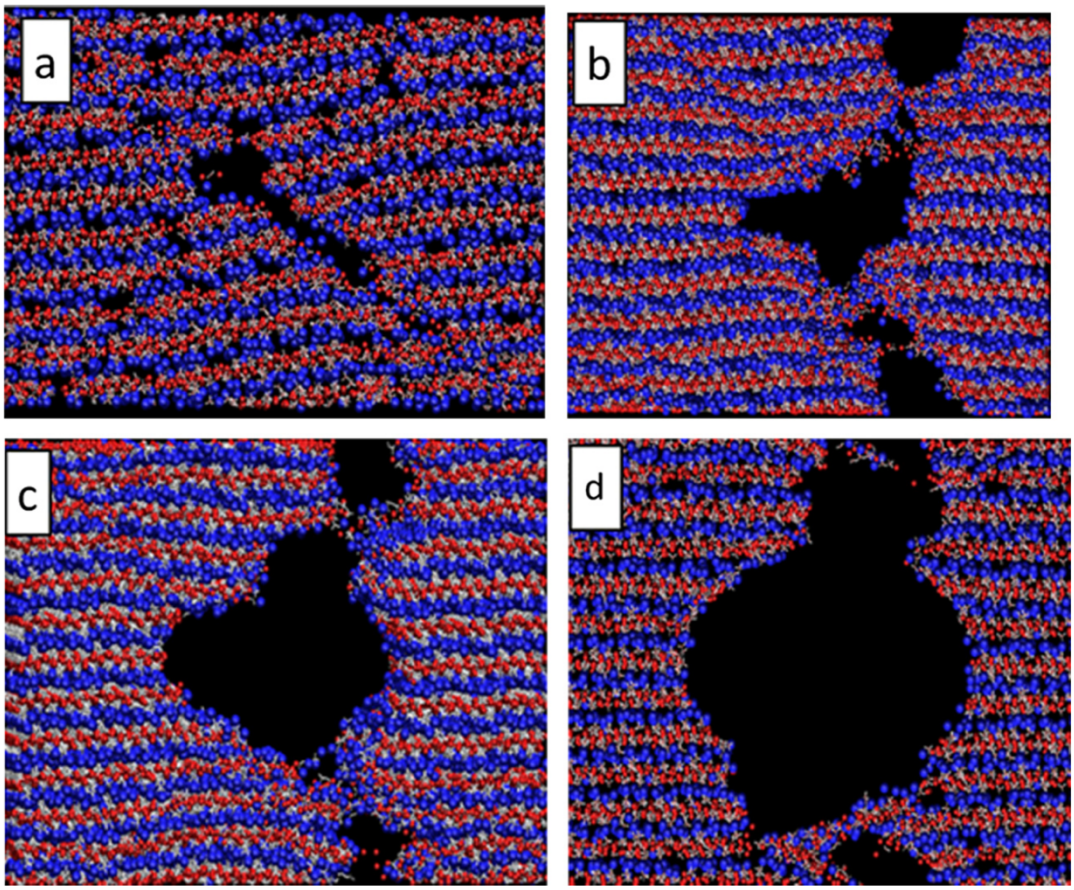

Figure 2.29 Snapshots of C-S-H gel with central void of diameter (a) 5 (b) 15 (c) 30 (d) 50 Å tensioned along x direction at strain 0.24 Å/ Å

Morphologies of damaged C-S-H gels with different original cracks in the central strain 0.24 Å/Å is shown in Figure 2.29 (Hou et al., 2014c). The size effect of voids on the fracture trend and stress-strain relationship has been simulated in this study. The presence of the original crack ranging from 20 Å to 50 Å deteriorates the stiffness of C-S-H structure, and the voids are detrimental to the mechanical properties of C-S-H on nanoscale obviously. The strain concentration happens at the boundary of the local defective region which is around the original voids.

2.5.3 GO model

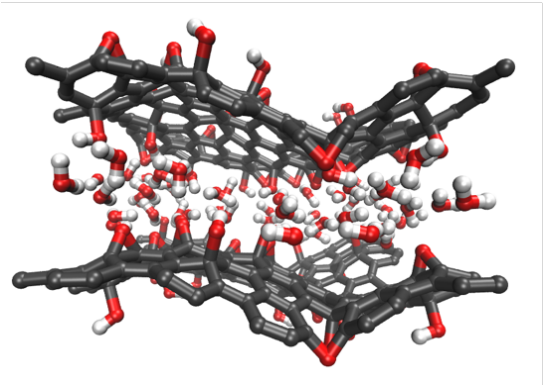

Figure 2.30 Model of Graphene Oxide and water interface provided by Dyer et al. (2015).

Graphene oxide is a derivative material based on graphene, the model of which is quite uniform and 'simple' compared to C-S-H model. Graphene has been widely concerned after Geim A. and Novoselov K. were awarded Nobel Prize in 2010, meanwhile, graphene oxide has been studied widely in recent years. By given acid

functional groups from graphene, it is deserved to achieve significant results from molecular dynamics method.

Shao et al. (2012) built an MD simulation of GO revised by Lerf-Klinowski model to test and verify the mechanisms results of GO oxidation and exfoliation from the experimental method. To study the mechanisms of wrinkles in graphene and graphene oxide sheets and their effects on the Young's modulus, Shen et al. (2014) chose COMPASS force field to do the simulation in different positions of two sheets, which are edge-to-edge interaction and face-to-face interaction, with the results and comparison of tension and Young's modulus. Zhang and Jiang (2014) studied the structural and mechanical properties of graphene/GO paper and polymer composites with COMPASS force field. This research presented the interface between GO and polymers with the influence of oxygen-containing groups and H-bond networks, and the structural and mechanical results achieved from this kind of multi-material composites provide the opportunity to study the interface of more complex GO-based composite. While Dyer et al. (2015) constructed a continuum model for GO completely based upon the Lerf-Klinowski model to study the interaction stress transfer between GO sheets themselves and GO sheets sandwiching water molecular using ReaxFF force field (Figure 2.30). With details of the mathematical method of presenting continuum approach and interaction energy, this model provides strong support in investigating hydration and oxidation within GO and water system.

2.5.4 Interface between GO and C-S-H

As GO reinforced cement is exceptionally new material, there is almost no information about the model of interaction between GO and C-S-H gel. Whereas based on the chemical composition and nanostructure of GO cement composition mentioned before, it is reasonable to realise the interface as accurate as possible with the details of the covalent bond and chemical energy between calcium and functional groups in GO. Fortunately, a latest DFT study on the interaction of calcium ions with carboxylic acids has been published (Mehandzhiyski et al., 2015), which provides the potential of the carboxyl and calcium ions interfaces, making the MD simulation of GO and C-S-H possible.

Chapter 3. Interfacial Stress Transfer in Graphene-Oxide Cementitious Composites

3.1 Introduction

Despite the promising future of incorporating GO in forming cementitious nanocomposites for optimal engineering properties, the current research of GO cement is still at a very early stage. To investigate the massive increase in the mechanical properties of GO cement, it is necessary to study the interfacial stress transferring mechanisms between the cement and the GO. The stress transferring mechanisms and effectiveness at the interfaces controls the global mechanical performance of the GO cement. MD provides unique insight into the mechanical performance of cementitious materials and nanocomposites at the nanoscale. MD can be used to calculate the deformation, the stress, and various molecular properties of cement systems (Shahsavari et al., 2011, Wu et al., 2011, Hou et al., 2014c). A molecular approach to determining the mechanical properties of cementitious materials is extremely helpful when physical nanoscale experiments are not widely available. In GO cement, the GO is mixed and reacted with the main binding phase of cement — a calcium-silicate-hydrate (C-S-H) gel. Alkhateb et al. (2013) has investigated the interfacial stress transfer for GO cement. In their study, a cell containing C-S-H with a layer of GO in the middle was constructed, and the COMPASS force field was applied. A pull-out test was conducted, and the interfacial strengths were calculated. However, the structure of C-S-H was not clear, and the full stress-strain curve, which represents the complete stress transferring behaviour,

was not shown. Li and co-workers (Li et al., 2011) simulated the pull-out test of carbon nanotube polymer with MD and produced the full shear stress and displacement relation at the interface between the carbon nanotube and the polymer. Ding et al. (2012) investigated the effects of GO sheets in poly(vinyl alcohol)/GO composites by using MD and found that the degree of oxidation of the GO sheet influenced the strength of interfacial binding characteristics between GO and the polymer. Liu et al. (2015) examined the interfacial mechanical properties of wrinkled GO/polyethylene and GO/PMMA composites by pull-out tests with MD; it has been found that the pull-out velocity of the wrinkled GO sheet has a great impact on the interfacial stress transfer capacity for both types of composites and the wrinkled shape of GO can also enhance the interfacial mechanical properties. To the best knowledge of the authors, however, there is very little research in modelling the interfacial mechanical properties of GO/cement composite and none in deriving the complete interfacial shear stress/displacement relation with MD.

This chapter attempts to model the interfacial stress transferring mechanism in GO reinforced cement using MD and derive the full shearing stress displacement curve by the pull-out test. The C-S-H structure used is based on 11Å tobermorite, and the Lerf-Klinowski model for the GO structure is employed with the random distribution of the functional groups. ReaxFF is used to represent the interatomic interactions in the MD simulation. The GO sheet is pulled out of the C-S-H, and the full stress

displacement curve is obtained based on which the complete stress transferring mechanism is discussed. The sensitivity of the pulling rate on the results is investigated and for each pulling rate, three tests/simulations are carried out to ensure repeatability and reliability. The interfacial shear stress is then calculated as a function of pull-out displacement. A yielding-like stage, between the linear stress increase and the stress softening, is identified. The elastic-plastic-fracture phenomenon has been first observed at the nanoscale for GO cement composite and will have a significant impact on engineering mechanical properties. The energies of the interface between GO and C-S-H, and the carbon atoms from the GO sheet are also calculated and discussed. The results from this model are highly complementary to finite element multi-scale modelling on GO cement composites. In order to accurately simulate the mechanical behaviour of the GO cement, especially at the mesoscale and microscale, the interfacial properties between GO and cement are necessary. However, such properties are extremely difficult to determine from experimental tests. This has motivated the work in this chapter.

The remainder of this chapter is structured as follows. In Section 3.2, the formulation of the model which covers the molecular structure of the composite, the interatomic force field, and the loading protocol for determining the interfacial mechanical properties are presented. In the next section, the results of the load-displacement relationship for different loading rates, as well as the energies for both the interface

and the carbon atoms are discussed. It is then followed by analysis of the interfacial mechanism and calculation of the shear stress development over the pull-out displacement.

3.2 Methodology

The structure of C-S-H analysed in this chapter is constructed based on the 11 Å tobermorite structure reported in (Merlino et al., 2001). The structure of C-S-H is considered very similar to that of 11 Å tobermorite (Richardson, 2004) with two main differences: the calcium/silicon ratio and the silicate chain length. Researchers have been trying to determine the molecular structure for C-S-H materials based on 11 Å or 14 Å Tobermorite, but there are still few widely acknowledged models. Pellenq et al. (2009) have derived perhaps the first realistic molecular model for C-S-H with MD, which represented the first-step forward towards modelling the mechanical properties of C-S-H. However, the several shortcomings of the model have been pointed out, such as a few aspects of the structure do not match with the general observations on crystalline calcium silicate hydrates (e.g., the coordination of Ca-O) (Richardson, 2014). In this chapter, the well-understood 11 Å tobermorite structure is used as the structure of C-S-H, which is believed reasonable, since the interface between the C-S-H and GO is the focus of the research.

The GO structure in this chapter is based on the Lerf-Klinowski GO model (Lerf et al., 1998) with the distortions neglected and the carbon plane structurally unaffected, as shown in Figure 2.11. In this model, the functional groups, including epoxy and hydroxyl, are distributed randomly (Mkhoyan et al., 2009) to avoid the energy reduction of GO sheet due to the gathering of the functional groups (Yan and Chou, 2010). Generally, the range of oxidation varies from a C/O ratio of 4:1–2:1 (Lahaye et al., 2009). In this model, the ratio of C/O is set to 3.2:1. The distribution of oxygen atoms is derived by Dyer et al. (2015), which was based on the density functional theory (DFT) analysis performed by Yan and Chou (2010). An epoxy functional group is a single oxygen atom bonded to two neighbouring carbon atoms in the carbon plane. The C-O bond length at relaxation is found 1.44 Å. The CAC bond is stretched to 1.51 Å and the two carbon atoms move out of the plane by 0.34 Å. Therefore, the oxygen atom in an epoxy group is deduced at a perpendicular distance of from the carbon basal plane. The hydroxyl functional group is constructed as the OH group bonds to certain carbon atoms. The O-H bond length is found to be 0.98 Å, and the angle of C-O-H bond is 107.9°. The attached carbon atom is distorted out of the plane by 0.37 Å. The hydrogen and oxygen atoms are placed at the same plane perpendicular to the basal plane for simplicity. Therefore, the oxygen atoms in hydroxyl groups stay at the perpendicular distance of $1.44\sin 107.9° + 0.37 = 1.74$ Å from the basal plane. The

average of the distance between the carbon sheet and oxygen atoms can be simply calculated as (1.57 + 1.74)/2 Å.

The interface between the GO sheet and the C-S-H matrix is difficult to model, due to the lack of data for the material composition near the interface. Figure 2.10 illustrates the nanostructure of GO C-S-H and especially the interface between the GO and the

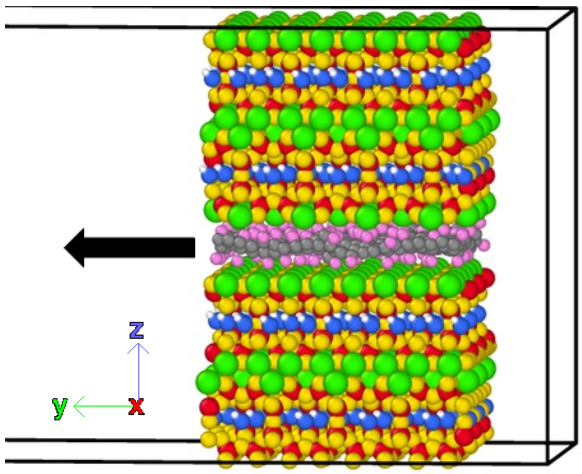

Figure 3.1 MD simulation cell for GO cement.

C-S-H (Pan et al., 2015). The functional groups of the GO sheet, mainly, oxygen atoms, react with the calcium atoms from the C-S-H and form a strong interface. To determine the distance between the calcium ion and the oxygen in carboxyl group, a DFT study was conducted by Mehandzhiyski and co-workers (Mehandzhiyski et al., 2015). The average length of the Ca-O bond is calculated as 2.17 Å. In addition, the average distance between the calcium layer and the carbon plane of the GO sheet can be obtained as 2.17 + 1.66 = 3.83 Å. Moreover, the distance between the two calcium layers, surrounding the GO sheet, can be derived as 3.83 × 2 = 7.66 Å.

The molecular structure of the GO reinforced C-S-H is shown in Figure 3.1 MD simulation cell for GO cement.

. Vacuum space is set for technically allowing pulling out the GO sheet without extending the simulation box. In Fig. 3, the blue1 atoms represent oxygen in the water, the white atoms are hydrogen in water, and the green atoms represent calcium; the

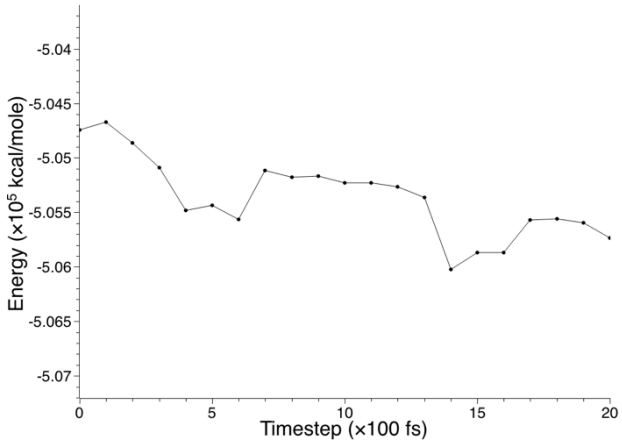

Figure 3.2 Energy – timestep curve during relaxation in pull-out process.

yellow atoms represent oxygen and the red atoms are silica, which form the silica chains, and the grey atoms are carbon and the pink atoms are oxygen forming the GO sheet. Periodic boundary conditions are applied in the x-z plane. The procedure to produce the molecular structure of GO C-S-H is as follows: a unit cell of C-S-H, which has the lattice parameters of a = 11.265 Å, b = 7.386 Å and c = 10.931 Å with space group F2dd (Merlino et al., 2001), is duplicated as 3 × 4 × 1 along x-, y-, z-directions, respectively.

The initial structure was relaxed for 50 ps in the isobaric-isothermal (NPT) ensemble. The Nosé-Hoover thermostat is used to keep the temperature at 300 K, and the

Nosé-Hoover barostat is used to maintain the pressure at p = 0 Pa. This was followed by a 50 ps run in the canonical (NVT) ensemble for a single layer of atoms where the Ca, Si, and oxygen in C-S-H are fixed. A time step of $\Delta t = 0.25$ fs was used during the entire relaxation.

After the initial relaxation, the system was subjected to the pull-out test. The outermost layer of atoms in C-S-H along y-direction was held fixed, while the outermost layer of carbon atoms (14 C atoms in total) in the GO sheet along y-direction was moved in the y-direction at a constant rate. Three pulling rates of the GO sheet were adopted: 0.0016 Å ps^{-1}, 0.008 Å ps-^{1} and 0.08 Å ps^{-1} . After every 0.4 Å pulling displacement of the GO sheet, the system was relaxed for 2 ps. The relaxation period is chosen from the literature [38]. A typical energy variation with time is shown in Figure 3.2, in which an equilibrium or a convergence trend to be achieved. The data were recorded during the relaxation before the next pull-out step was applied. A cell incorporating a pure graphene sheet without functional groups was also established for the pull-out test, in light of comparing with the GO cement and examining the effects of functional groups on the interfacial mechanical properties. The interaction energy between GO sheet and C-S-H is calculated and discussed, which represents the energy of the interface. The energy of the carbon atoms from the GO sheet is also derived as a function of pulling displacement under various pulling rates.

3.3 Interfacial Force

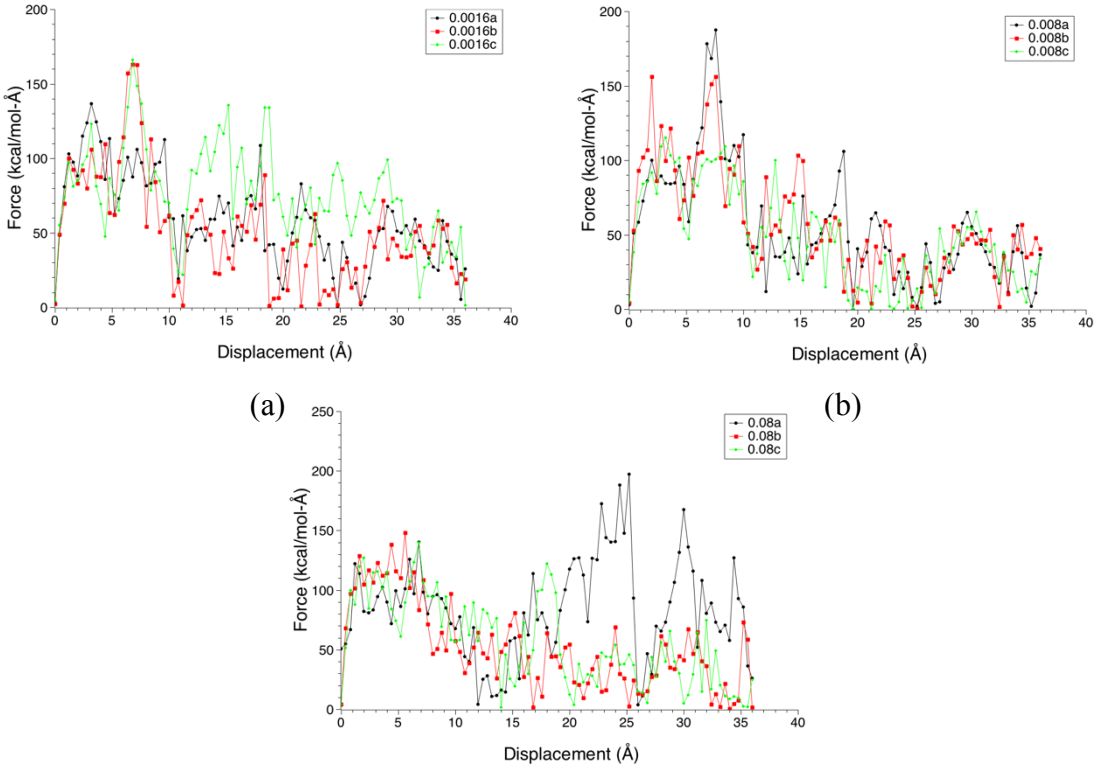

Figure 3.3 Pull-out force-displacement curves of GO cement under a pulling rate of: (a) 0.0016 Å ps^{-1}, (b) 0.008 Å ps^{-1} and (c) 0.08 Å ps^{-1}.

The relationship between the total force on the moving carbon atoms along pull-out direction (y-direction) F_Y and the pull-out displacement for different loading rates are shown in Figure 3.3. According to Eq. (2-2), the force F_i exerted on atom *i* is given by $F_i = -\frac{\partial E_i}{\partial r_i}$, where E_i is the interaction energy for atom i, and r_i is the position of atom *i*. The total force *F* on the fixed atoms is calculated by $F = \sum F_i$. Therefore, the force is directly related to the interfacial stress transfer and can be used as the basis to derive the interfacial shear strength of the nanocomposite.

Figure 3.3 shows the results for three groups of pull-out tests with different pulling rates of the GO sheet (0.0016 Å ps^{-1}, 0.008 Å ps^{-1} and 0.08 Å ps^{-1}, respectively). For each loading rate, three tests/simulations, as represented by ‘‘a”, ‘‘b”, and ‘‘c” in the figures, were carried out to examine the repeatability and reliability of the results. For all three loading rates, the results show no significant difference for the initial elastic development (i.e., no bonds are broken). The force then starts to fluctuate once bonds are stretched too much, and bond breaking/reformation occurs. In

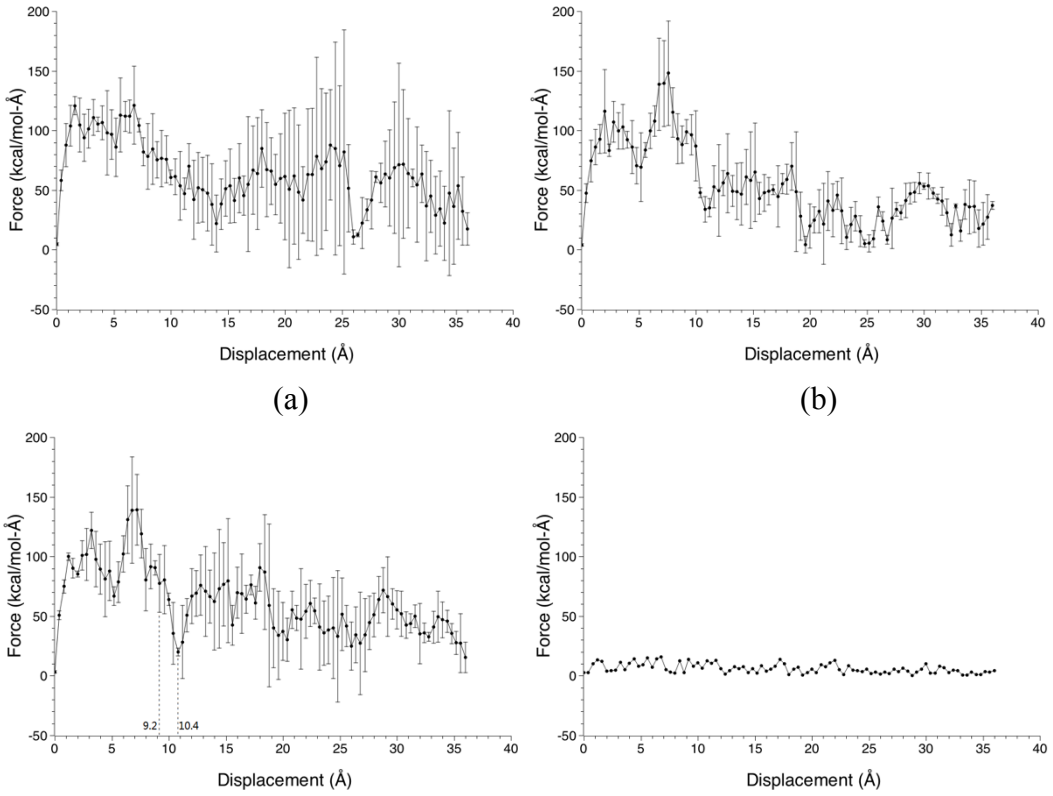

Figure 3.4 Averaged force-displacement curve of GO cement with the pulling rate of: (a) 0.0016 Å ps^{-1}, (b) 0.008 Å ps^{-1} (c)0.08 Å ps^{-1} and (d) graphene pulled out from cement with a pulling rate of 0.08 Å ps^{-1}.

addition, the force-displacement relation under the loading rate of 0.08 Å ps^{-1} has the largest fluctuation, especially for the later pulling out stage, while the force-displacement relation under the other loading rates has the smallest fluctuations. All three curves for each loading rate are quite close to each other.

Figure 3.4 shows the average force-displacement response; the error bars in Figure 3.4(a)-(c) from each loading rate are taken as the standard deviation of the data in Figure 3.3(a)-(c). Although the loading rate 0.08 Å ps^{-1} has slightly more fluctuations in the load-displacement curve, the overall/averaged mechanical performance for all these three loading rates are similar. The averaged pull-out forces are almost the same until about 10 Å, after which there are slightly more differences. Nevertheless, the first 10 Å displacement represents the initial cycle of the elastic-plastic-fracture phenomenon and thus is more important than the following force development in the context of engineering applications. It can be seen in Figure 3.4(a)-(c) that three peaks of the forces, representing three cycles of force development, are present during the process of pulling out the GO sheet from the C-S-H matrix. In the first 2 Å displacement, the force increases rapidly, mainly due to the initial elongation of C-O-Ca bonds. The force fluctuation follows before it reaches its highest value (e.g., 140 kcal $mol^{-1}Å^{-1}$ for 0.0016 Å ps^{-1} loading rate). In this period, most of the bonds between the GO sheet and the C-S-H are still intact, although some of have broken. After the peak load, the force abruptly drops to 19.9 kcal $mol^{-1}Å^{-1}$ for the loading

rate of 0.0016 Å ps^{-1}. During this stage, most bonds at the interface are broken. Meanwhile, new bonds are generated during the relaxation in the displacement range of 9.2-10.4 Å. The whole period up to 10.4 Å displacement represents a complete and initial cycle of the shearing load development at the interface (i.e., an initial increase, a kind of interesting yielding phase prior to the peak load and a decrease/softening phase until a small residual value). As mentioned, such an elastic-plastic-fracture phenomenon has been first observed at the nanoscale for GO cement composite and not yet been seen in the macroscale mechanical property.

After the first complete cycle of the shearing load development at the interface, the GO continues to be pulled out while new bonds are being created. For example, during the displacement from 10.4 Å to 18 Å under the 0.0016 Å ps^{-1} loading rate, the force increases again up to 90.8 kcal $mol^{-1}Å^{-1}$, which is then followed by a rapid decrease to 30.3 kcal $mol^{-1}Å^{-1}$ at 20.4 Å displacement. The maximum force is smaller than that of the first cycle. The reduction is mainly caused by the 12 Å length of GO sheet, which has been pulled out of the C-S-H matrix, resulting in fewer C-O-Ca bonds being generated. The rapid increase in energy around 18 Å also shows the generation of bonds, as illustrated in Figure 3.4(a). After the second drop to the lower level, the force distribution begins to fluctuate significantly; about half length of the GO sheet has been pulled out of the original position, thus the short-range interaction between the GO and the C-S-H contributes less and less in the following

period, making the energy distribution in the interface more complex and changeable. The third cycle starts from 26 Å and terminates at 36 Å with a peak force of 71.6 kcal $mol^{-1}Å^{-1}$ at 28.8 Å pull-out displacement. At this stage, the GO has been completely pulled out of the C-S-H matrix.

According to Amonton's law of adhesion (Gao et al., 2004), the friction force F is divided into two parts: $F = \mu L + F_0$, the external normal force L multiplied by the friction coefficient μ and the internal force F_0 impacted by the adhesion between the two surfaces. In this study, L continuously decreases due to the reduction of the contact surface; the internal force F_0 should initially increase because of bond stretching and then decrease due to bond breakage. The force-displacement generally follows Amonton's law for individual cycles. The simulations clearly show both the chemical interaction (i.e. bonding) and the physical interaction occurring at the interface between the GO and the C-S-H.

To investigate the influence of the oxygen functional group on the interfacial mechanical performance of GO cement, the pull-out test was conducted for pure graphene cement composite. At the interface between the pure graphene sheet and the C-S-H, there is no chemical or short-range interaction and only long range interaction remains. Figure 3.4(d) shows the force-displacement curve for pure graphene without functional groups under a pulling rate of 0.08 Å ps^{-1}. The force remains relatively constant, with a maximum value of about 16 kcal $mol^{-1}Å^{-1}$. The

peaks keep decreasing until it is completely pulled from the C-S-H matrix. This demonstrates that the chemical bonds formed between the C-S-H and GO have significantly increased the shearing force transferring capacity, about 8.5 times for the maximum force.

3.4 Interfacial Energy

The interfacial interaction energy ΔE is an important parameter that reflects the energy state for the interface between GO and C-S- H, which can be defined as follows:

$$\Delta E = E_{Total} - E_{GO} - E_{C-S-H} \quad (3\text{-}1)$$

where E_{Total} is the potential energy of the whole system, E_{GO} is the potential energy of all the atoms in the GO sheet alone (i.e., C-C bonds and C-O bonds) and $E_{C\text{-}S\text{-}H}$ is the potential energy of C-S-H alone. The interaction energy represents the interfacial

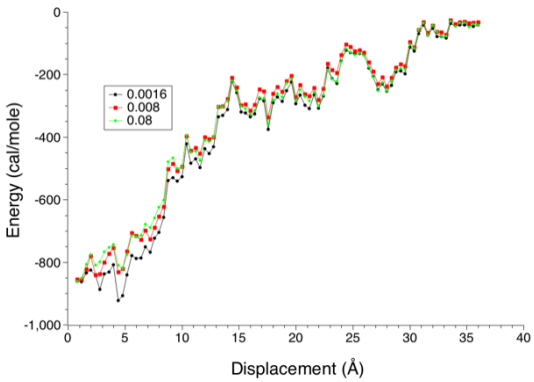

Figure 3.5 Interaction energy-displacement curves of GO cement with various pulling rates.

energy including the binding effect of oxygen as function groups.

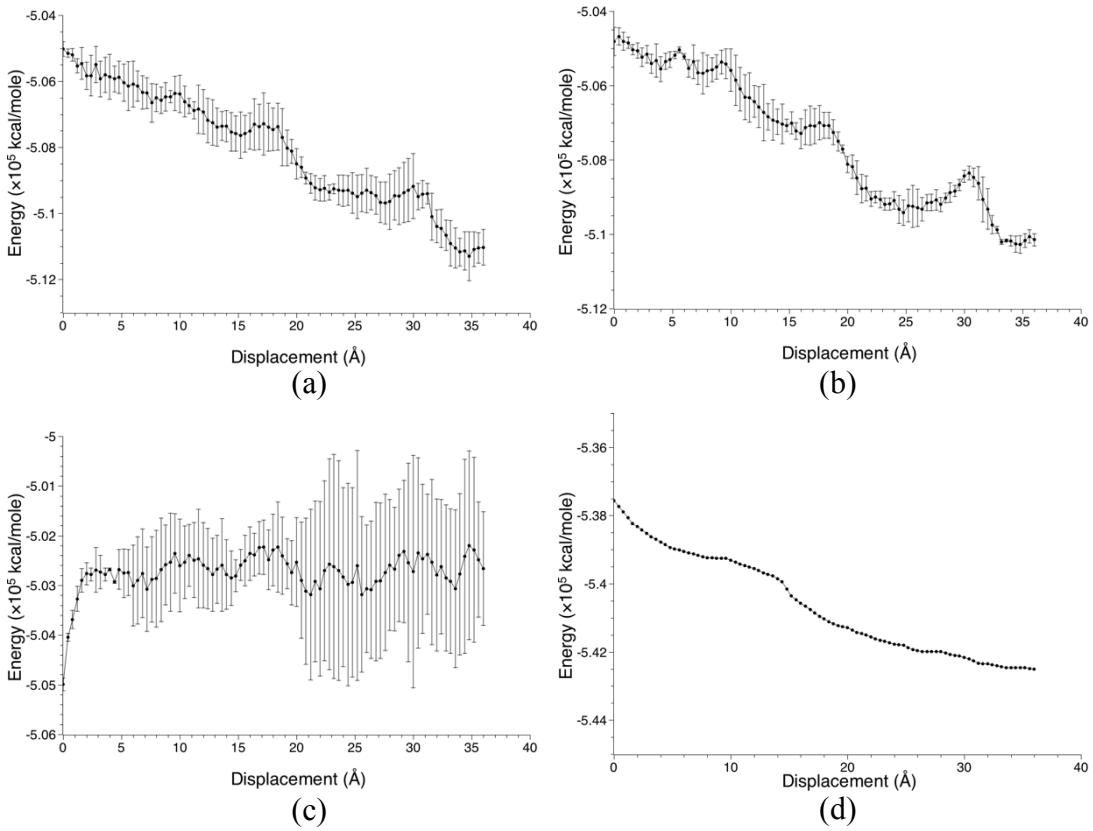

Figure 3.6 Averaged energy of carbon atoms as a function of pull-out displacement of GO cement with a pulling rate of: (a) 0.0016 Å ps^{-1} (b) 0.008 Å ps^{-1} (c) 0.08 Å ps^{-1} and (d) graphene pulled out from cement with a pulling rate of 0.08 Å ps^{-1}

Figure 3.5 shows the interaction energy as a function of the pull-out displacement for different loading rates. It should be noted that the energy is shown with a sign, so the energy is actually decreasing rather than increasing in magnitude. The interfacial energy decreases from 850 cal mol^{-1} to around 50 kcal mol^{-1} during the pull-out process. The energy loss of the interface is mainly caused by the reduction of Ca-O-C chemical bonds. In Figure 3.5, all three curves are initially constant for about

4Å and then gradual decrease. This demonstrates that there is no breakage of chemical bonds during the first 4 Å of displacement. Further, the effect of the loading rates on the change of interfacial energy is minimal.

The energies of all the carbon atoms in the GO sheet for different loading scenarios are presented in Figure 3.6(a)-(c). The energy of all carbon atoms conforms to the trend of consistent increase in general for pulling rates of 0.0016 Å ps^{-1} and 0.008 Å ps^{-1}, despite some local decreases at certain loading stages; there are three local decreases in the energy of all the carbon atoms, and the three lowest local energies are exactly corresponding to the three force peaks as illustrated in Figure 3.4(a), around 7 Å, 18 Å and 29 Å respectively, for the 0.0016 Å ps^{-1} pulling rate. Three tests were performed for each loading rate, and the trend was clear and stable. This suggests that these two pulling rates are suitable for pull-out test on GO cement composites. However, the trend for the energy variation at the pulling rate of 0.08 Å ps^{-1} is unstable (see Figure 3.6 (c)), and the error bars for most of the curve are considerably larger. Compared to the energy variation of a graphene sheet pulled out from C-S-H with a pulling rate 0.08 Å ps^{-1} (see Figure 3.6 (d)), it can be confirmed that the oxygen atoms in GO sheet significantly influence the pull-out process when the pulling rate is high. Therefore, the choice of a proper loading rate for the pull-out test is key to reliable MD simulation. A similar observation was made by Hou et al.

(2014c), where different pulling rates changed the material properties simulated from plastic to elastic.

3.5 Interfacial Shear Stress

With the pull-out force recorded, the pull-out shear stress can be calculated as (Boresi et al., 1993):

$$\tau = \frac{F}{A} \tag{3-2}$$

where F is the pull-out force, and A is the force-resisting area. The shear stress s can be re-written as:

$$\tau = \frac{F}{A_{GO-CSH}} = \frac{F}{2[a_0 \times (b_0 - \Delta b)]} \tag{3-3}$$

where $A_{GO\text{-}CSH}$ is the force-resisting area in the interface of C-S-H and GO sheet, a_0 is the length of GO sheet vertical to the pull-out direction, b_0 is the width of GO sheet along the pull-out direction, and Δb is the pull-out distance of the GO sheet. In this model, a_0 = 32.13Å and b_0= 27.124 Å.

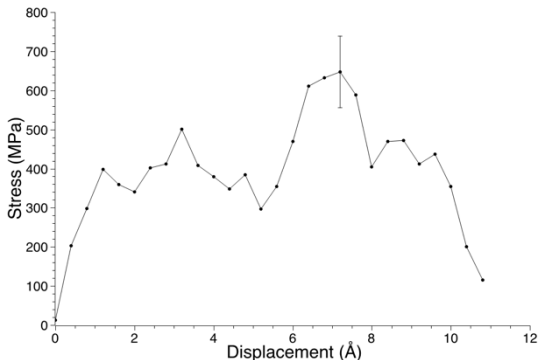

Figure 3.7 Average shear stress-displacement curve for GO cement.

There are two sides of the GO sheet which are in shear, so the force-resisting area is the double of the area of the GO sheet connecting to the C-S-H. By using Eq.3-3 and the values of a_0 and b_0 given above, the shear stress can be calculated as a function of the pull-out displacement for the first cycle. The pulling rate of 0.0016 Å ps^{-1} is chosen. This relationship is shown in Figure 3.7. It can be seen that the shear stress increases roughly until 400 MPa; the stress then fluctuates over the next about 4 Å displacement until the maximum shear stress is reached (i.e., 647.58±91.18 MPa obtained from different pulling rates). It is very interesting to find this fluctuation is similar to stress yielding behaviour which has not been commonly seen in macroscale stress analysis. This stress yielding phase is then followed by stress softening (i.e., stress decrease), which usually implies damage has occurred. During the stress softening phase, the stress suddenly drops to around 400 MPa and gradually decreases. This is similar to what have been found in the macroscale Mode I and II fractures of cement, which has often been simplified to a bilinear softening curve. At about 10 Å displacement, the shear stress drops to about 100 MPa which is comparable to that of the pure graphene case.

The interfacial shear strength is calculated to be about 647.58±91.18 MPa. As a general comparison, the tensile strength of the pure graphene sheet is about 130 GPa (Lee et al., 2008), and the shear strength of Portland cement is typically in the range of 6–35 MPa at the macroscale (Moosavi and Bawden, 2003). It would be extremely

to verify the results by comparing with experimental data; however, none is currently available. As explained, this is probably because there is no experimental method available for capturing the interfacial stress of the GO cement at the nanoscale. However, this further increases the necessity of predicting the interfacial mechanical properties by numerical approaches. It would be very useful to have the nanoscale bond-slip relation including the shear strength for GO cement which can be used as the inputs for multi-scale modelling or to be upscaled to the engineering scale.

The shear stress-displacement, often known as bond-slip relation, is for the first time derived for GO cement. It has significant impact on multi-scale modelling (e.g., finite element simulation) in terms of the interface properties. The properties for interface elements in finite element analysis are usually not available due to the difficulties of experiments. This is why trial and error analysis are applied for determining the interfacial properties. The shear stress-displacement curve derived can well be used for defining the bond-slip behaviour in the interface elements in multi-scale numerical simulation and also be upscaled to the engineering properties at the macroscale.

3.6 Conclusions

In this chapter, the nano interface between the C-S-H and GO has been modeled and the complete stress transferring mechanism has been studied using MD. The

structures for the GO and the C-S-H have been clearly presented, and pull-out tests were carried out in a realistic manner. ReaxFF was employed to provide the interactive potentials for the whole molecular system. Three different pulling rates were employed in running the MD simulations and it has been found that 0.08 Å ps-1 leads to larger fluctuation in the force-displacement curve, compared with 0.0016 Å ps-1 and 0.008 Å ps-1, especially for the later pulling out stage. The full stress displacement curve which represents the mechanical properties of the GO cement interface has been derived and the shear strength has been found to be 647.58±91.18 MPa. The shear stress-displacement curve has, for the first time, been derived for GO cement which represents the bond-slip relation in finite element simulation. It can be concluded that MD simulation offers a unique insight into modelling the nanoscale mechanical properties of cementitious nanocomposites which have not, yet, been determined by experiment.

Chapter 4.
Mechanical Properties of C-S-H Globules and Interface

4.1 Introduction

Recently, there is a growing research interest in modelling the atomic structure and investigating the nano/microscopic properties of cement (Bernard et al., 2003, Feng and Christian, 2007, Haecker et al., 2005, Ulm et al., 2004, Wu et al., 2010). In light of difficulties in conducting experimental tests at the nano/micro-scale level, atomic modelling provides a unique view in understanding the fundamental behaviour, especially mechanical properties, of the cementitious materials.

C-S-H gel is known as imperfect crystalline and a close analogue of Tobermorite and Jennite minerals. In the past three decades, a number of crystalline models for C-S-H structure were identified or developed, based on the well-known Tobermorite and/or Jennite structures (Taylor, 1986, Makar and Chan, 2009, Richardson and Groves, 1992, Richardson, 2004, Moon et al., 2015, Hamid, 1981, Rejmak et al., 2012). 14 Å Tobermorite and Jennite are the most common crystalline phases presented, whereas the modelling of the real imperfect crystalline structure of the C-S-H gel is tremendously challenging. Generally, the C-S-H structure can be characterized in terms of calcium/silicon (Ca/Si) ratio which normally ranges from 0.6 to 2.3 (Selvam et al., 2009). 14 Å Torbermorite has a chemical formula $Ca_5Si_6O_{16}(OH)_2 \cdot 7H_2O$ and a density of 2.18g/cm^3. Typical Jennite has a Ca/Si ratio of 1.5, a density of 2.27 g/cm^3 and a formula $Ca_9Si_6O_{18}(OH)_6 \cdot 8H_2O$ (Taylor, 1997). Accordingly, Richardson (2004) has developed Tobermorite/Jennite (T/J) model and Tobermorite/Calcium Hydroxide

(T/CH) model for C-S-H. The T/J model is a combined Tobermorite and Jennite domains while the T/CH model contains Tobermorite silicate chains sandwiching calcium hydroxide, providing higher Ca/Si ratios. Another widely-cited C-S-H model is the so-called realistic molecular structure of C-S-H, developed by Pellenq and his co-workers (Pellenq et al., 2009). This model has defected silicate chains, consisting of silicate monomers, dimers and pentamers. It has a Ca/Si ratio of 1.65 which is close to the recent experimental findings, i.e., $(CaO)_{1.7}(SiO_2)(H_2O)_{1.80}$, by neutron scattering measurements (Allen et al., 2007). They postulated that the Ca/Si ratio remains the most important parameter in any model construction of C-S-H. Moreover, Richardson (2014) developed a series of models for C-S-H with Ca/Si lower than 1.4 representing different mean chain lengths using crystal-chemical and geometrical reasoning.

Based on the C-S-H models, atomic simulation, mainly through MD modelling, have been conducted in recent years to determine the mechanical properties of C-S-H. Al-Ostaz et al. (2010) simulated the mechanical properties of the 14 Å Tobermorite, Jennite and calcium hydroxide. They have found that the force field chosen and size of simulation box affected the results. For example, different force fields resulted in different mechanical properties. Moreover, the C-S-H unit needed to be duplicated 3×3×3 to match the experimental mechanical properties for initial MD modeling as the mechanical properties of the original unit and 2×2×2 supercell were not very close to the experimental data. Moreover, Hou et al. (2014d) modeled the C-S-H structure

based on the 11Å Tobermorite (Janik et al., 2001) with ClayFF force field bnmnatoms in the interlayer on the mechanical properties of C-S-H. Other than elastic properties, MD simulation can also be employed to study the fracture properties of cement at the nanoscale. A similar structure as proposed in Pellenq et al. (2009) was used and duplicated several times to form a cube with the size of 13.8 nm; direct tension was then applied to investigate the Mode I fracture of C-S-H under CSHFF force field (Hou et al., 2014c). It has been found that Ca-O and Si-O bonds were provided to contribute the most cohesive force on xy plane, and weaker H- bonds bind the structure on z plane. In addition, size effects have been shown as result of different size of the central voids made by deleting different number of atoms, on weakening stiffness and cohesive force of C-S-H. Further, fracture toughness of C-S-H were evaluated by MD simulations, and the brittleness was discussed in comparison with other brittle materials at the atomic scale (Bauchy et al., 2015).

When the structure of C-S-H evolves from nanoscale to mesoscale, it is much more unclear. There are perhaps only two widely acknowledged models, namely, Colloidal model (Jennings, 2000, Jennings, 2008) and Feldman-Sereda model (Feldman and Sereda, 1970), to describe the mesostructure of C-S-H. In Jenning's Colloidal model, a globule (about 4.2nm) forms the basic unit cell which is a discrete nano particle; the globules are not linked together but packed randomly with water molecules and voids. In Feldman-Serada model, however, long layers of C-S-H are well aligned and extend

from one nanocrystalline region to another. The 4.2nm unit cell (globule) of C-S-H in the Colloidal model has four or five layers of silicate chains, sandwiching Calcium ions, water molecules and possibly pores. The unit cell then discretely joins each other in different directions to form the mesostructure of C-S-H. To simulate the mesoscale mechanical properties of C-S-H, granular mechanics would be of much interest; however, the mechanical properties of the globule itself and the interfaces on the joining surfaces of these nanostructure cells would need to be obtained in advance. This chapter attempts to determine the basic mechanical properties of the globule of C-S-H and the interfaces of the globules in terms of different water contents. The atomic structure of C-S-H in Richardson (2004) and the ReaxFF force field are employed in the molecular dynamics simulation.

4.2 Methodology

4.2.1 C-S-H Globules

The atomic structures of C-S-H used in this chapter are chosen from Richardson (Richardson, 2014), i.e., T2_ac and T11_14sc. T2_ac is a double-chain Tobermorite-based monoclinic structure, derived from Merlino et al. (2000) in which all the interlayer Ca atoms are in octahedral coordination with oxygen atoms in silicate chains, as shown in Figure 4.1.

(a). T11_14sc is also a Tobermorite-based monoclinic structure but the mean length of silicate chains is 11 Å, and the layer spacing is 14 Å, as presented in Figure 4.1.

(c). Based on these two structures, two orthorhombic structures are generated (Figure

4.1 Molecular structures of five different C-S-H unit. Green atoms are Calcium, cantaloupe atoms are Silicon, red atoms are Oxygen and white atoms are Hydrogen.

(b) and (d)). Moreover, in Jennings's Colloidal model intraglobular pores (IGP) may exist in the unit cell of globule and the effects of I GP have not been addressed or simulated yet. In this chapter, a structure containing IGP is produced as shown in

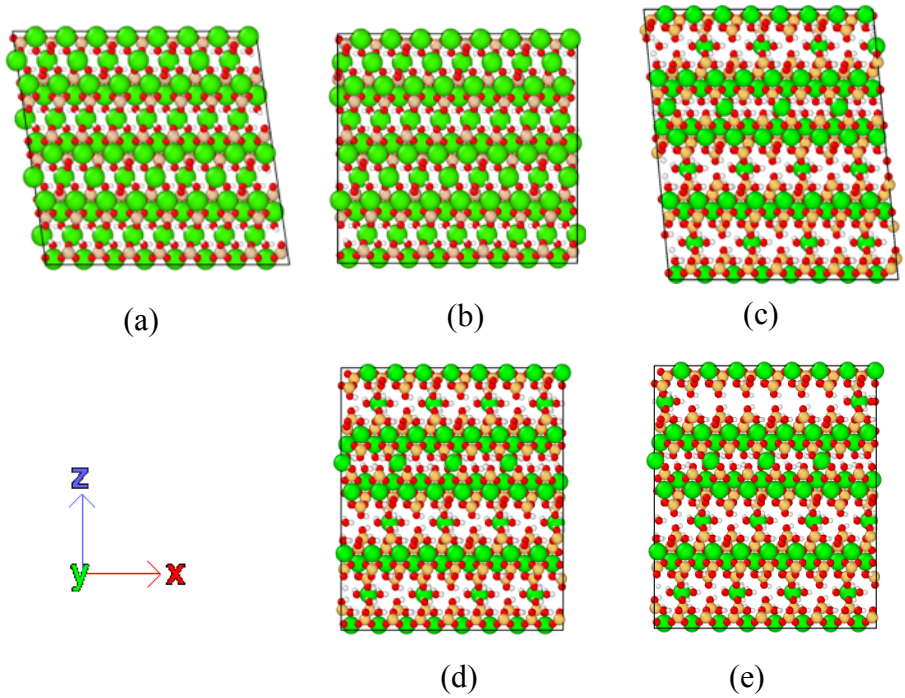

Figure 4.1 Molecular structures of five different C-S-H unit. Green atoms are Calcium, cantaloupe atoms are Silicon, red atoms are Oxygen and white atoms are Hydrogen.

Figure 4.1(e). And the characteristics of all five models is listed in Table 4.1. All structures are tested under uniaxial tension along y- and z- axis.

For T2_ac molecular structure with chemical formula $Ca_4H_2(Si_2O_7)_2Ca_4H_20$, the lattice parameters of a = 11.35 Å, b = 7.3 Å, c = 21.5 Å and β = 98.4° with space group C12/c1 are duplicated as 4 × 6 × 2 along x-, y-, z- directions, respectively, to generate Model I; the structure is then changed to orthorhombic structure, where the volume, density, atom position and bonds information are kept the same, as named Model II. For T11_14sc molecular structure with chemical formula $Ca_9(Si_{11}O_{28}(OH)_6)(H2O)_{7.25}$, the lattice parameters of a = 11.35 Å, b = 7.3 Å, c = 52.7 Å and β = 95.5° with space group C1 are duplicated as 4 × 6 × 2 supercell along x-, y-, z- directions, respectively, to generate Model III; the structure is then changed to orthorhombic, namely, Model IV. Model V is the IGP structure. LAMMPS (Plimpton, 1995) is used to perform the MD simulations.

Table 4.1 Characteristics of the five models used in the simulation

Model Name	Original structures from Richardson (2014)	Supercell unit (Å×Å×Å)	Crystalline Structure	Mean length of silicate chain	Bridging tetrahedral connection
Model I	T2_ac	45.4×43.8×43, β = 98.4°	monoclinic	2 Å	adjacent
Model II	T2_ac	45.4×43.8×43	orthorhombic	2 Å	adjacent
Model III	T11_14sc	45.4×43.8×52.7, β = 95.5°	monoclinic	11 Å	staggered
Model IV	T11_14sc	45.4×43.8×52.7	orthorhombic	11 Å	staggered

Model V	T11_14sc	45.4×43.8×52.7	orthorhombic	11 Å	staggered

Model III and Model IV have advantages to be used as the basic structure to investigate the effects of IGP (Jennings, 2008) on the mechanical properties of C-S-H, since the interlayer Calcium atoms have the occupancy lower than 1.0 which can be arranged in MD simulation for a targeting structure. In this chapter, Model IV is modified by rearranging the first upper interlayer Calcium atoms in the unit with a number of water molecules to maintain appropriate Ca-O coordination number (Richardson, 2014), for a porosity of 10.43%, shown as Model V in Figure 4.1 Molecular structures of five different C-S-H unit. Green atoms are Calcium, cantaloupe atoms are Silicon, red atoms are Oxygen and white atoms are Hydrogen.

(e). All simulation boxes, i.e., Models I – V, are relaxed for 50 ps in the isobaric-isothermal ensemble (NPT) and coupled to zero external pressure in the x, y, z dimensions. The Nose-Hoover thermostat is used to keep the temperature at 300 K, and the Nose-Hoover barostat is used to maintain the pressure at p = 0Pa. After it reaches equilibrium, the system is subjected to the tensile load with a constant strain rate at 0.08 Å/ps. For the strain-stress relation along z-direction, the pressures in the x- and y-directions are kept at zero.

4.2.2 Interfaces between The Globules

Jennings's Colloidal model (2008) sheds light on simulating the mesoscale mechanical properties of C-S-H by using granular mechanics, i.e., discrete element method, or continuum mechanics, i.e., finite element method. No matter which

method is used to simulate the mesosystem of C-S-H, the interfacial properties between the unit globules should be known as a prior. To investigate the normal and

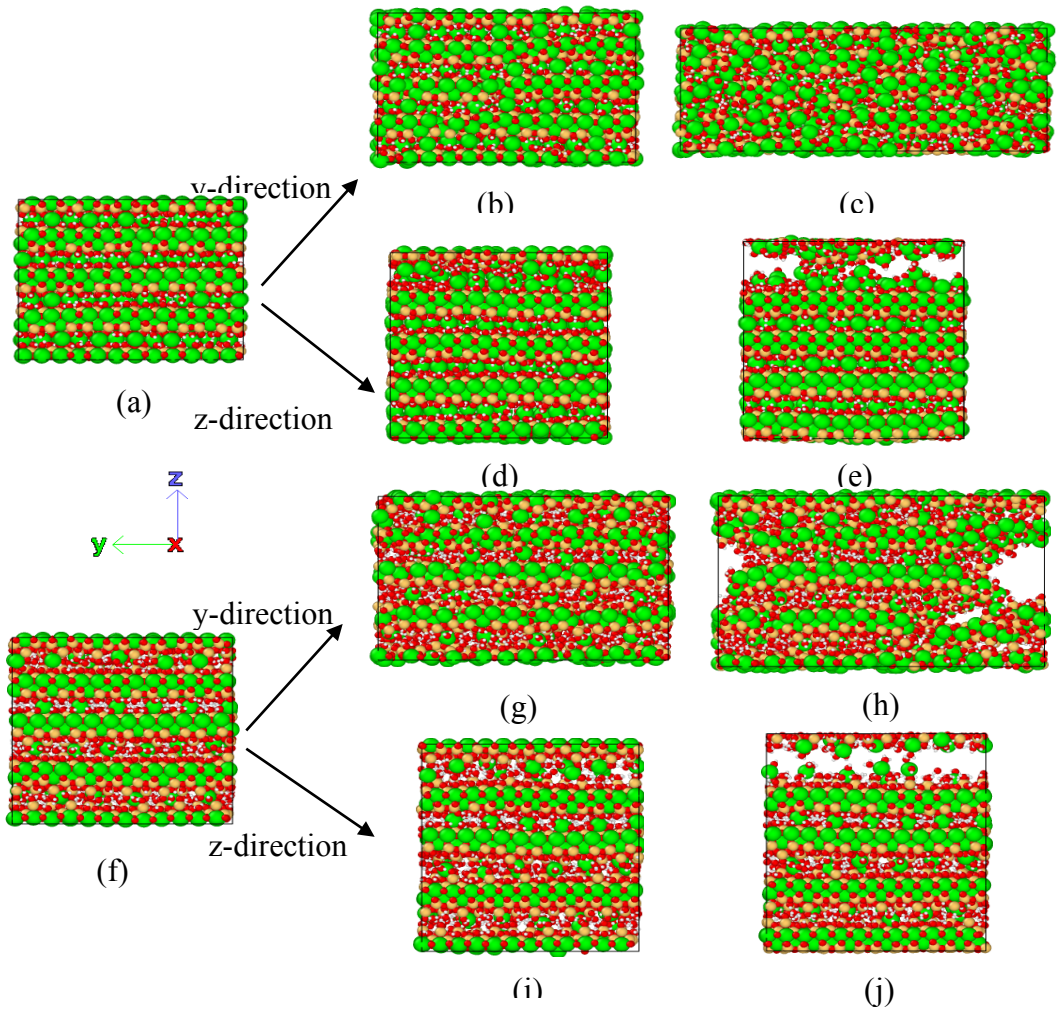

Figure 4.2 Tensile test simulation of Model I and Model III along z- and y- Directions. (a) Model I after equilibrium. (b) After the maximum value of the stress for Model I along y-direction. (c) The failure happens in Model I along y-direction. (d) After the maximum value of the stress for Model I along z-direction. (e) The failure happens in Model I along z-direction. (f) Model III after equilibrium. (g) Model III after the maximum value of the stress along y-direction. (h) The failure happens in Model I along y-direction, (i) After the maximum value of the stress for Model I in z-direction. (j) The failure happens in Model I along z-direction.

shear strengths at the interfaces in different directions, two supercells of Model IV are connected to each other along (100), (010) and (001) planes. Five different thicknesses of water layers are added to investigate the effect of water content on the interfacial properties, 0.0, 1.0, 2.0, 3.0, 4.0 Å, respectively. The density of water is 1 g/cm^3, and the Water/Si ratio for each model is 0.66, 0.86, 1.04, 1.25 and 1.37, respectively. The adsorption process of building the water interface between C-S-H globules is investigated by the grand canonical monte carlo (GCMC) method, in which the temperature, volume, and chemical potential are fixed. In the experimental setup, the adsorbed 'gas' is in equilibrium with the gas in the reservoir. The equilibrium conditions are that the temperature and chemical potential of the gas inside and outside the adsorbent must be equal. The gas that is in contact with the adsorbent can be considered as a reservoir that imposes a temperature and chemical potential on the adsorbed gas. Therefore, only the temperature and chemical potential of this reservoir determines the equilibrium concentration inside the adsorbent. At every step in the interface, moving a water molecule, creating a new water molecule or destroying an existing water molecule should be decided randomly. To satisfy the symmetry in the underlying transition matrix, it is required that the probability of creating a molecule is the same as that of destroying it immediately. The acceptance/rejection probability in Metropolis algorithm is shown in follow equation (Frenkel & Smit, 2001): $P_{acc} =$

$\min\left[1, \frac{V}{\Lambda(N+1)} exp\left(-\frac{\mu - E_N(N+1) + E_M(N)}{k_B T}\right)\right]$, where μ is the target chemical potential and N is the number of molecules while V is the system volume.

The simulation box is relaxed for 50 ps in the isobaric-isothermal ensemble (NPT) and coupled to zero external pressure in the x, y, z dimensions under temperature of 300 K. After that, the boundaries are changed to non-periodic and shrink-wrapped in three dimensions for the shear test a nd the microcanonical ensemble (NVE) is employed. During each shear test, the bottom atoms are fixed and the top atoms are loaded to move along the interface with a constant loading rate at 0.08 Å/ps. During each tensile test, the bottom is fixed, and the top is moved vertically to the interface with a constant loading rate of 0.08 Å/ps.

4.3 Mechanical Properties of C-S-H Globules

The complete tensile test simulations for the C-S-H globules along y- and z- directions (along silicate chains and normal to silicate chains respectively) are shown in Figure 4.2. In addition, the direct tensile stress-strain relationships obtained are shown in Figure 4.3. The stress shown here is the pressure P on the boundary of the whole C-S-H structure, and $P = \frac{N k_B T}{V} + \frac{\sum_i^{N'} r_i \cdot f_i}{dV}$, where N is the number of the atoms in the system, k_B is the Boltzmann constant, T is the temperature, d is the dimensionality of the system, V is volume, r_i and f_i are the position and force vector of atom i. In y-direction, all the five structures present linear increases in the initial elastic stage while Model I

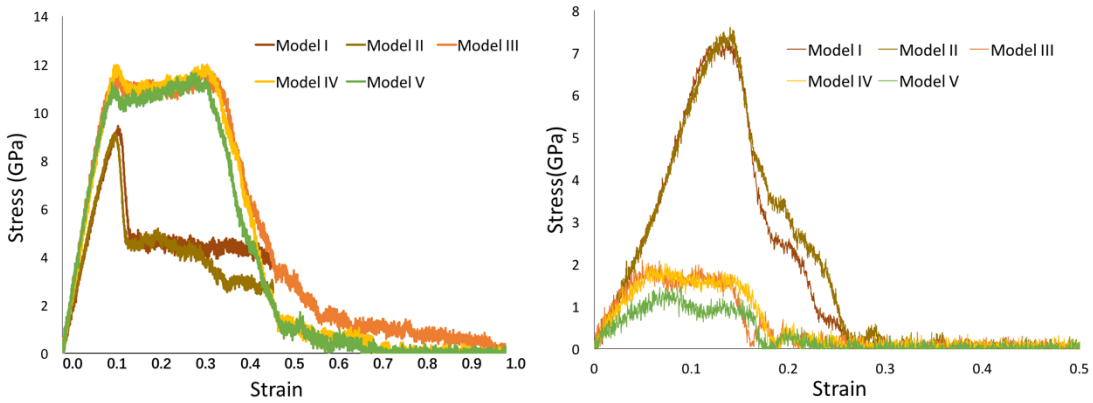

Figure 4.3 Stress-strain curves for five different C-S-H structrues along (a) y-direction (b) z-direction

and II have slightly lower elastic modulus than the other three structures. Model I and II have a very close tensile stress-strain relationship which has the maximum stress about 9 GPa at the strain of 0.11. These two structures are very brittle, since following the maximum value, the stress suddenly reduces to 4.5 GPa and keeps constant for the next 0.2 straining. It then gradually decreases until the complete separation. For Models III, IV and V, the stresses develop in similar trend and increase up to about 11 GPa. Different from Model I and II, these three structures undergo a clear ductile development before they gradually decrease. Such a ductile stage in the mechanical behaviour is caused by the longer mean length of the silica chains, which provide higher force carrying capability during tensile test along the y-direction. Moreover, it is interesting to find that the Model V (i.e., IGP structure) has some minor strength decrease at y-direction, compared with Models 3 and 4. This means the intralayer pores can slightly affect the mechanical properties in the silicate chain length direction.

It makes sense as the y-direction mechanism is mainly provided by the silicate chains which are not significantly affected by these pores. In z-direction which is the direction vertical to the silica chain, Models I and II have much higher strengths compared with Models III, IV and V. The stress-strain curves for Models I and II in z-direction are close to those in y-direction except for the softening pattern. However, the C-S-H structures of Models III – V have much lower strengths in z-direction in comparison with those in y-direction. This is because the interlayer Calcium and water interface in Models III – V provide a weaker connection compared to Model I and II, where the Calcium atom is in octahedral coordination with oxygen atoms resulting in much stronger interactions. Compared to Models III and IV, Model V (IGP structure) has much lower strength, i.e., 1.15GPa, while the Model III and IV go up to 1.9 GPa. It demonstrates that the existence of IGP can significantly reduce the strength of the C-S-H globules in the z-direction (i.e., the normal direction to the silicate chains).

Table 4.2 Simulated results for the mechanical properties of C-S-H nanostructures along y- and z- directions

	Modulus of Elasticity in y-direction (GPa)	Strength in y-direction (GPa)	Modulus of Elasticity in z-direction (GPa)	Strength in z-direction (GPa)
Model I	85.53	9.13	46.97	7.44
Model II	87.22	8.95	44.88	7.15
Model III	108.10	11.78	53.42	1.93

Model IV	112.71	11.17	51.29	1.92
Model V	116.8	10.94	38.39	1.15

The modulus of Elasticity calculated from the stress-strain curves and the maximum stress of each structure of C-S-H are shown inTable 4.2. The Young's modulus of the five structures along z-direction is in the range of 39 GPa to 54 GPa, which is reasonable compared to the experimental data of cements in range of 38 GPa to 56 GPa for wetted cement with low porosity and simulation data of tobermorite-like and jennite-like structures in range of 35 GPa to 56 GPa (Feldman, 1972, Manzano et al.,

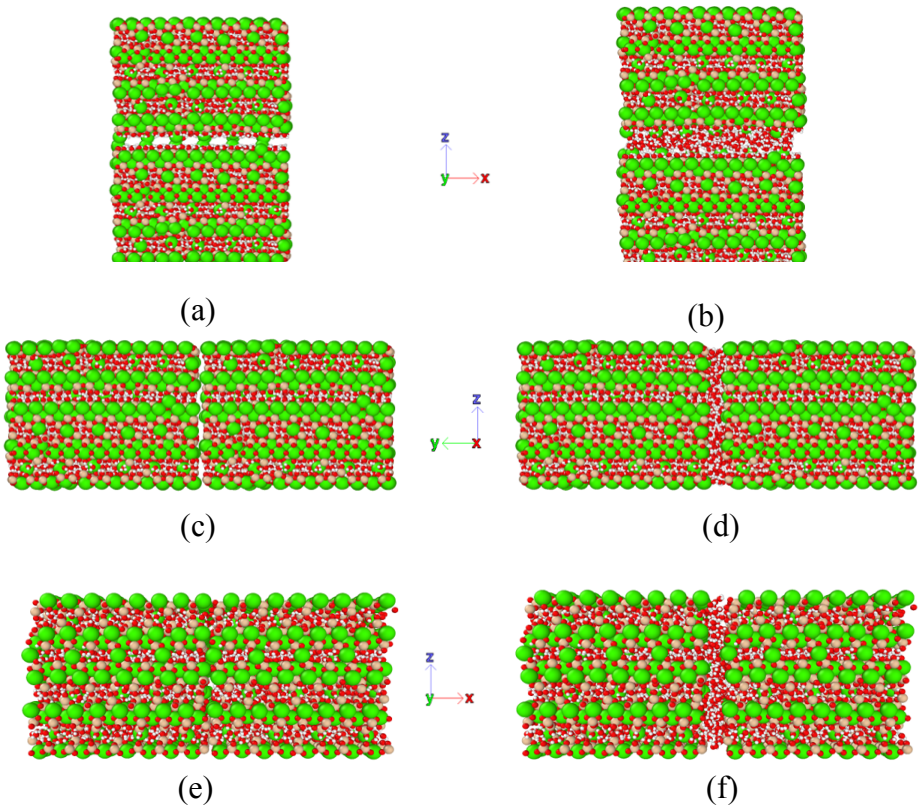

Figure 4.4 (a) (001) surface with 0 Å water layer (b) (001) surface with 2.0 Å water layer (c) (010) surface with 0 Å water layer (d) (010) surface with 2.0 Å water layer (e) (100) surface with 0 Å water layer (f) (100) surface with 2.0 Å water layer

2009). The strength of each structure is also in the reasonable range compared to tobermorite-like structure at about 1.4 GPa along z-direction and 9 GPa along y-direction (Hou et al., 2014a, Bauchy et al., 2015).The Young's modulus in y direction increases when the C-S-H gel changes to orthorhombic from monoclinic. By contrast, the strengths in y- and z-directions and Young's modulus in z-direction reduce for the orthorhombic structure. The change of crystal system has an impact on the mechanical properties; although the difference is not significantly large, it needs to be rigorous in establishing C-S-H structures. On the other hand, for some large-scale molecular system modelling or interfacial properties study, the structure will need to be changed slightly under duplication or packing or fitting in simulation box. Interestingly, Model V shows lower mechanical capacity, especially in z-direction, with 28% and 40% reduction for modulus of Elasticity and strength compared to Model III, respectively. Under loading the existence of IGP will cause rearrangement of Calcium in the interlayer.

4.4 Mechanical Properties of The C-S-H Interfaces under Tension Test

Figure 4.4 illustrates Model IV packed with 0 to 2 Å water layer interface on different surfaces of the globules, and the structure with W0, W5, W10, W15, W20 stand for the interface with a water layer of 0.0, 0.5, 1.0, 1.5, 2.0 Å added, respectively. According to Eq. (2-2), the force F_i exerted on atom i is given by $F_i = -\frac{\partial E_i}{\partial r_i}$, where E_i is the interaction energy for atom i, and r_i is the position of atom i. The total shear force F

on the fixed atoms is calculated by $F = \sum F_i$. The tensile force F is considered as being transferred to the interface between two C-S-H globules. The stress at the interface can be calculated as follows:

$$\sigma = \frac{F}{A} \tag{4-1}$$

where F is tensile force at the interface, and A is the force-resisting area. Due to the tensile test, the area in Equation (3) is kept constant, the tendency of the

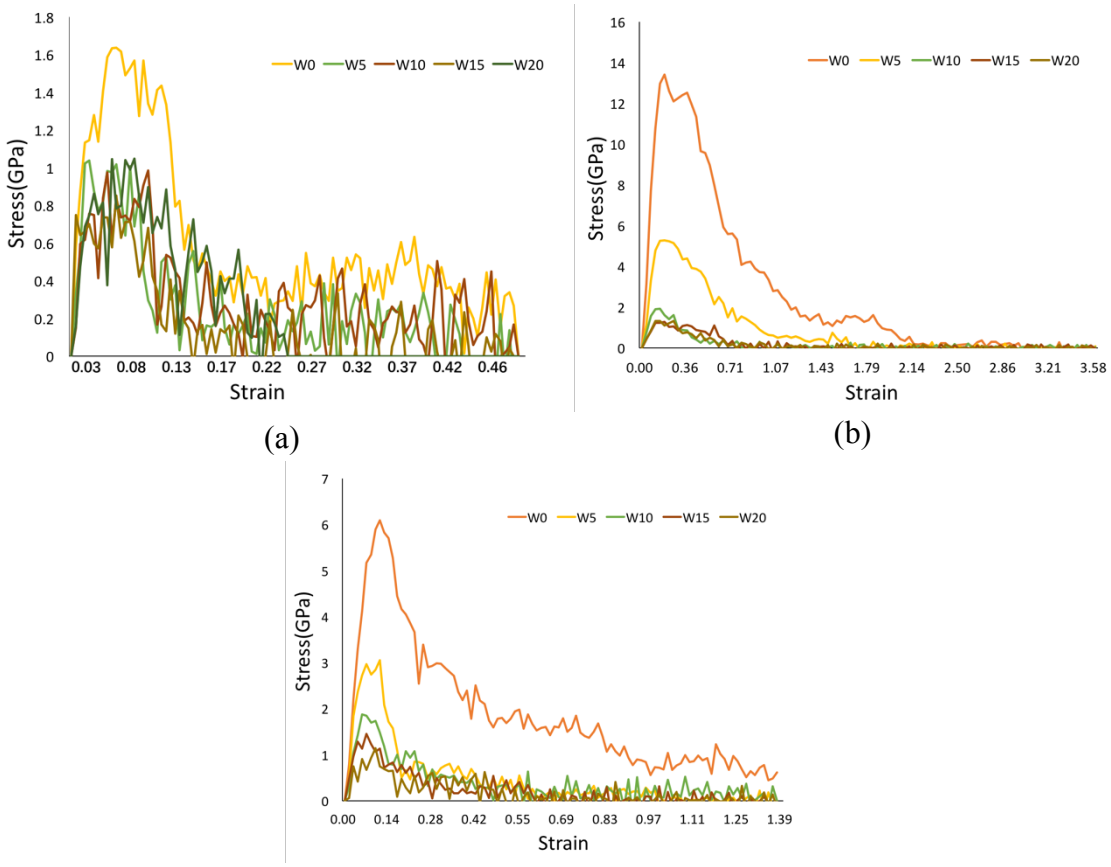

Figure 4.5 Tensile stress-strain curve for different water content in (a) (001) interface (b) (010) interface (c) (100) interface. W0, W5, W10, W15, W20 stand for the interface with a water layer of 0.0, 0.5, 1.0, 1.5, 2.0 Å added, respectively.

force-displacement and stress-strain curve is the same and only the stress-strain curves are shown in Figure 4.5.

For all three types of interfaces, the interface with no extra water molecules has greatest tensile strength compared to other structures with added water, because of the destructive effect of water on the bond generation between two C-S-H globules. For (001) interface, the stresses of other four structures with different amount of water molecules added present similar properties and there is no significant difference among the maximum value of stress, initial elastic stage and trend of the curve. For (010) and (100) interfaces, the slope of the initial elastic stage and the maximum value of stress both decrease with the increase of water content. The details of the tensile mechanical properties calculated from Figure 4.5 are shown in Table 4.3.

Table 4.3 Simulated results for the mechanical properties of the C-S-H interfaces along x-, y- and z- directions.

[001]	W0	W5	W10	W15	W20
Maximum Stress (GPa)	1.64	1.04	0.98	0.85	1.05
Young's modulus (GPa)	49.41	34.65	27.14	27.25	30.65
Fracture energy (J/m^2)	1.20	0.50	0.59	0.29	0.50
[010]					
Maximum Stress (GPa)	13.42	5.29	1.93	1.27	1.33
Young's modulus (GPa)	102.18	44.25	19.15	12.29	11.49
Fracture energy (J/m^2)	5.51	1.80	0.34	0.36	0.31

[100]					
Maximum Stress (GPa)	6.09	3.05	1.88	1.45	1.14
Young's modulus (GPa)	75.79	53.28	34.06	25.87	15.48
Fracture energy (J/m^2)	3.79	0.91	0.76	0.43	0.32

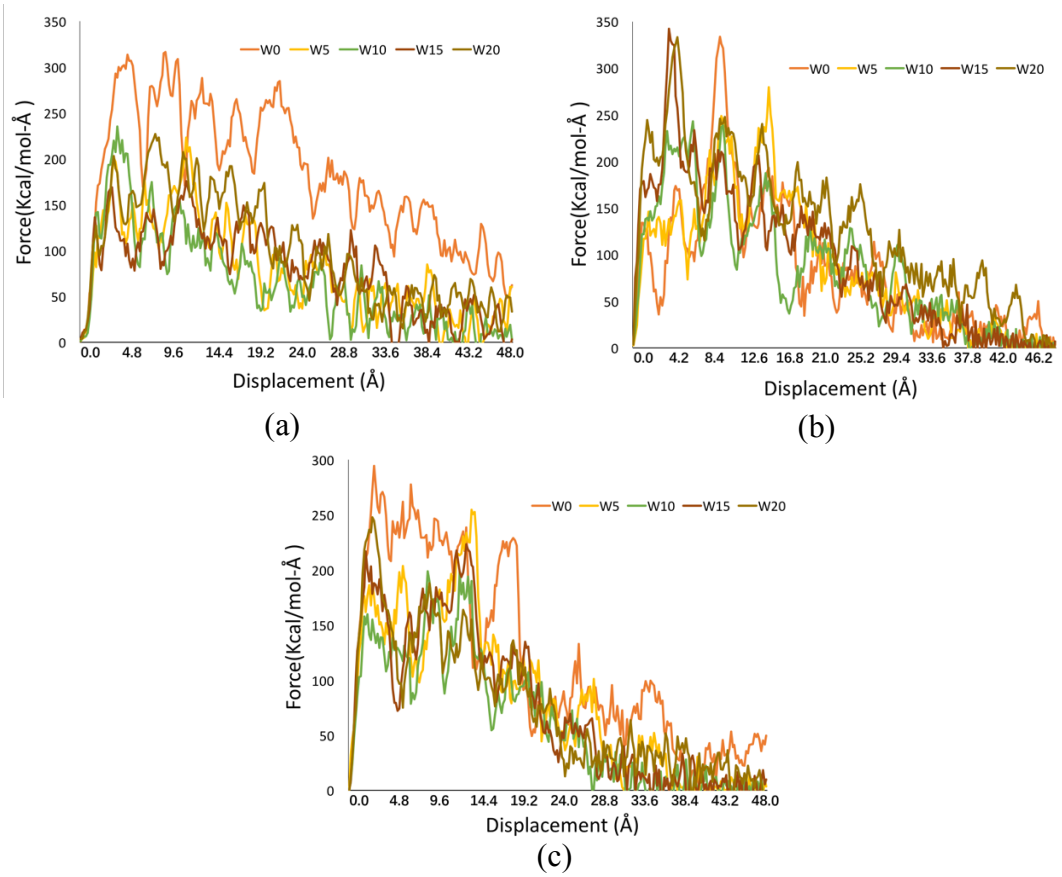

Figure 4.6 Shear force-displacement curve for different water content in (a) (001) interface (b) (010) interface (c) (100) interface

Young's modulus is defined by the slope of the initial elastic stage. Compared to the mechanism analysis of C-S-H globules during compressing test, the results in this study cover different Young's modulus between C-S-H interfaces in range of 10 GPa to 37 GPa in three elastic stage under compression (Suzuki et al., 2016). Young's modulus is defined by the slope of the initial elastic stage. The fracture energy G_F is

determined from the area under the stress-strain curves in Figure 4.5, multiplied by the initial length of the simulation box. For (001) surface, with water molecules added, the maximum stress, Young's modulus and fracture energy show no significant difference among different water content. For (010) and (100) surfaces, the maximum stress and Young's modulus decrease with the increase of water molecules. The minimum values of the fracture energy in three interface types all show in the structure with 2.0 Å and 1.5 Å water layer. It is interesting that the maximum value of stress and Young's modulus of W0 structure in (010) interface are almost the same as the value of Model III along y-direction in Table 4.1, because Reaxff allows bond breakage and generation so that the interface reconnects as one C-S-H unit during equilibrium to form the original structure. In order to obtain the parameters for further simulation such as FEM and DEM, the results in (001) interface are chosen, because it is the natural cleavage plane which is also the weakest layer in the C-S-H structure (Manzano et al., 2017). The tensile properties are calculated by the average of four structures with extra water molecules as: $\sigma_{max} = 0.98 \pm 0.09$ Gpa ; Young's modulus $E = 29.92 \pm 3.55$ GPa; Fracture energy $G_F = 0.47 \pm 0.13\ J/m^2$.

4.5 Mechanical Properties of The C-S-H Interfaces under Shear Test

The shear properties for the interfaces of C-S-H globules with different water content are also simulated and the shear force – displacement curves are shown in Figure 4.6. The shear force F is directly related to the interfacial stress transfer and can be used as

the basis to derive the interfacial shear strength of the globule interfaces. Figure 4.6(a)-(c) show the relation between the shear force along moving direction *F* and the shear displacement for different thickness of water layers for the three types of interfaces. W0, W5, W10, W15, W20 stand for the interface with a water layer of 0.0, 0.5, 1.0, 1.5, 2.0 Å, respectively. For 001 surface, all the five curves start to increase linearly. The maximum force is achieved for the water layer 0 Å, which is 313.4 $kcalmol^{-1}Å^{-1}$ at 5.4 Å shear displacement. After the maximum value of each curve, the shear force along x-direction gradually decreases with fluctuation. It can be found that the effect of water layer is significant for 001 surface since the overall shear force of 0 Å water layer is much higher than that of the other four interfaces. This indicates that the water molecules interdict the intralayer Calcium-Oxygen bonding between the globules. The shear force fluctuates over the displacement which is normal for molecular dynamics simulation.

According to Amonton's law of adhesion (Gao et al., 2004), the friction force F is divided into two parts: $F = \mu L + F_0$, the external normal force L multiplied by the friction coefficient μ and the internal force F_0 impacted by the adhesion between the surface. In this study, L continuously decreases due to the reduction of the contact surface in the globules interface; the internal force F_0 should initially increase because of bond stretching and then decrease due to bond broken. During any fluctuation stage of *F*, the generation and breakage of bonds in the interface both

happen. The shear force–displacement generally follows Amonton's law for individual curves. The simulation of the interfacial shearing clearly shows both the chemical interaction (i.e. bonding) and the physical interaction occurring at the interface between two globules for three surfaces. The shear stress τ can be determined

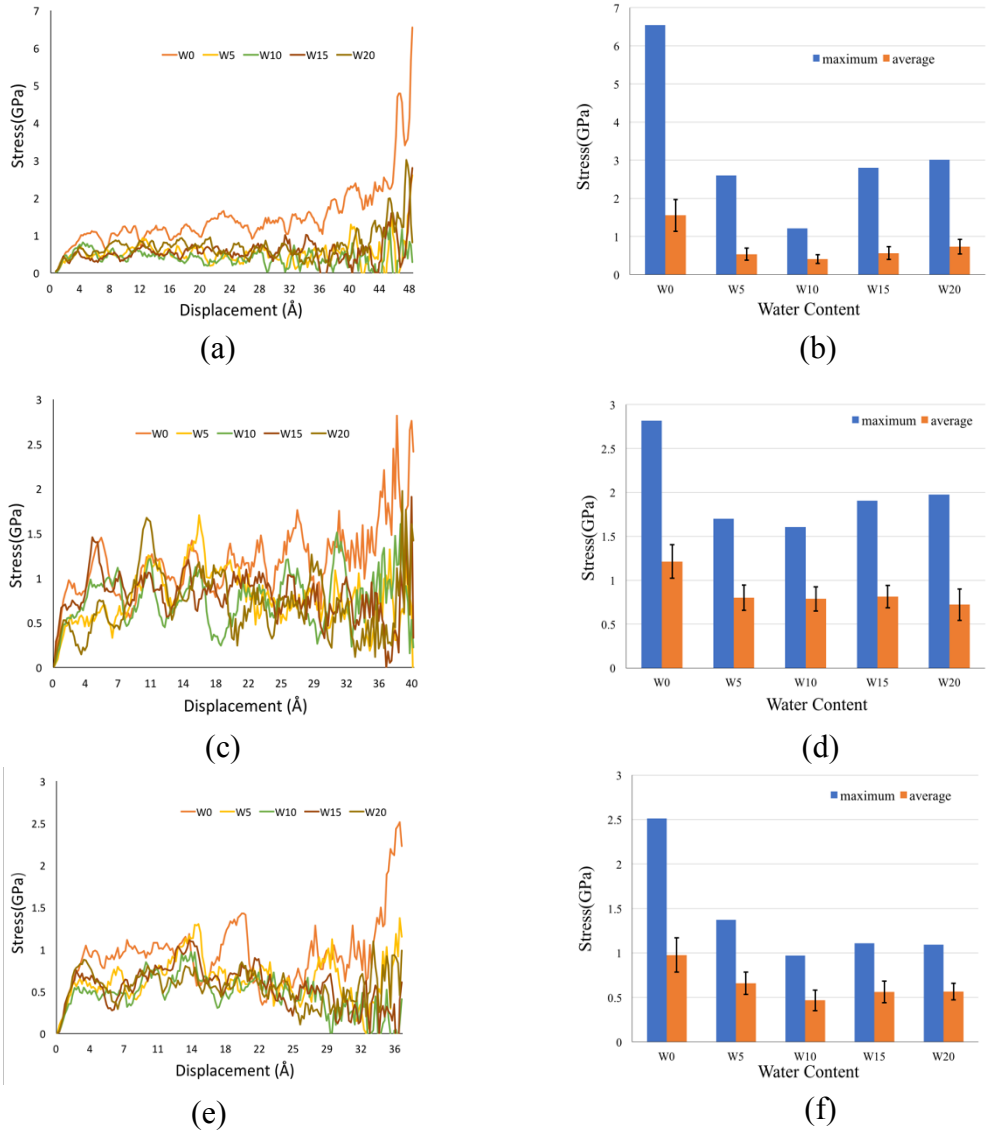

Figure 4.7 Stress-displacement curve for different water content in (a) (001) interface (c) (010) interface (e) (100) interface. Maximum value and average value of stress for each curve in (b) (001) interface (d) (010) interface (f) (100) interface.

as follows:

$$\tau = \frac{F}{A_{CSH-CSH}} = \frac{F}{a_0 \times (b_0 - \Delta b)} \quad (4\text{-}2)$$

where $A_{CSH\text{-}CSH}$ is the contact area between two C-S-H globules in the interface, a_0 is the length of C-S-H vertical to the shear direction, b_0 is the width of C-S-H along the shear direction and Δb is the shear distance of the moving C-S-H globule. For (001) surface, $a_0 = 43.43$ Å , $b_0 = 50.60$ Å, for (010) surface, $a_0 = 41.60$ Å , $b_0 = 32.43$ Å, and for (100) surface, $a_0 = 50.60$ Å, $b_0 = 41.60$ Å, respectively. By using Eq.4-2 and the values of a_0 and b_0 above, the shear stress can be calculated as a function of the displacement for each surface. Figure 4.7(a), (c) and (e) show the relationship between the shear stress and displacement and Figure 4.7(b) (d) and (f) present the maximum shear stress, average shear stress and error bars. The average stress is calculated after the first peak stress. In the shear stress-strain curves for all three interfaces, stresses all increase first and then fluctuate over certain values. Such a shearing mechanism of the interfaces can be simplified to a linear increase, followed by a constant development over the strain; or it may be called bi-linear stress-strain curves which can be easily implemented in FEM or DEM modelling. This yielding-like shearing behaviour after its peak stress is not commonly seen in macroscale shear stress development in cementitious materials, where the shear stress usually drops after its strength. It can be found out that the shear strength, i.e., the maximum shear stress, for any type of interfaces of the C-S-H globules, has the

highest value when no water layer exists. When water molecules are presented at the interfaces, however, the strength is reduced. Another interesting finding is the content of water molecules is not a very sensitive parameter. For example, the average stresses for W5, 10, 15 and 20 of all these interfaces are relatively the same, as shown in Figure 4.7(b), (d) and (f). The interfacial shear strength of C-S-H globules interface is then calculated by the average value of the stress for (001) surface with 0.5 Å, 1.0 Å, 1.5 Å and 2.0 Å water layer thickness to be about 560.29 ± 135.44 MPa; for (010) surface is about 780.63 ± 39.51 MPa; and for (100) surface, the shear strength is about 564.53 ± 78.33 MPa.

The shear stress-displacement curves, often know as bond-slip relation, for the C-S-H globule interfaces and the mechanical properties for C-S-H globules are derived for C-S-H which have been hardly seen in existing literature. It has significant impact on multi-scale modelling (either FEM or DEM) in terms of providing necessary inputs for the nanoscale C-S-H structures. These properties are usually not available due to difficulties in conducting experiments. This is why trial and error analysis is always applied for estimating the mechanical properties. The mechanical properties derived in this chapter can well be used for defining the bond-slip behaviour between the unit C-S-H globules as well as the constitutive relation for the globule itself.

4.6 Conclusions

In this chapter, the C-S-H globules and the interfaces between the C-S-H globules have been modeled at the atomic scale and the complete mechanism has been studied through MD simulations. Reaxff was used to provide the interactive potentials for the whole molecular system. Key material parameters, e.g., Young's modulus, strength and fracture energy, were determined for the globules and interfaces. It has been found that the atomic structure significantly affects the mechanical performance of the C-S-H structures. Longer mean chain lengths (i.e., Models III - V) tend to increase the strength of C-S-H and, more importantly, change the fracture behavior from brittle failure to ductile failure, along the silicate chains direction. In the direction normal to silicate chains, however, silicate chains do not play an important role while interlayer structure matters. Octahedral coordination of Calcium with oxygen atoms will result in stronger interactions and higher mechanical strengths in the normal direction. Moreover, pores (i.e., IGP) in the C-S-H globules can considerably reduce the strength of the globule structures in normal to silicate chain direction but the weakening effect becomes less significant in silicate chain direction. Further, the effects of water content at the interfaces between globules were investigated and the normal strength and the shear strength for the interfaces were determined. It has been found that, for all types of the interfaces, the interface with no extra water molecules has greatest tensile/shear strength, because of the destructive effect of water on the bond

generation between two C-S-H globules. However, it is interesting to find the strength is not very sensitive to the amount of water since different water content at the interfaces resulted in roughly similar mechanical performance. It can be concluded that the mechanical properties obtained in this chapter for C-S-H nanostructures and interfaces are highly complementary to the meso-scale modelling of C-S-H via granular mechanics, i.e., DEM, or continuum mechanics, i.e., FEM.

Chapter 5.
GO C-S-H Composite Properties

5.1 Introduction

In the molecular structure of GO cement nanocomposite, the GO is mixed and reacted with C-S-H gel. Alkhateb et al. (2013) is perhaps the first researcher investigating the microcosmic properties for GO cement using MD method. In their study, COMPASS force field was applied; a unit cell with a layer of GO in the middle in the C-S-H structure was constructed. A simple pull-out test was conducted for calculating the interfacial strength and energy. Nevertheless, the structure of C-S-H was not clear enough, and the full stress-strain curve was not shown which represents the complete stress transferring behaviour. For other similar GO composite MD simulations without C-S-H, Li and co-workers (Li et al., 2011) simulated the pull-out test of carbon nanotube polymer with MD and produced the full shear stress and displacement relation at the interface between the carbon nanotube and the polymer. Inadequately, in this model, all the atoms of the polymer matrix were fixed while the carbon nanotube was pulled out, which does not represent the real physical mechanism. Ding et al. (Ding et al., 2012) investigated the effects of GO sheets in Poly(vinyl alcohol)/GO composites by using MD; it is found that the oxidation degree of the GO sheet influenced the strength of interfacial binding characteristics between GO and the polymer. Liu et al. (Liu et al., 2015) examined the interfacial mechanical properties of wrinkled GO/polyethylene and GO/PMMA composites by pull-out test with MD, and it has been found that the pull-out velocity of the wrinkled GO sheet. Depends on the

previous MD study of GO composite, a GO sheet pull-out test is accomplished for studying the interfacial stress and energy transfer via MD method with a reasonable value of shear stress calculated on the nanoscale (Fan et al., 2017). Based on the previous MD research on GO related composites, it is possible to do further simulation of GO cement composites on nanoscale.

This chapter attempts to model the GO-cement nanocomposite and determine the elastic and fracture properties of the composite by molecular dynamics method. A novel method to produce multi-layer GO sheets in C-S-H structure is introduced. It is then followed by the simulation of the enhancement mechanism by adding GO in LAMMPS. Furthermore, the overall strength and fracture properties for the GO cement composite is calculated and the cracking bridging effects has been investigated in this chapter.

5.2 Methdology

The C-S-H structure imported in this study as cement to react with graphene oxide is provided by Richardson (2014), which has Ca/Si ratio lower than 1.4, and it is also a Tobermorite-based monoclinic structure but the mean length of silicate chains is 11 Å and the layer spacing is 14 Å. This structure matches with the general observations on crystalline calcium silicate hydrates (e.g. the coordination of Ca-O) and the existence of intraglobular pores (IGP) (Jennings, 2008). The GO structure in this chapter is

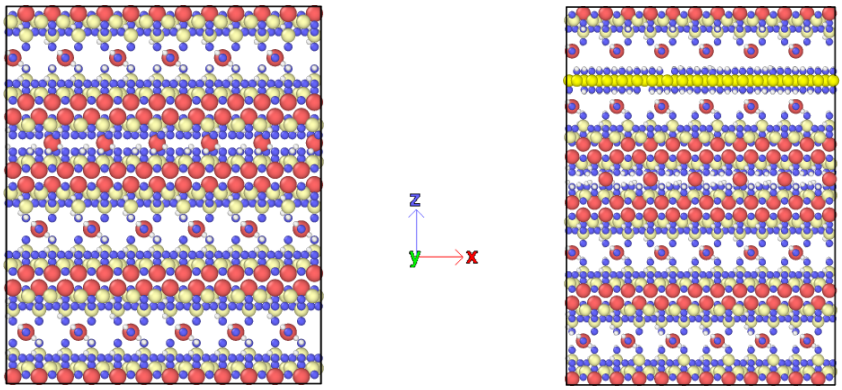

(a) (b)

Figure 5.1 The structure of (a) C-S-H duplicated from Richardson (2014) (b) single layer GO reinforced C-S-H

based on the Lerf-Klinowski GO model (Lerf et al., 1998), with the distortions neglected and the carbon plane structurally unaffected. In this model, the functional groups, including epoxy and hydroxyl, are distributed randomly (Mkhoyan et al., 2009) to avoid the energy reduction of GO sheet due to the gathering of the functional groups (Yan and Chou, 2010). Generally, the range of oxidation varies from a C/O ratio of 4:1 to 2:1 (Lahaye et al., 2009). The distribution of oxygen atoms is derived in (Dyer et al., 2015), which has been based on the density functional theory (DFT) analysis

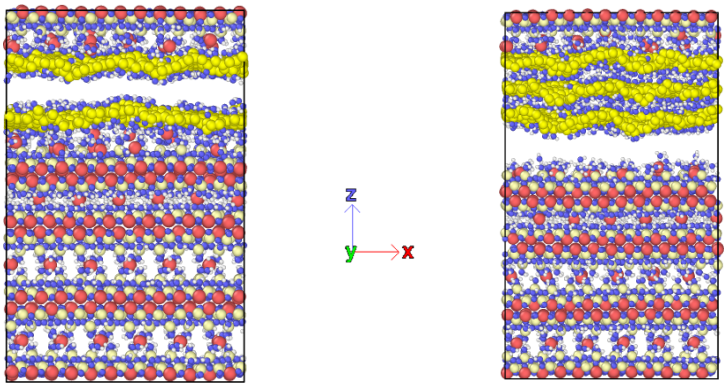

(a) (b)

Figure 5.2 The structure of C-S-H with multilayer GO sheets after equilibrium (a) two layers of GO sheets (b) three layers of GO sheets

performed in (Yan and Chou, 2010).

The molecular structure of C-S-H globule and one layer of GO sheet reinforced C-S-H is shown in Figure 5.1. C-S-H molecular structure with chemical formula $Ca_4H_2(Si_2O_7)_2Ca_4H_20$ with the lattice parameters of a = 11.35 Å, b = 7.3 Å, c = 21.5 Å is duplicated as 4 × 6 × 2 supercell along x-, y-, z- directions, respectively, and modified to the orthorhombic structure. The GO sheet is inserted in the intralaminar Calcium layer which is a natural cleavage plane (Manzano et al., 2017) and it is the weakest layer in this structure before under a tensile test to achieve a simulation box with the lattice parameters of a = 45.4 Å, b = 43.8 Å, c = 61.46 Å. To investigate the mechanical properties of C-S-H and GO reinforced C-S-H structure, the compression or tension tests along y- and z- direction are applied to all the structures. To study the effect of different layers of GO sheets on C-S-H structure, the GO sheets are adjusted the size to fit the size of C-S-H unit for the period boundary. Due to the interaction of GO (Dyer et al., 2015), the GO sheets would stay together when reacting with C-S-H. As shown in figure 5.2, one layer, two layers and three layers of GO sheets with C/A ratio of 3.2:1 are placed in the same cleavage plane for the z-compression and y-tensile tests.

LAMMPS (Plimpton, 1995) was used to perform the MD simulations. ReaxFF has been used in C-S-H structures (Manzano et al., 2012, Hou and Li, 2015), making it reasonable to model the GO cement. In general, ReaxFF can simulate the chemical

and physical interactions between Ca, Si, O, H atoms in the C-S-H gel and interface. The potential energy defined by the ReaxFF for the structures used in this chapter can be expressed as follows (Nielson et al., 2005):

$$E_{\text{system}} = E_{bond} + E_{over} + E_{under} + E_{val} + E_{tors} + E_{vdWalls} + E_{Coulomb} \quad (5\text{-}1)$$

where E_{bond} is bond energy, E_{over} is over coordination energy, Eunder is under coordination energy, Eval is valence angle energy, E_{tors} is torsion rotation energy, $E_{vdWaals}$ is van der Waals interaction energy and $E_{Coulomb}$ is coulomb interaction energy. The energy of per atom is calculated by defined potentials from neighbor atoms.

After the energy minimization of each structure, the simulation box is relaxed for 50 ps in the isobaric-isothermal ensemble (NPT) and coupled to zero external pressure in the x, y, z dimensions. The Nose-Hoover thermostat is used to keep the temperature at 300 K, and the Nose-Hoover barostat is used to maintain the pressure at p = 0 Pa. After the system reached equilibrium, the system was then subjected to the tensile test or compression test along z- or y-axis to achieve the strain-stress relation with a constant strain rate at 0.08 Å/ps. For the strain-stress relation along z-direction, the pressures in the x and y directions are kept at zero, and for the strain-stress relation along y-direction, the pressures in the x- and z-directions are kept at zero.

Moreover, for GO-containing structures, an extra relaxation with compression along z-direction is applied to eliminate the natural separation in the interface

between GO sheets and C-S-H structure. During this relaxation, a loading rate of 0.05 Å/ps is applied along the z-direction. In each stress-strain curve of all the composite structures, the stress stays zero for a short period before it goes up to its peak value. The occasion when the stress starts to increase from zero is chosen as the starting structure for the following mechanical tests. On this occasion, it is believed that the separation between the GO sheet and C-S-H is removed without incurring any additional stress. Accordingly, the thickness of the interface reduces from 7.9 Å, 17.8 Å and 25.0 Å, for the one, two and three layers of GO, respectively, to 7.2 Å, 13.5 Å and 20.3 Å.

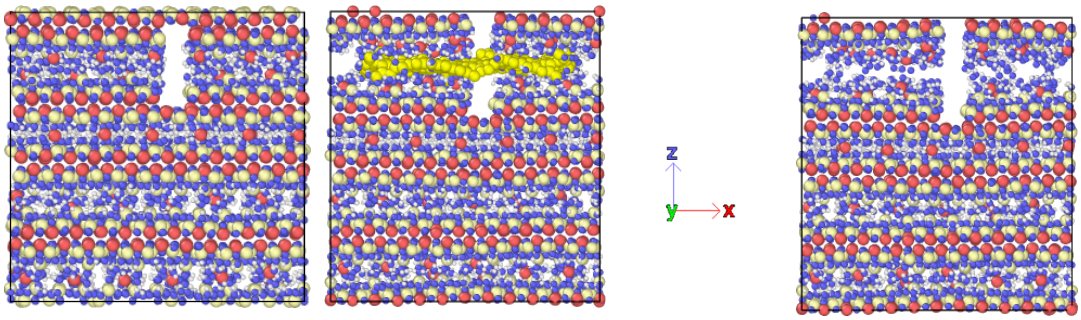

(a) (b) (c)

Figure 5.3 The structure cut with notch length of 10 Å (a) C-S-H globule (b) C-S-H with one layer GO sheet (c) C-S-H with vacuum later as interface

To investigate and determine the fracture properties of the C-S-H gel and the GO C-S-H composite, a notch with a width of 8 Å is made between 17 Å to 25 Å along y-axis in the C-S-H structure and the C-S-H composite with one layer of non-periodic GO sheet respectively. For each structure, four different lengths of notches are cut with lengths of 5 Å, 10 Å, 15 Å and 20 Å, as shown in Figure 5.3 The structure cut with

notch length of 10 Å (a) C-S-H globule (b) C-S-H with one layer GO sheet (c) C-S-H with vacuum later as interface.

5.3 Mechanical Properties of GO C-S-H Unit

5.3.1 Multilayer GO

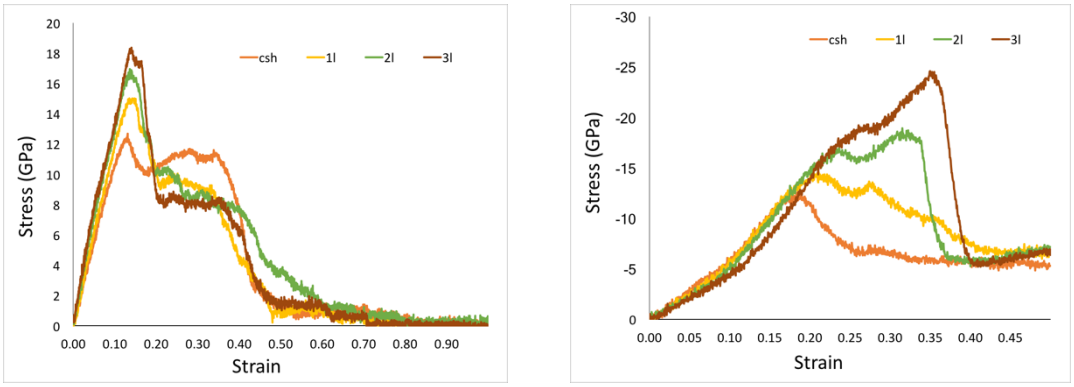

(a) (b)

Figure 5.4 The stress-strain curves of all C-S-H structures with further relaxation (a) under tensile test along y-direction (b) under compression test z-direction

The stress-strain curve of all periodic GO sheets reinforced C-S-H structures with further relaxation in this study during tensile test along y-direction and compression test along z-direction are shown in Figure 5.4, which shows the mechanical behavior of each structure during the mechanical process. The stress shown here is the pressure P on the boundary of the whole C-S-H structure, and $P = \frac{Nk_BT}{V} + \frac{\sum_i^{N'} r_i \cdot f_i}{dV}$, where N is the number of the atoms in the system, k_B is the Boltzmann constant, T is the temperature, d is the dimensionality of the system, V is volume, r_i and f_i are the

position and force vector of atom i. For y-direction tension, all the five structure present a linear increase in the elastic stage firstly in y-direction with different gradients. The structure of C-S-H globule indicates the smallest slope and the following structures are C-S-H with one layer GO, two layers GO structure, three layers GO structure and C-S-H with interface orderly. Unsurprisingly, the maximum strain of each curve maintains the same order mainly. For the C-S-H globule structure, the stress increases up to the maximum value of 12.67 GPa at a strain of around 0.13 $ÅÅ^{-1}$ after the linear increase. Following the maximum value, the stress directly reduces to 10.07 GPa at 0.18 $ÅÅ^{-1}$ and then turn into a yielding phase with a higher stress value around 11.04 GPa to 11.62 GPa until 0.35 $ÅÅ^{-1}$, which is the strongest yielding phase in the four structures. Because the breakage and generation of bonds are available with ReaxFF in C-S-H structure, as GO sheets interdict the bonds generation between molecules on two sides of the interlayers. The stress rapidly drops to 2.60 GPa at 0.44 $ÅÅ^{-1}$ with following slow decrease to 0 eventually. For the structure with one layer GO sheet, the maximum stress value of 15.02 GPa shows up at a strain of 0.15 $ÅÅ^{-1}$, then the stress decreases to 9.10 GPa at 0.21 $ÅÅ^{-1}$. Following is a rising yielding phase with a maximum stress of 9.8 GPa around 0.30 $ÅÅ^{-1}$, before the stress rapidly drops to 2.56 GPa at 0.48 $ÅÅ^{-1}$. The stress decreases to 0 slowly in the end as well. The structures with two layers and three layers of GO sheets presents more sufficient properties in y-direction. For two layers GO structure, the maximum value

of 16.86 GPa appears at 0.14 ÅÅ^{-1} following with the drop to 10.01 GPa at 0.20 ÅÅ^{-1}. After that the yielding phase continues with a decrease to 8.23 GPa at 0.27 ÅÅ^{-1} finishing with the stress drop to 2.25 GPa around 0.45 ÅÅ^{-1}. For three layers GO structure, the maximum stress reaches 18.35 GPa at 0.14 ÅÅ^{-1} after the initial linear increase. Following the maximum value, the stress directly reduces to 8.08 GPa at 0.21 ÅÅ^{-1} and then turn into a yielding phase with same value at 0.36 ÅÅ^{-1} end up with the stress drop to 2.06 GPa at 0.46 ÅÅ^{-1}. The stress of both multilayer GO cement structure then goes to 0 GPa ultimately.

For z-direction tension, four structure present a linear increase in the elastic stage firstly in y-direction with different gradients. In the initial increasing state, the structure of C-S-H globule indicates the largest slope and the following structures are C-S-H with one layer GO, two layers GO structure, three layers GO structure and C-S-H with interface orderly, which are reversed to the tensile test along y-direction. Interestingly, the mechanics after failure follows the reversed order with the increasing number of GO sheets. Compared to the C-S-H globule, there is a second peak shows up for the structure with GO sheet added. For single GO sheet reinforced C-S-H structure, the maximum compression stress happens at the first peak as the C-S-H globule. For multilayer GO sheets reinforced C-S-H structure, the maximum stress shows up at the second peak in the strain-stress curve. The reason and details of the properties are discussed in the following section.

5.3.2 Failure Evaluation

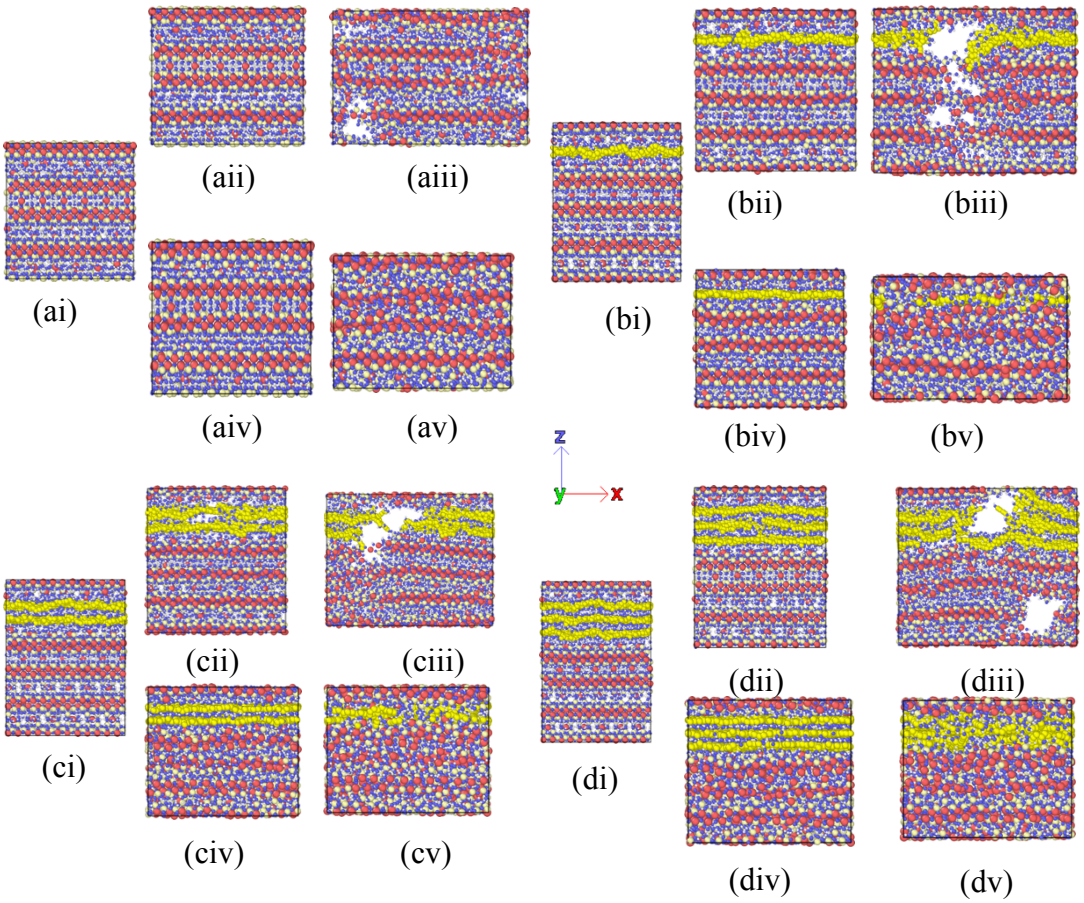

Figure 5.5 The tensile simulation and compression simulation on (a) C-S-H globule (b) C-S-H with one layer GO sheet (c) C-S-H with two layers GO sheet (d) C-S-H with three layer GO sheet for different moment: (i) the structure after equilibrium (ii) after the maximum stress along y-direction (iii) after failure happens along y-direction (iv) after the maximum stress along z-direction (v) after failure happens along z-direction

The morphology of the C-S-H globule and GO reinforced C-S-H structure with different numbers of GO sheets under tension simulation along y-direction and compression simulation along z-direction at five typical moments are shown in Figure 5.5. It is noted that the failure can be taken as an intrinsic feature of C-S-H gel's deformation at nanoscale (molecular dynamics study on the mode I fracture of

calcium silicate hydrate under tensile loading) so that it is worth to discuss how the GO sheets impact the failure of C-S-H at nanoscale. For all the structures under tension along y-direction, the failure happens where the silica chain broken after the maximum stress shows up in the second picture for each scenario. It can be seen that some local atoms adjusted with GO sheets broken at the same time just after the maximum stress happens from figure ii for each scenario, and this explains the reason that there is only one clear peak for each curve in Figure 5.4 (a). For the first scenario in Figure 5.5 (ai) to Figure 5.5 (aiii), the crack of C-S-H globule happens close to the right boundary of the simulation box. In contrast, the failure happens at the edge of the broken part of GO sheet in the structure with GO sheets added shown in Figure 5.5 (biii), Figure 5.5 (ciii) and Figure 5.5 (diii), and this is reason why the second drop happens for each structure in figure 5.4. Compared to all the chemical bonds in C-S-H gel (Hou et al., 2014a), the C-C bonds in GO sheet (Mkhoyan et al., 2009) present a much stronger binding effect which transfers through the interfacial connection to protect the C-S-H structure. For multilayer GO sheets C-S-H composites structure, disk-disk type molecular interaction between two graphene sheets (Dyer et al., 2015) provide a weaker capacity than the intrinsic interaction in the interior C-S-H gel, which causes the lower elastic properties in the interface later as the results of the lower initial slope in Figure 5.4 (b). From figure iv in each scenario, it can be seen that there is a time difference between the adjustment of

C-S-H structure and the breakage of GO sheets, which is the answer for two peaks in each curve in Figure 5.4 (b) with GO sheets added in the C-S-H interface. The more GO sheets added, the second peak reaches a higher value. Furthermore, there will not be any vacuum show up in compression test so that the stress will not reach 0 in the test.

5.4 Fracture Energy and Mechanical Properties

The mechanical properties of each scenario are discussed in this section. According to the demonstration presented by Petersson (1981), the fracture energy is calculated in this study, which is determined from the area under the stress-strain curves in figure 5.4. Young's modulus calculated by the stress-strain curve, maximum stress and fracture energy of each structure are shown in Table 5.2, and the error calculated of the results are also shown in the tables in brackets.

Table 5.1 Mechanics for tensile test along y-direction

Tension along y-direction	Young's modulus (GPa)	Stress maximum (GPa)	Fracture Energy (J/m2)
CSH	114.06	12.67	2.46
GO1l	128.62	15.02	2.27
GO2l	145.96	16.94	2.73
GO3l	156.86	18.37	2.46

- For the tensile simulation along y-direction, the young's modulus, maximum value of stress increase with the GO sheets added in the interface compared to the control

structure. In addition, young's modulus and maximum stress of the single layer of GO structure increase with the number of GO sheet layers increases, with 12.77%, 27.97% and 37.53% for Young's modulus respectively, and 18.53%, 33.68% and 44.95% for the maximum stress respectively. The multilayer GO sheets structures present better fracture properties and mechanical properties due to the stronger inherent bond connection in GO sheets compared to C-S-H structure which has been discussed before. The indistinctive strength of GO sheets turns up in fracture energy, because the GO sheets interdict the bonds generation between molecules in two sides of the interlayers during the yielding stage along y-direction tension.

Table 5.2 Mechanics for compression test along z-direction

Compression along z-direction	Young's modulus (GPa)	Stress maximum (GPa)	Fracture Energy (J/m2)
CSH	60.65	12.58	3.74
GO1l	47.13	14.57	4.96
GO2l	44.34	18.92	5.50
GO3l	42.50	24.60	6.28

For the results along z-direction, Young's modulus decreases with the GO sheets added in the interface compared to C-S-H globule, and the more GO sheets added, the less Young's modulus the structure has, but maximum stress and fracture energy increase with GO sheets added orderly. It need to be noticed that the fracture energy is calculated with the strain up to 0.5. GO sheets reduced the initial elastic stage of C-S-H

structure due to the weaker interfacial connection between GO sheets for a lower Young's modulus, and more layers it has, weaker properties it shows. After the GO sheets form as a flat plane from winkled by external pressure applied along z-direction, these sheets hold more stress than C-S-H structure to a higher stress performance so that the more GO sheets added in, the better fracture properties the structure has.

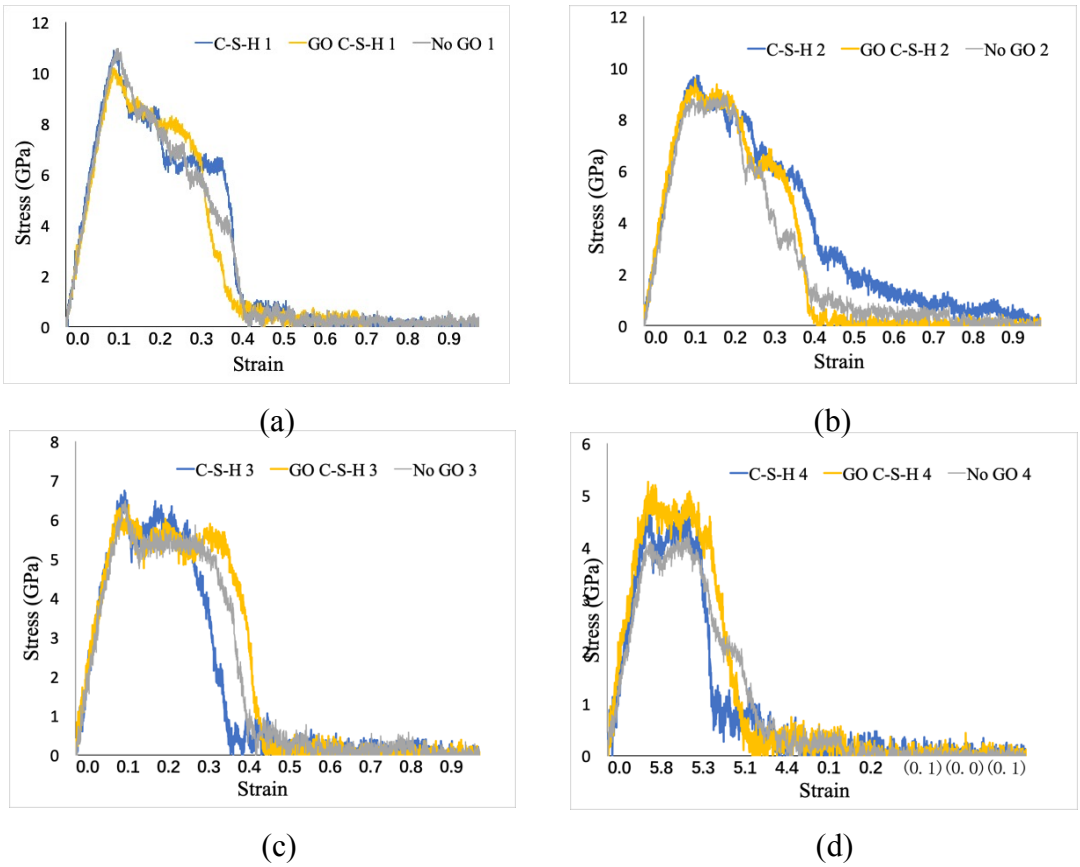

Figure 5.6 Stress-strain curves of C-S-H globule, one later GO sheet reinforced C-S-H and C-S-H interface under tensile test along y-direction with notch in length of (a) 5 Å (b) 10 Å (c) 15 Å (d) 20 Å

5.4.1 Fracture Properties

To achieve the impact of GO sheet on fracture properties of C-S-H structure, notches are cut in the structures of C-S-H globule (0l), one layer GO sheet reinforced C-S-H (1l)

and C-S-H interface without GO sheet (nc) with width of 8 Å, and different length of 5 Å, 10 Å, 15 Å and 20 Å. The stress-strain curves of those structures are presented in Figure 5.6. For the notch of 5 Å, all the three structures have the very similar Young's modulus as they have the same slope for the initial elastic stage. The stress of C-S-H globule and interface reaches 10.8 GPa and C-S-H with one layer GO sheet arrives 10.1 GPa at the strain of 0.11 ÅÅ^{-1}. With this small length of the notch, the structure of C-S-H globule presents the best mechanics during the yielding stage between a strain of 0.16 to 0.35 ÅÅ^{-1}, and all the structures are totally failed after 0.41 ÅÅ^{-1}. For the notch of 10 Å, C-S-H globule has best mechanics including Young's modulus, maximum stress and fracture energy, and C-S-H GO composite presents better mechanics than C-S-H interface unit. For the notch of 15 Å, the GO sheet starts to show its reinforcement on C-S-H on the nanoscale. The Young's modulus of C-S-H interface reveals the trend to decrease with the increase of the notch length, and the maximum stress shows up for C-S-H globule. C-S-H globule also has a yielding stage with a higher value but the C-S-H with GO sheet lasts longest for the stage. For the notch of 20 Å, C-S-H with GO sheet has best mechanics in the three structures that the reinforcement of GO sheet is obvious for a larger notch on the nanoscale of the C-S-H structure.

5.4.2 Failure Evaluation

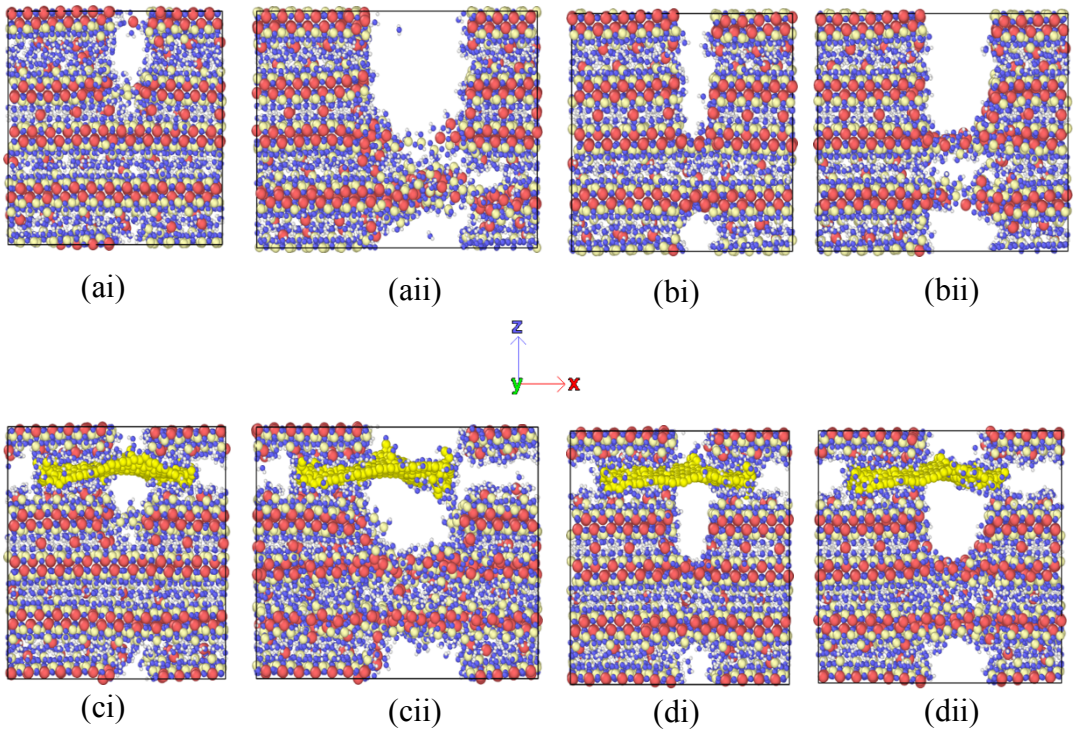

Figure 5.7 Different structures (a) C-S-H globule with 15 Å notch (b) C-S-H globule with 20 Å notch (c) C-S-H with one layer GO sheet with 15 Å notch (d) C-S-H with one layer GO sheet with 20 Å notch in two moments: (i) maximum stress happens (ii) after failure happens

The morphology of C-S-H globule and one layer GO reinforced C-S-H structure with 15 Å and 20 Å notch under tension simulation along y-direction at two typical moments are shown in Figure 5.7. The maximum stress of each structure with 15 Å notch at the strain of 0.1 Å/Å is shown in figure (ai) (ci), the moment after the failure of C-S-H globule/with GO where the strain of 0.4 Å/Å of each structure is shown in figure (aii) (cii). The maximum stress of each structure with 20 Å notch at the strain of 0.1 Å/Å is shown in figure (bi) (di), and the strain of 0.25 Å/Å of each structure is shown in figure (bii) (dii). It is obvious that the notch controls the fracture trend

compared to Figure 5.5. The GO sheet acts as bridge effect on the C-S-H structure in figure (cii) and (dii), which protects the parallel silica chains from being broken. Compare to the tensile test in last chapter, GO sheet also can also make up for the defect in C-S-H globule to enhance the interior mechanics in this scale. The fracture mechanics is not precise due to the shortage of silica layers, and the reinforcement of GO sheet on this scale depends on the pull-out effect which is verified in the former study (Fan et al., 2017).

5.4.3 Fracture Energy and Mechanical Properties

Table 5.3 and Figure 5.8 contains maximum stress and fracture energy of above scenarios calculated from Figure 5.6 is listed.

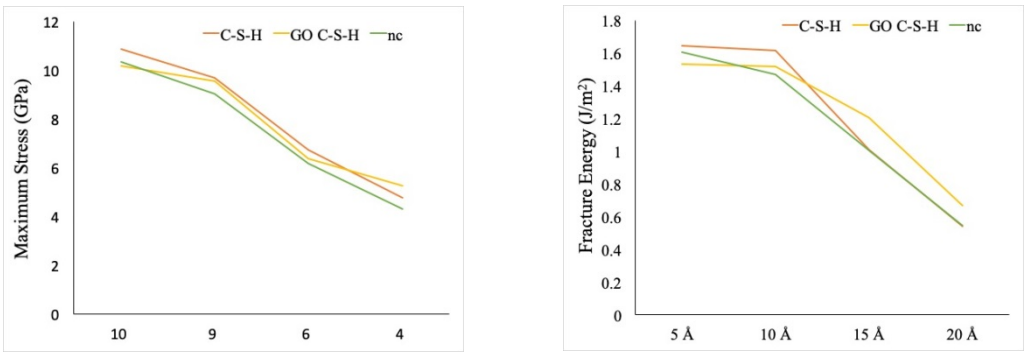

(a) (b)

Figure 5.8 Different mechanics for the fracture properties of tensile simulation along y-direction (a) Maximum stress (b) Fracture energy

Table 5.3 Mechanics for the fracture properties of tensile simulation along y-direction

Structure/Notch	5 Å	10 Å	15 Å	20 Å

	Maximum Stress (GPa)			
0l	10.88	9.71	6.74	4.78
1l	10.18	9.57	6.37	5.26
nc	10.35	9.04	6.19	4.29
	Fracture Energy (J/m^2)			
0l	1.65	1.98	1.01	0.54
1l	1.53	1.52	1.20	0.67
nc	1.60	1.47	1.00	0.55

For all the structures, mechanics including maximum stress and fracture energy for tensile simulation along y-direction, decrease with the length of the notch increases. For the maximum stress, each scenario with the same notch presents similar value, and GO sheet shows a modicum of superiority when the length of notch is 20 Å. The The enhancement of fracture energy with GO sheet added in the interface of C-S-H is incredible when the notch is longer than 5 Å, which is shown in Figure 5.8(c).

5.5 Conclusions

In this chapter, the unit composed of C-S-H and multi-layer GO sheets has been modeled and the overall strength and fracture mechanism has been studied using MD method. The structures for the multi-layer GO sheets and the C-S-H have been clearly presented, and tension and compression tests were carried out in a realistic manner. ReaxFF was employed to provide the interactive potentials for the whole molecular system. The full stress strain curves which represent tensile stress along

y-direction and compressive stress along z-direction indicate that the mechanical properties of GO cement composite increase with more layers of GO added in. It is found that the fracture mechanism of cement has been improved by GO sheets by the bridging effect on the nanoscale. The conclusion is made that MD simulation provides a comprehension in modelling the nanoscale mechanism of GO cement composite which have not been determined by experimental method yet.

Chapter 6. Experimental Study on GO-Cement Composite

6.1 Introduction

In this chapter, results of experimental investigation carried to study the effects of GO on the mechanical properties including Young's Modulus, flexural strength, fracture toughness and fracture energy of cement and cement/fly ash composites. At the meantime, the In-situ SEM are used to observe the morphology of the surfaces of these cementitious materials and present the process of failure clearly.

6.2 Experimental Setup

6.2.1 Materials

Graphene Oxide is produced by Graphena, the concentration of GO is 4 mg/ml. The chemical composition of GO is Carbon 49-56%, Hydrogen 0-1%, Nitrogen 0-1%, Sulfur 0-2%, Oxygen 41-50%.

6.2.2 Specimen Preparation

The Graphene oxide cement composite was prepared by mixing cement, water and GO. The dosage of GO is 0.00%, 0.02% and 0.035% by weight of composite. Water / composite weight ratio remained 0.4.

The cement / fly ash paste was prepared by mixing cement / fly ash, water and Go. Composite of cement / fly ash is mixed by the ratio of 1:1. The dosage of GO is 0.00%, 0.01%, 0.02%, 0.03%, 0.04%, 0.06%, 0.08% and 0.10% by weight of composite. Water / composite weight ratio remained 0.4.

For dispersion of GO in water, the bath sonicator is used for 30 minutes for each GO/water solution with different dosages of GO. Then the cement was added and

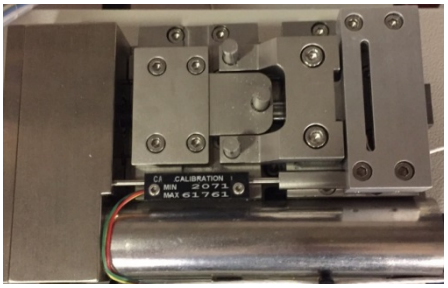

Figure 6.1 Three point bending mechine.

mixture was stirred. The resulting composite was immediately poured into a 6 mm × 10 mm × 40 mm mould for the three-point bending flexural strength test. After 24 hours settled in the chamber at the temperature of 20℃, the specimens were removed from the mould and cured in water and at 20℃ for 28 days. Because of the cement contraction in the first 24 hours in the mould, the size of final specimens for tests is approximately 5 mm × 10 mm × 39.5 mm.

6.2.3 In-situ SEM Test

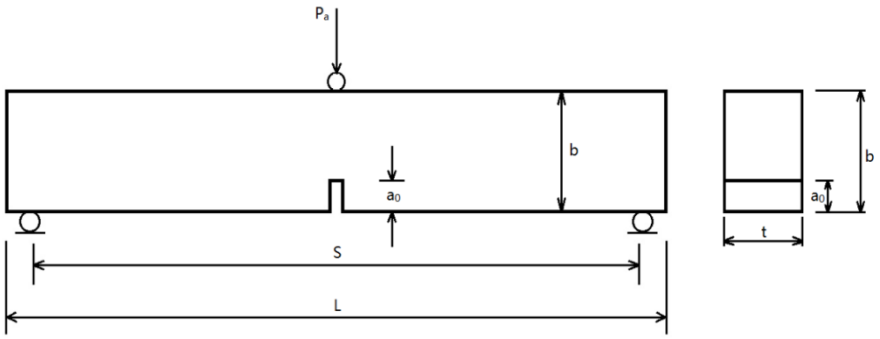

Figure 6.2 Scheme of the three-point bending test.

In-situ SEM (W-SEM) test was proceeded by a Tungsten Filament Scanning Electron Microscope with three-point bending test, shown in Figure 6.2. The dried cement GO composite pastes were stood to an aluminium stub and coated with gold by a sputtering process for good conductivity. For the three-point bending test, the distance S of two support columns is 30 mm, and the motor speed of the loading column is 0.05 mm/min. The scheme of three-point bending test is shown in Figure 6.2.

6.3 Calculation Method

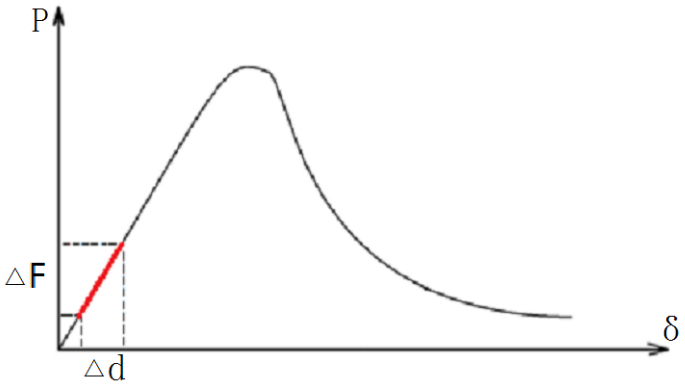

Figure 6.3 Load - deflection curve achieved from three-point bending test

The result achieved from three-point bending test is the force-elongation curve, which can be adjusted to load-deflection curve shown in Figure 6.3. With the top loading column goes forward slowly at a constant speed of 0.05 mm/min, the load P_a increases until the maximum flexural strength has happened and it is recorded all the time. During the three-point bending test, the whole process of the failure of a

specimen can be divided into three parts: Elastic deformation, plastic deformation and fracture. To calculate Young's modulus of each specimen, the elastic deformation process is the only applicable part, which is the straight line before the peak in load-deflection curve. Young's modulus, Y, is determined by the following formula:

$$Y = \frac{P_a S^3}{4t(b-a_0)^3 d} \tag{6-1}$$

Where P_a is the load, S is the distance between two support columns, t is the width of the specimen, b is the depth of the specimen, a_0 is the notch and d is the deflection of specimen.

In the elastic deformation, what can be achieved from the load – deflection curve is the relationship between force and displacement, which is measured as average slope, k, by:

$$k_i = \frac{\Delta F}{\Delta d} = \frac{\sum_n^m F_i}{\sum_n^m d_i} \tag{6-2}$$

Thus, Eq.6-1 can be fixed as:

$$Y_i = \frac{S^3}{4t(b-a_0)^3} * \frac{\sum_n^m F_i}{\sum_n^m d_i} = k_i \frac{S^3}{4t(b-a_0)^3} \tag{6-3}$$

The average Young's modulus is measured by:

$$Y_{average} = \frac{\sum_1^n Y_i}{n} \tag{6-4}$$

The flexural strength is measured by:

$$\sigma = \frac{3P_{max}S}{2t(b-a_0)^2} \quad (6\text{-}5)$$

Where P_{max} is the maximum load of each specimen recorded by three-point bending test,

The average Flexural strength is measured by:

$$\sigma_{average} = \frac{\sum_1^n F_i}{n} \quad (6\text{-}6)$$

The improvement on Young's modulus is measured by:

$$Y_{improvement} = \frac{Y_i\ average - Y_{0.00\ average}}{Y_{0.00\ average}} \times 100\% \quad (6\text{-}7)$$

And the improvement on Flexural strength is measured by:

$$\sigma_{improvement} = \frac{F_i\ average - F_{0.00\ average}}{F_{0.00\ average}} \times 100\% \quad (6\text{-}8)$$

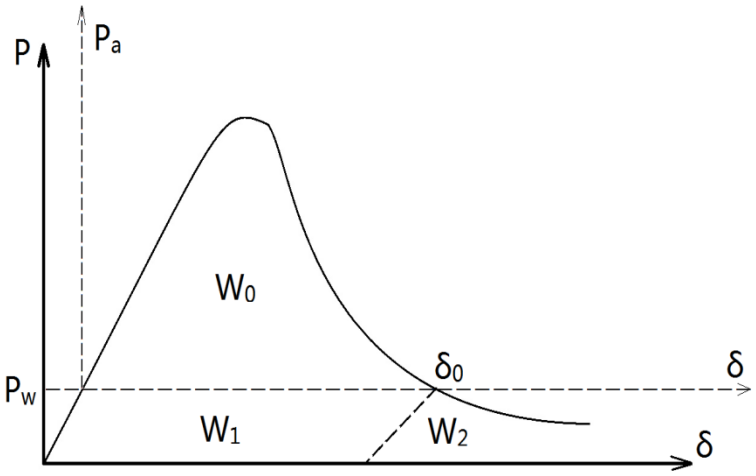

Figure 6.4 Load-deflection curve for calculation of fracture energy

The fracture energy G_F can be determined from the results achieved from the tensile test and the size of the specimen. Figure 6.4 Load-deflection curve for calculation of fracture energy

presents the schematic of the calculation of fracture energy, where P_w is the load which is equivalent to self-weight of the tested specimen, P_a is the external applied load which is the load measured and the sum of which equals the total load. W_0 is the area between curve P_a-δ and δ axis and $W_1 = P_w\delta_0$, where δ is the deflection. According to the demonstration presented by Petersson (Crack growth and development of fracture zones in plain concrete and similar materials. Division, Inst.), W_2 is approximately equivalent to W_1 The total fracture energy can be expressed as:

$$W_t = W_0 + W_1 + W_2 = W_0 + 2P_w\delta_0 \quad (6\text{-}9)$$

Thus, the fracture energy:

$$G_F = \frac{W_t}{A} = \frac{W_0 + 2P_w\delta_0}{A} \quad (6\text{-}10)$$

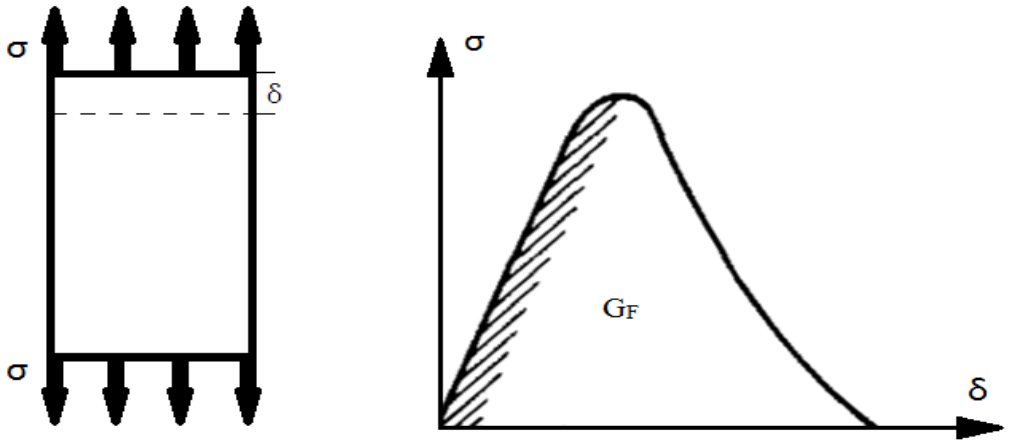

(a) (b)

Figure 6.5 (a) Scheme of a tensile test (b) The σ-δ Curve resulting from the test in (a)

Another method of estimating G_F directly is going to be treated briefly, which can be determined from the results in Figure 6.5 (a) Scheme of a tensile test (b) The σ-δ Curve resulting from the test in (a)

(a).

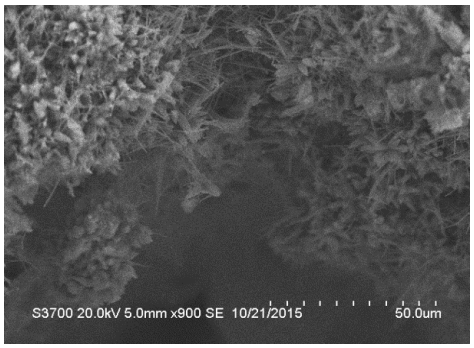

(a)

(b)

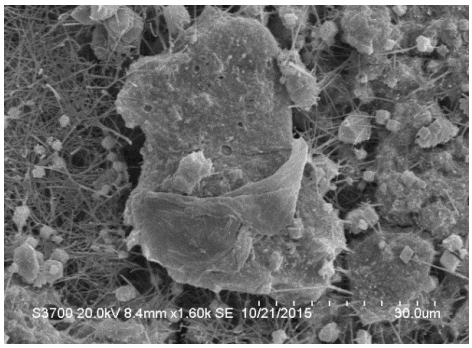

(c)

Figure 6.6 surface situation on (a) notch tip of 0.00% GO cement (b) 0.02% GO cement (c) 0.035% GO cement

After the maximum load is reached, the fracture zone begins to develop somewhere across the slash sectional area. All further deformation takes place in this fracture zone. G_F is then measured as the area under the σ-δ Curve in Figure 5.7(b) (Peterson, 1980).

6.4 Morphology of GO Cement Composites

The surfaces of the notches of 0.00% GO, 0.02% GO and 0.035% GO are shown in Figure 6.7. All the notches are relatively smooth inside and there's no binding in the

(a)

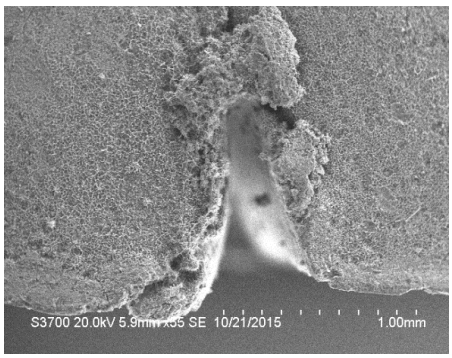

(b)

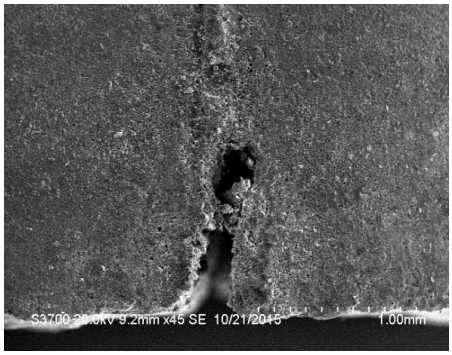

(c)

Figure 6.7 the view of notch (a) 0.00% of GO (b) 0.02% of GO (c) 0.035% of GO

notch. Compared to figure 4(a), there are more ettringite generates on the surface with the GO added, and in this scale various ettringite shows network formation.

The microscale view on specimens is shown in Figure 6.6. In Figure 6.6(a), it is the crack tip of the notch, around which there has the broken structure generated when notch has been made. In Figure 6.6(b), there are graphene oxide sheets holding

together and binding each other. In Figure 6.6(c), there is a piece of grouped graphene oxide on the surface with ettringite binding the edge. In Figure 6.6(b) and Figure 6.6(c), there is no similar flower or crystal formation as former studies. The reason why cement shows the rock-like surface on graphene oxide probably is the absence of Polycarboxylic superplasticizer. Polycarboxylic superplasticiser insures the graphene oxide spread across uniformly in the water, thus graphene oxide can be mixed with cement randomly and forms different crystalline shapes. However, there is lack of evidence to confirm Polycarboxylic superplasticiser has no effect on formation and properties of GO cement composite. Without polycarboxylic superplasticiser, different dosages of GO show the same formation when GO mixed in cement.

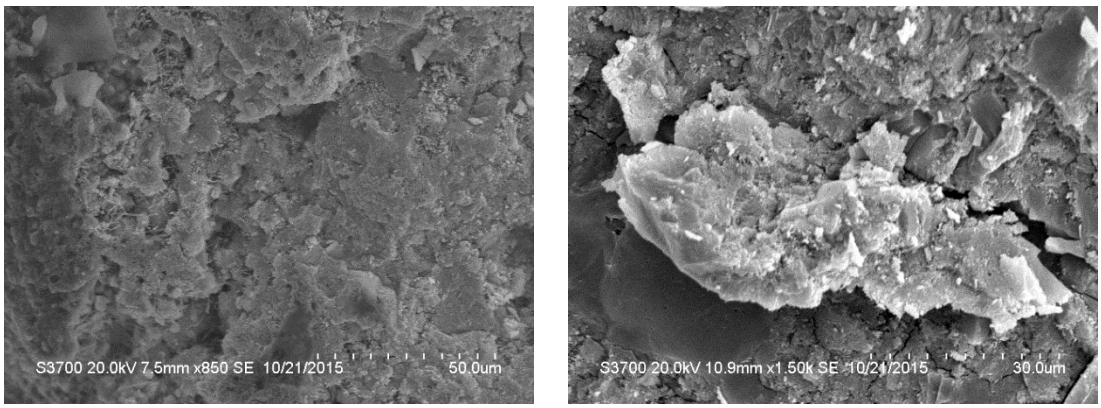

(a) (b)

Figure 6.8 the fracture surface on (a) 0.00% GO cement (b) 0.035% GO cement

The surface of the fracture plane is shown in Figure 6.8, it was caught after the fracture happened and coated with gold. In Figure 6.8(a), the fracture surface of 0.00% GO cement is shown. The surface is relatively smooth and presents a tight rock-like

structure with a little ettringite in the crack. The fracture surface of 0.035% GO cement is shown in Figure 6.8(b). There are some asperities, whose length is ranging from 3-5 micrometres to 30 micrometres, presented on the surface. It is reasonable to confirm it is the effect of GO, which means the asperities are produced by the interaction of C-S-H and GO. C-S-H prefers to generate around GO sheets due to the existing functional groups, and such functional groups offer a stronger binding by the covalent bond between oxygen in GO and calcium in cement (Pan et al., 2015). This structure of GO covered C-S-H somehow works as clinch materials in to enhance the performance of cement and provides higher Young's modulus and flexural strength compared to normal cement. This can be assumed by the strong young's modulus and strength of GO.

6.5 Mechanical Properties of GO Cement Composites

The results of the three-point bending test are shown in Table 6.1.

Table 6.1 dimensions of specimen and experimental results of GO cement.

	0.00a	0.00b	0.00c	0.00d	0.02a	0.02b	0.02c	0.02d	0.035 a	0.035 b	0.035 c	0.035 d
Slope (kN/m)	585	536	529	630	425	852	908	610	496	651	648	946
S (mm)	30	30	30	30	30	30	30	30	30	30	30	30
t (mm)	9.936	10.069	9.887	10.046	9.901	9.819	10.011	9.886	9.737	10.001	9.997	9.822
$b-a_0$ (mm)	3.289	3.232	3.187	3.151	3.181	3.420	3.452	3.264	3.128	3.284	3.303	3.413

Young's Modulus (Gpa)	11.17	10.65	11.17	13.53	9.01	14.64	14.89	11.98	11.24	12.41	12.13	16.36
Y Average (Gpa)	11.63				12.63				13.04			
improvement%					8.60				12.11			
Maximum load P_{max} (N)	19.56	22.27	20.35	22.81	19.34	33.17	26.30	18.44	17.42	28.46	28.66	29.65
Flexural Strength σ (Mpa)	8.19	9.53	9.12	10.29	8.68	13.00	9.92	8.31	8.23	11.87	11.83	11.66
σ Average (Mpa)	9.28				9.98				10.90			
Improvement %					7.50				17.40			

Because cement is a porous material and the tiny size of the specimen increase the errors, each group of different dosages of GO added have been tested for four times to reduce the errors by average calculation. By 0.02% GO added in cement, there is 8.60% improvement in Young's modulus and 7.50% improvement in flexural strength. By 0.035% GO added in cement, there is 12.11% improvement in Young's modulus and 17.40% improvement in flexural strength. This is a good evidence to verify the enhancement of GO on cement as a complementary result for former study on GO cement composite (Horszczaruk et al., 2015, Lv et al., 2014b).

6.6 Morphology of GO Cement Fly Ash Composites

As the morphology of the surface can be achieved in the in-situ SEM test when the load-deflection curve was recorded, the intuitionistic observation of the fracture can be gained during the failure happened in the cement/fly ash composite specimen.

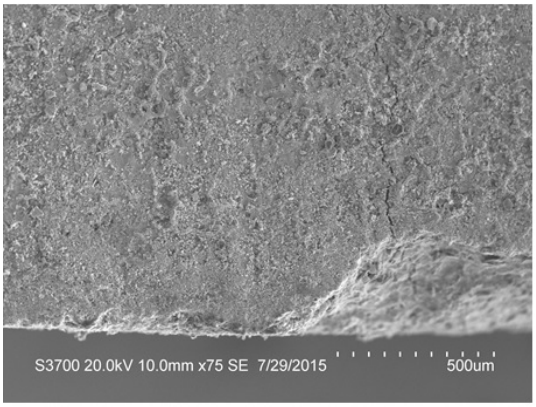

(a)

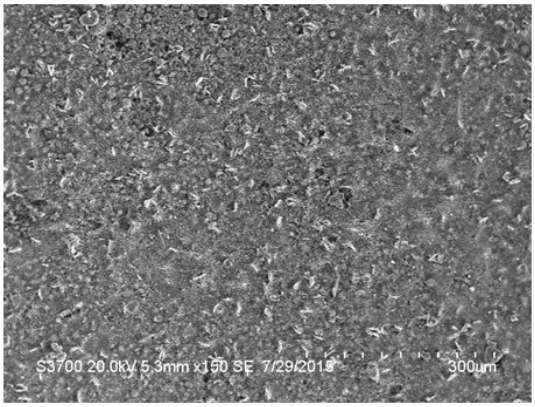

(b)

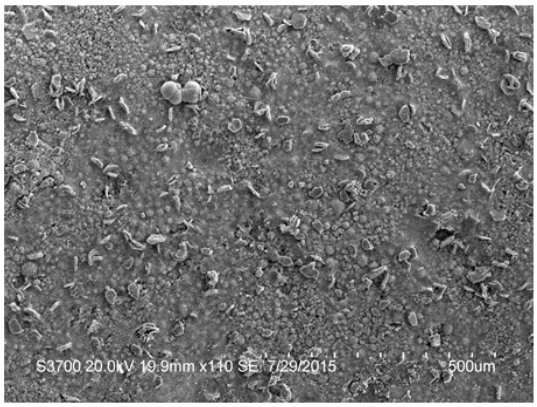

(c)

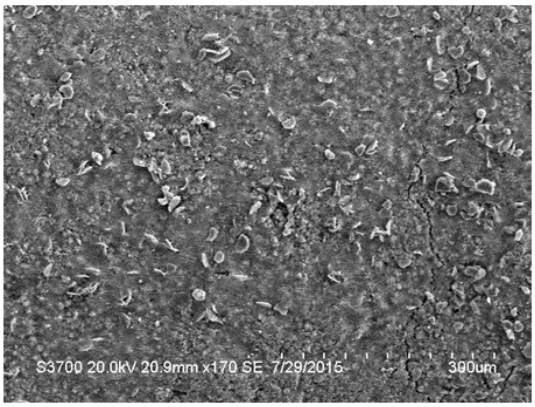

(d)

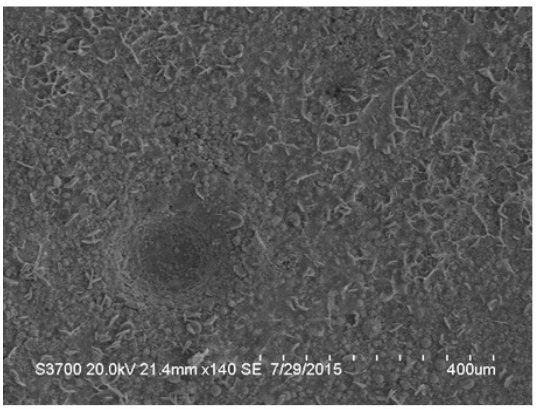

(e)

Figure 6.9 The surfaces of cement/fly ash composite with different dosages of GO: (a) 0.00% GO; (b) 0.01% GO; (c) 0.02% GO; (d) 0.03% GO; (e) 0.04% GO

Figure 6.9(a) – (e) shows the surfaces of five specimens with different dosages of GO that cement/fly ash composite without GO has a relatively levelled surface shown as Figure 6.9(a), the tiny white reflective tablets on the surfaces are cementitious material produced by GO which is covering GO sheet (C-S-H covering

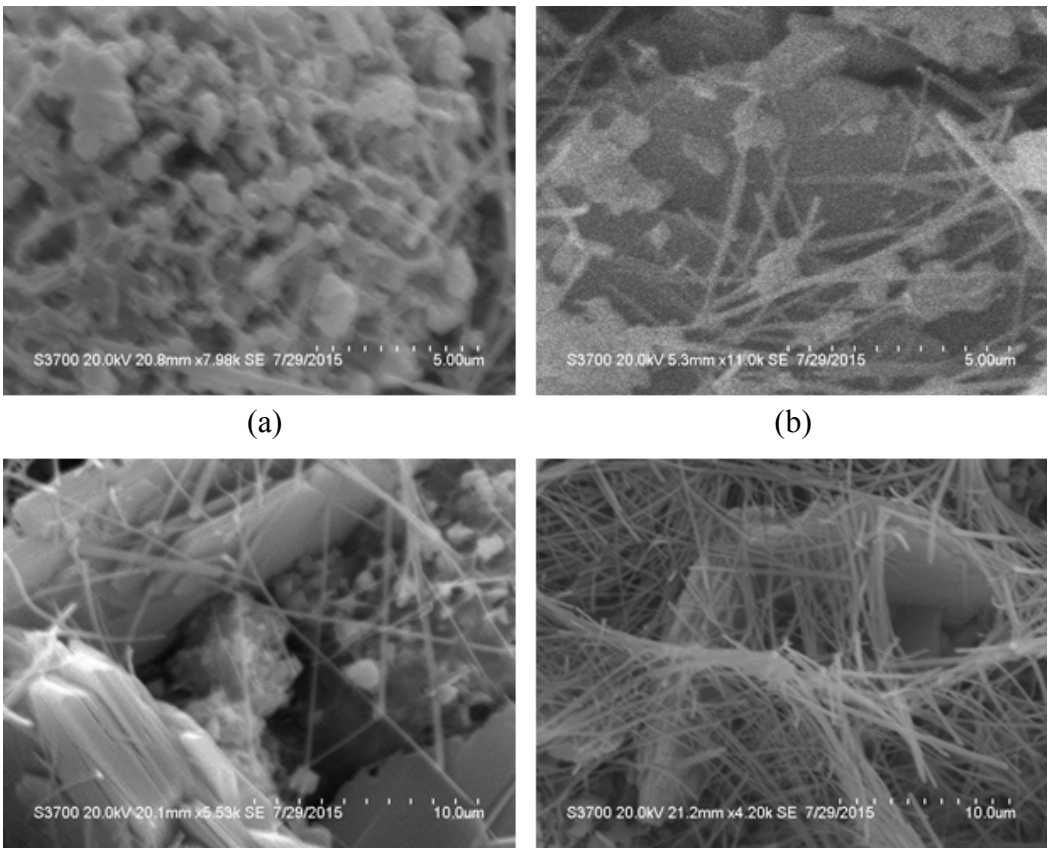

Figure 6.10 Microstructure of GO reinforced cement/fly ash composite with different GO dosages (a) 0.00% GO; (b) 0.01% GO; (c) 0.02% GO; (d) 0.04% GO.

GO). And the amount of the cementitious material from Figure 6.9(b) to Figure 6.9(d) increases obviously shows the rising quantity of GO. When it comes to Figure 6.9(e) of 0.04% GO of weight, the tablets covering GO seem to connect into flake.

To figure out microstructure of the tiny white cementitious material, the SEM images containing the details of it are shown in Figure 6.10 (a)-(d).

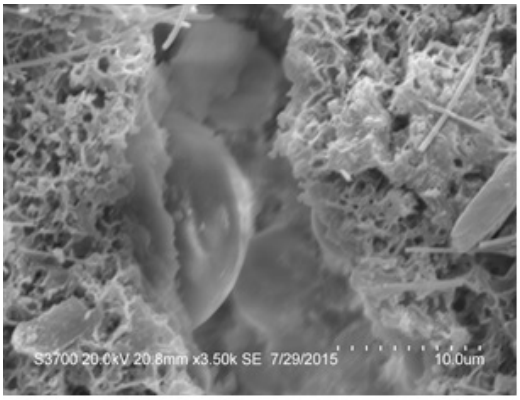

(a)

(b)

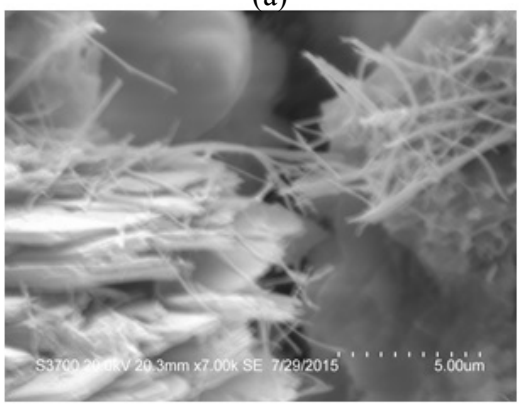

(c)

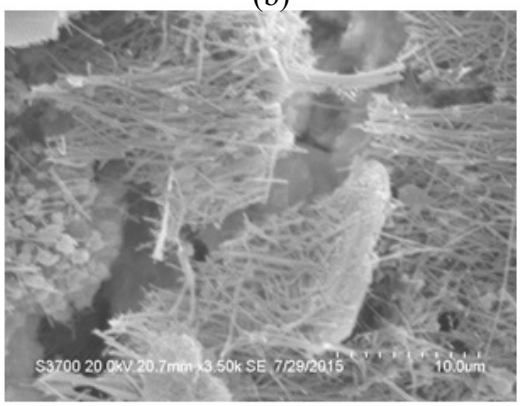

(d)

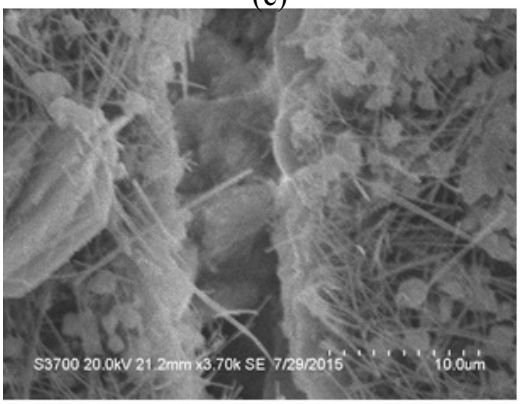

(e)

Figure 6.11 Fracture interface of GO reinforced cement/fly ash composite after failure happened with different GO dosages (a) 0.00% GO; (b) 0.01% GO; (c) 0.02% GO; (d) 0.03% GO; (e) 0.04% GO.

Compared to cement surface microstructure, more ettringite structure is formed on cement/fly ash composite. Figure 6.10(a) shows some rounded particle of fly ash; a piece of horizontal C-S-H covering GO sheet is shown in Figure 6.10 (b) with ettringite and small C-S-H/fly ash particle connected; Figure (c) shows vertical GO sheets covered C-S-H, and the C-S-H is formed to smooth layers. Some ettringite structure formed crossing the C-S-H covering GO sheets, but the other cement/fly ash structure shows no binding effect with C-S-H covering GO in Figure 6.10c). The connection of ettringite and C-S-H covering GO sheets and formation of ettringite around C-S-H covering GO sheets can also be observed in Figure 6.10 (d).

The fracture interfaces of the five specimens after failure happened are shown in Figure 6.11(a)-(e).

Some fly ash particles and coarse C-S-H particle are found in Figure 6.11(a). Figure 6.11(b) shows some cracked ettringite connected to C-S-H covering GO. Figure 6.11(c) provides clear images of C-S-H covering GO sheets keep it position on one side of crack and some of ettringite cracked from the connection with the other side, as well as one unbroken fly ash particle adheres on one side. Besides the cracked ettringite shown in Figure 6.11(d) and Figure 6.11(e), some intact GO sheets covered C-S-H were still connecting between two sides of fracture.

Figure 6.12 shows how a small crack expanded to failure in cement/fly ash composite with 0.03% dosage of GO. When the failure happened, all the ettringite connected between two sides of the crack broke to two parts, a flake of C-S-H covering GO sheet pulled out and stood above the middle of crack with ettringite connected and some unreacted fly ash particles shown up on one side of the crack.

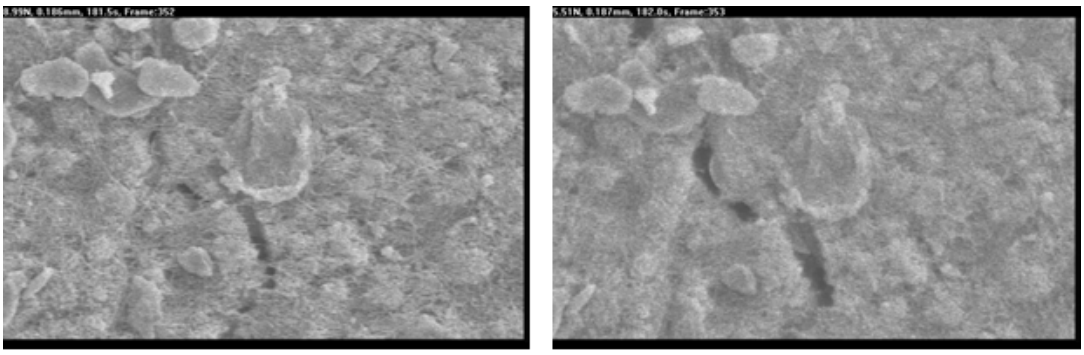

(a) (b)

(c) (d)

Figure 6.12 Procedure of fracture happened in cement/fly ash composite of 0.03%

6.7 Mechanical of GO Cement Fly Ash Composites

Table 6.2 The results of all the GO/fly ash cement sample on fracture toughness, fracture energy and flexural strength.

Sample	Fracture	Fracture	Flexural

	Toughness (Mpa*mm$^{1/2}$)	Energy (N/m)	Strength (MPa)
0.00a	71.21	218.52	5.45
0.00b	78.56	184.40	4.47
0.00c	49.93	115.73	4.07
0.00d	63.96	164.61	5.73
0.02a	60.23	198.90	4.79
0.02b	55.37	124.67	4.58
0.02c	43.18	202.31	3.61
0.02d	48.31	272.49	4.44
0.04a	56.29	229.21	4.38
0.04b	49.49	169.35	4.26
0.04c	50.6	173.67	4.03
0.04d	62.23	213.33	4.94
0.06a	57.61	163.41	4.93
0.06b	44.23	134.55	4.04
0.06c	41.65	168.72	4.48
0.06d	70.57	150.91	4.33
0.08a	54.29	157.11	4.95
0.08b	53.93	192.02	4.8
0.08c	42.27	133.64	3.98
0.08d	48.29	213.52	4.42
0.1a	48.25	267.07	4.12
0.1b	61.59	360.23	4.61
0.1c	65.66	181.76	4.95
0.1d	50.76	140.14	4.79

The average flexural strength of each dosage of GO calculated from the results in Table 6.2 is shown in Figure 6.13(a), and the reduction shows up in fracture strength with GO added. The trend is strange that with more GO added, the fracture increases but it still lower than the control sample with the GO added up to 0.10% of the total weight so that the minimum value happens when GO added with the minimum quantity of 0.02% of the total weight. The fracture toughness of the composite shows the similar trend with different GO added in the cement/fly ash composite. But GO do

enhances the fracture energy of cement/fly composite as shown in Figure 6.13(c), that with the dosages of GO increases, the fracture energy increases, and the maximum value of fracture energy happens when GO added with a maximum quantity of 0.10% of total weight.

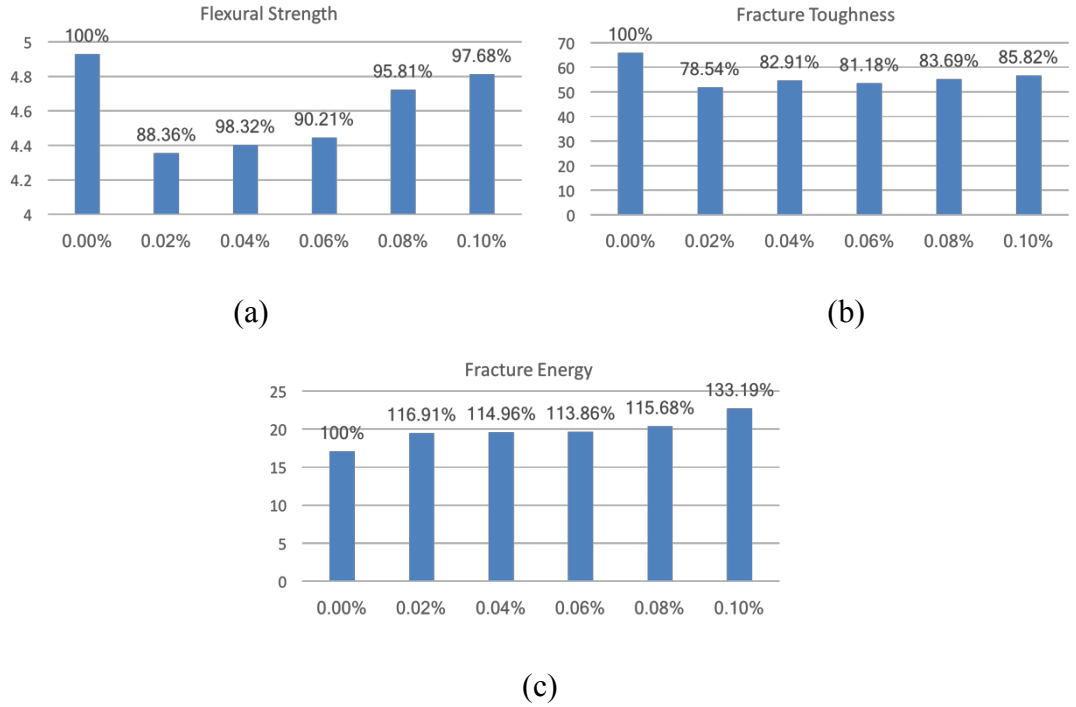

Figure 6.13 The average flexural strength of each dosages of GO/fly ash cement composites

6.8 Conclusions

The in-situ SEM test on cement and cement/fly ash composite with different dosages of GO range from 0.00% to 0.035% of weight and 0.00% to 0.1% respectively has been done in this research. For GO added in cement and cement/fly ash composite, two totally different characteristics have been shown in this chapter. In GO-cement

composite, GO sheets covered by C-S-H is hard to find on the surface of the clear morphology and GO enhanced cement a lot with a little bit of it added to the mixture. However, for cement/fly ash GO composite, it is easy to find where the GO sheets are on the surface of the composite; but it reduces the mechanics of cement/fly ash composite except the fracture energy. One of the possible reason for the phenomenon assumed to be that the GO sheets absorbed C-S-H and reduced the C-S-H locally, which let cement/fly ash composite trend to reduce its mechanical properties. Cement is enhanced a lot with a small quantity of GO added, but the cement/fly ash composited with GO has a weaker mechanical performance compared to cement/fly ash composite. This could be solved by chemical treatment or superplasticiser for better enhancement of GO on cementitious materials.

Chapter 7. Conclusions and Future Research

In this thesis, molecular dynamics method has mainly been used to simulate the cementitious materials and GO-cement nanocomposite at the nanoscale which is highly complementary to experimental research. The molecular structures, dynamics, mechanical and fracture properties have been investigated in different models in this thesis. Moreover, experimental tests about the mechanical and fracture properties of cementitious material containing GO, fly ash and cement have also been carried out. Specifically, the findings of this study are summarised as follows.

7.1 Conclusions

1. An MD simulation of the interface between the C-S-H and GO has been modelled and the complete stress transferring mechanism on the nanoscale. The structures for the GO and the C-S-H have been clearly presented, and pull-out tests were carried out in a realistic manner. Three different pulling rates were employed in running the MD simulations and it has been found that 0.08 Å ps-1 leads to larger fluctuation in the force-displacement curve, compared with 0.0016 Å ps-1 and 0.008 Å ps-1, especially for the later pulling out stage. The full stress-displacement curve which represents the mechanical properties of the GO cement interface has been derived and the shear strength has been found to be 647.58±91.18 MPa. For the first time, the shear stress-displacement curve has been derived for GO cement.

2. The C-S-H globules and the interfaces between the C-S-H globules have been modelled at the atomic scale and the complete mechanism has been studied through MD simulations. Key material parameters were determined for the globules and interfaces. It has been found that the atomic structure significantly affects the mechanical performance of the C-S-H structures. Longer mean chain lengths tend to increase the strength of C-S-H and change the fracture behaviour from brittle failure to ductile failure, along the silicate chains direction. Pores (i.e., IGP) in the C-S-H globules can considerably reduce the strength of the globule structures in normal to silicate chain direction but the weakening effect becomes less in silicate chain direction. Further, the effects of water content at the interfaces between globules were investigated and the normal strength and the shear strength for the interfaces were determined. However, the mechanical property of the interface is not very sensitive to the amount of water since different water content. Moreover, the weakest shear strength in the interface between C-S-H globules of 560.29 ± 135.44 MPa is found in this study.
3. Multi-layered GO C-S-H composites have been simulated in this study for the first time. For multi-layered GO sheets, GO sheets enhanced the tensile and compression strength of the C-S-H structure. It has been found that the more layers of GO sheets are added, the higher strength the composite has. Moreover, the GO

C-S-H composites have better fracture properties than the C-S-H structure on the nanoscale with larger notch size.

4. Without any further chemical treatment or any superplasticizer, GO can enhance some kinds of the cementitious materials on macroscale. For plain cement, the phenomenon that GO enhances it a lot with a small quantity is found in this study, but compared to the literature, morphology of GO cement composite is hard to be observed. On the other hand, GO reduces the mechanical properties of fly ash/cement composite, but the morphology of the composition can be observed clearly by SEM test. Compared to the literature, chemical treatment and superplasticizer are important for the properties of cementitious materials containing GO.
5. On the nanoscale, the enhancement of GO sheets on the C-S-H structure or cement can be explained that the shear stress of GO C-S-H structure is achieved as 647.58±91.18 MPa, and the shear stress of the interface between C-S-H globules is found as 560.29 ± 135.44 MPa with water contents. It is the fact that the fracture in cement happens at the weakest point in the interfaces between the globules so that the enhancement is obvious that GO sheets added in cement can improve the mechanical properties of the interface. And GO sheets also improve the fracture properties with the bridging effect.

7.2 Future Research

The ultimate goal of this study is to inform industry with better understood fracture properties and phenomenon of cementitious materials. However, there is a huge gap currently between the nanoscale properties obtained from MD simulation and the properties on macroscale. To figure the gap out, one possible solution is to build a largescale simulation, i.e., at the mesoscale. The largest structure built in this study is about 90 Å, and it is realistic to build a model in a much bigger size up to 40 nm or up to 100 nm, which could present a clearer observation and measurement of the interface in cementitious materials. Moreover, a multiscale modelling approach involving FEA together and the outcome from MD at the nanoscale will be a crucial solution to bridge the properties across scales.

Appendix

List of publications:

- Fan D, Lue L, Yang S. Molecular dynamics study of interfacial stress transfer in graphene-oxide cementitious composites[J]. Computational Materials Science, 2017, 139: 56-64.
- Duan, Z., Zhang, L., Lin, Z., Fan, D., Saafi, M., Castro Gomes, J., & Yang, S. (2018). Experimental test and analytical modeling of mechanical properties of graphene-oxide cement composites. Journal of Composite Materials, 0021998318760153.
- Fan D, and Yang S, "Mechanical properties of C-S-H globules and interfaces by molecular dynamics simulation", Construction and Building Materials, Volume 176, 10 July 2018, Pages 573–582.
- Fan D, Yang S, and Saafi, M, "A molecular dynamics study on graphene oxide cementitious nanocomposites", Scientific Report, in review.
- Fan D, Shangtong Yang, Experimental Determination of Fracture Toughness of Graphene-Oxide Fly Ash Cement. 2nd International Conference on mechanics of composites, Porto, Portugal, 11-14/07/2016
- Fan D, Shangtong Yang, Molecular Dynamics Model of Graphene-Oxide Reinforced Cement. 2nd International Conference on mechanics of composites, Porto, Portugal, 11-14/07/2016

References

AL-OSTAZ, A., WU, W., CHENG, A.-D. & SONG, C. 2010. A molecular dynamics and microporomechanics study on the mechanical properties of major constituents of hydrated cement. *Composites Part B: Engineering,* 41**,** 543-549.

ALKHATEB, H., AL-OSTAZ, A., CHENG, A. H.-D. & LI, X. 2013. Materials Genome for Graphene-Cement Nanocomposites. *Journal of Nanomechanics and Micromechanics,* 3**,** 67-77.

ALLEN, A. J., THOMAS, J. J. & JENNINGS, H. M. 2007. Composition and density of nanoscale calcium–silicate–hydrate in cement. *Nature materials,* 6**,** 311-316.

AYUELA, A., DOLADO, J., CAMPILLO, I., DE MIGUEL, Y., ERKIZIA, E., SÁNCHEZ-PORTAL, D., RUBIO, A., PORRO, A. & ECHENIQUE, P. 2007. Silicate chain formation in the nanostructure of cement-based materials. *The Journal of chemical physics,* 127**,** 164710.

BABAK, F., ABOLFAZL, H., ALIMORAD, R. & PARVIZ, G. 2014. Preparation and Mechanical Properties of Graphene Oxide: Cement Nanocomposites. *The Scientific World Journal,* 2014.

BAGRI, A., MATTEVI, C., ACIK, M., CHABAL, Y. J., CHHOWALLA, M. & SHENOY, V. B. 2010. Structural evolution during the reduction of chemically derived graphene oxide. *Nature chemistry,* 2**,** 581-587.

BAUCHY, M., LAUBIE, H., QOMI, M. A., HOOVER, C., ULM, F.-J. & PELLENQ, R.-M. 2015. Fracture toughness of calcium–silicate–hydrate from molecular dynamics simulations. *Journal of Non-Crystalline Solids,* 419**,** 58-64.

BENMOKRANE, B., CHAALLAL, O. & MASMOUDI, R. 1995. Glass fibre reinforced plastic (GFRP) rebars for concrete structures. *Construction and Building Materials,* 9**,** 353-364.

BERNARD, O., ULM, F.-J. & LEMARCHAND, E. 2003. A multiscale micromechanics-hydration model for the early-age elastic properties of cement-based materials. *Cement and Concrete Research,* 33**,** 1293-1309.

BONACCORSI, E., MERLINO, S. & TAYLOR, H. 2004. The crystal structure of jennite, Ca 9 Si 6 O 18 (OH) 6· 8H 2 O. *Cement and Concrete Research,* 34**,** 1481-1488.

BORESI, A. P., SCHMIDT, R. J. & SIDEBOTTOM, O. M. 1993. *Advanced mechanics of materials*, Wiley New York.

BRENNER, D. W., SHENDEROVA, O. A., HARRISON, J. A., STUART, S. J., NI, B. & SINNOTT, S. B. 2002. A second-generation reactive empirical bond order (REBO) potential energy expression for hydrocarbons. *Journal of Physics: Condensed Matter,* 14**,** 783.

BRUNAUER, S., KANTRO, D. & COPELAND, L. E. 1958. The stoichiometry of the hydration of β-dicalcium silicate and tricalcium silicate at room temperature. *Journal of the American Chemical Society,* 80**,** 761-767.

BURTON, D., LAKE, P. & PALMER, A. 2011. Properties and Application of Carbon Nanofibers (CNFs) Synthesized Using Vapor-Grown Carbon Fiber (VGCF) Manufacturing Technology. *Applied Sciences, Inc., Cedarville, OH* [Online]. Available: http://www.sigmaaldrich.com/materials-science/nanomaterials/carbon-nanofibers.html - appli.

CAI, W., PINER, R. D., STADERMANN, F. J., PARK, S., SHAIBAT, M. A., ISHII, Y., YANG, D., VELAMAKANNI, A., AN, S. J. & STOLLER, M. 2008. Synthesis and solid-state NMR structural characterization of 13C-labeled graphite oxide. *Science,* 321**,** 1815-1817.

CHEN, J., KOU, S.-C. & POON, C.-S. 2012. Hydration and properties of nano-TiO 2 blended cement composites. *Cement and Concrete Composites,* 34**,** 642-649.

CHUAH, S., PAN, Z., SANJAYAN, J. G., WANG, C. M. & DUAN, W. H. 2014. Nano reinforced cement and concrete composites and new perspective from graphene oxide. *Construction and Building Materials,* 73**,** 113-124.

CLAUSS, A., BOEHM, H. P. & HOFMANN, U. 1957. Untersuchungen über die adsorbierende und katalytisch wirksame Oberfläche der Ruße. *Zeitschrift für anorganische und allgemeine Chemie,* 290**,** 35-51.

CONG, X. & KIRKPATRICK, R. J. 1996. 29 Si MAS NMR study of the structure of calcium silicate hydrate. *Advanced Cement Based Materials,* 3**,** 144-156.

CONSTANTINIDES, G. & ULM, F.-J. 2004. The effect of two types of CSH on the elasticity of cement-based materials: Results from nanoindentation and micromechanical modeling. *Cement and concrete research,* 34**,** 67-80.

DIKIN, D. A., STANKOVICH, S., ZIMNEY, E. J., PINER, R. D., DOMMETT, G. H., EVMENENKO, G., NGUYEN, S. T. & RUOFF, R. S. 2007. Preparation and characterization of graphene oxide paper. *Nature,* 448**,** 457-460.

DING, N., CHEN, X., WU, C.-M. L. & LU, X. 2012. Computational investigation on the effect of graphene oxide sheets as nanofillers in poly (vinyl alcohol)/graphene oxide composites. *The Journal of Physical Chemistry C,* 116**,** 22532-22538.

DREYER, D. R., PARK, S., BIELAWSKI, C. W. & RUOFF, R. S. 2010. The chemistry of graphene oxide. *Chemical Society Reviews,* 39**,** 228-240.

DUAN, W. H., GONG, K. & WANG, Q. 2011. Controlling the formation of wrinkles in a single layer graphene sheet subjected to in-plane shear. *Carbon,* 49**,** 3107-3112.

DYER, T., THAMWATTANA, N. & JALILI, R. 2015. Modelling the interaction of graphene oxide using an atomistic-continuum model. *RSC Advances,* 5**,** 77062-77070.

FAN, D., LUE, L. & YANG, S. 2017. Molecular dynamics study of interfacial stress transfer in graphene-oxide cementitious composites. *Computational Materials Science,* 139**,** 56-64.

FELDMAN, R. & SEREDA, P. 1970. A new model for hydrated Portland cement and its practical implications. *Engineering Journal,* 53**,** 53-59.

FELDMAN, R. F. 1972. Factors affecting Young's modulus—porosity relation of hydrated Portland cement compacts. *Cement and Concrete Research,* 2**,** 375-386.

FENG, L. & CHRISTIAN, M. 2007. Micromechanics model for the effective elastic properties of hardened cement pastes. *Acta Materiae Compositae Sinica,* 24**,** 184-189.

FRENKEL, D. & SMIT, B. 2001. *Understanding molecular simulation: from algorithms to applications*, Elsevier.

GAO, J., LUEDTKE, W., GOURDON, D., RUTHS, M., ISRAELACHVILI, J. & LANDMAN, U. 2004. Frictional forces and Amontons' law: from the molecular to the macroscopic scale. ACS Publications.

GEIM, A. K., NOVOSELOV, K. S., YAZYEV, O. V., LOUIE, S. G., GHOSH, S., BAO, W., NIKA, D. L., SUBRINA, S., POKATILOV, E. P. & LAU, C. N. 2007. Nobel Prize for graphene. *Nature Materials,* 6**,** 183-192.

GONG, K., PAN, Z., KORAYEM, A. H., QIU, L., LI, D., COLLINS, F., WANG, C. M. & DUAN, W. H. 2014. Reinforcing effects of graphene oxide on Portland cement paste. *Journal of Materials in Civil Engineering,* 27.

GRAPHENEA 2014. Graphene Oxide. *In:* OXIDE, G. (ed.). Graphenea.

HAECKER, C.-J., GARBOCZI, E., BULLARD, J., BOHN, R., SUN, Z., SHAH, S. & VOIGT, T. 2005. Modeling the linear elastic properties of Portland cement paste. *Cement and Concrete Research,* 35**,** 1948-1960.

HAILE, J. M. 1992. *Molecular dynamics simulation: elementary methods*, Wiley New York.

HAMID, S. 1981. The crystal structure of the 11 Ä natural tobermorite Ca2. 25 [Si3O7. 5 (OH) 1.5]· 1H2O. *Zeitschrift für Kristallographie-Crystalline Materials,* 154**,** 189-198.

HE, H., RIEDL, T., LERF, A. & KLINOWSKI, J. 1996. Solid-state NMR studies of the structure of graphite oxide. *The Journal of physical chemistry,* 100**,** 19954-19958.

HOFMANN, U. & HOLST, R. 1939. Über die Säurenatur und die Methylierung von Graphitoxyd. *Berichte der deutschen chemischen Gesellschaft (A and B Series),* 72**,** 754-771.

HOOVER, W. G. 1985. Canonical dynamics: equilibrium phase-space distributions. *Physical review A,* 31**,** 1695.

HORSZCZARUK, E., MIJOWSKA, E., KALENCZUK, R. J., ALEKSANDRZAK, M. & MIJOWSKA, S. 2015. Nanocomposite of cement/graphene oxide–Impact on hydration kinetics and Young's modulus. *Construction and Building Materials,* 78**,** 234-242.

HOU, D. & LI, Z. 2015. Large-scale simulation of calcium silicate hydrate by molecular dynamics. *Advances in Cement Research,* 27**,** 278-288.

HOU, D., LI, Z. & ZHAO, T. 2015. Reactive force field simulation on polymerization and hydrolytic reactions in calcium aluminate silicate hydrate (C–A–S–H) gel: structure, dynamics and mechanical properties. *RSC Advances,* 5**,** 448-461.

HOU, D., MA, H., ZHU, Y. & LI, Z. 2014a. Calcium silicate hydrate from dry to saturated state: structure, dynamics and mechanical properties. *Acta materialia,* 67**,** 81-94.

HOU, D., ZHANG, J., LI, Z. & ZHU, Y. 2014b. Uniaxial tension study of calcium silicate hydrate (C–S–H): structure, dynamics and mechanical properties. *Materials and Structures*, 1-14.

HOU, D., ZHAO, T., WANG, P., LI, Z. & ZHANG, J. 2014c. Molecular dynamics study on the mode I fracture of calcium silicate hydrate under tensile loading. *Engineering Fracture Mechanics,* 131, 557-569.

HOU, D., ZHU, Y., LU, Y. & LI, Z. 2014d. Mechanical properties of calcium silicate hydrate (C–S–H) at nano-scale: a molecular dynamics study. *Materials Chemistry and Physics,* 146, 503-511.

INITIATIVE, C. S. 2002. The cement sustainability initiative: our agenda for action. *Geneva: World Business Council for Sustainable Development*.

JANIK, Y., KURDOWSKI, W., PODSIADLY, R. & SAMSETH, J. 2001. Fractal structure of CSH and tobermorite phases. *ACTA PHYSICA POLONICA SERIES A,* 100, 529-538.

JANSSENS, G. O., BAEKELANDT, B. G., TOUFAR, H., MORTIER, W. J. & SCHOONHEYDT, R. A. 1995. Comparison of cluster and infinite crystal calculations on zeolites with the electronegativity equalization method (EEM). *The Journal of Physical Chemistry,* 99, 3251-3258.

JEFF THOMAS, H. J. 2008. The Science of Cement and Concrete. Northwestern University.

JENNINGS, H. M. 2000. A model for the microstructure of calcium silicate hydrate in cement paste. *Cement and concrete research,* 30, 101-116.

JENNINGS, H. M. 2008. Refinements to colloid model of CSH in cement: CM-II. *Cement and Concrete Research,* 38, 275-289.

KIM, J., COTE, L. J., KIM, F., YUAN, W., SHULL, K. R. & HUANG, J. 2010. Graphene oxide sheets at interfaces. *Journal of the American Chemical Society,* 132, 8180-8186.

KNYAZEV, A. V. & LASHUK, I. 2007. Steepest descent and conjugate gradient methods with variable preconditioning. *SIAM Journal on Matrix Analysis and Applications,* 29, 1267-1280.

KOMARNENI, S., ROY, D. M., FYFE, C. A. & KENNEDY, G. 1987. Naturally occurring 1.4 nm tobermorite and synthetic jennite: Characterization by 27Al and

29Si MASNMR spectroscopy and cation exchange properties. *Cement and Concrete Research,* 17**,** 891-895.

LAHAYE, R., JEONG, H., PARK, C. & LEE, Y. 2009. Density functional theory study of graphite oxide for different oxidation levels. *Physical Review B,* 79**,** 125435.

LAU, T. T., KUSHIMA, A. & YIP, S. 2010. Atomistic simulation of creep in a nanocrystal. *Physical review letters,* 104**,** 175501.

LE ROUX, S. & PETKOV, V. 2010. ISAACS–interactive structure analysis of amorphous and crystalline systems. *Journal of Applied Crystallography,* 43**,** 181-185.

LEACH, A. R. 2001. *Molecular modelling: principles and applications*, Pearson education.

LEE, C., WEI, X., KYSAR, J. W. & HONE, J. 2008. Measurement of the elastic properties and intrinsic strength of monolayer graphene. *science,* 321**,** 385-388.

LERF, A., HE, H., FORSTER, M. & KLINOWSKI, J. 1998. Structure of graphite oxide revisited. *The Journal of Physical Chemistry B,* 102**,** 4477-4482.

LEROCH, S. & WENDLAND, M. 2012. Simulation of forces between humid amorphous silica surfaces: A comparison of empirical atomistic force fields. *The Journal of Physical Chemistry C,* 116**,** 26247-26261.

LI, G. Y., WANG, P. M. & ZHAO, X. 2005. Mechanical behavior and microstructure of cement composites incorporating surface-treated multi-walled carbon nanotubes. *Carbon,* 43**,** 1239-1245.

LI, Y., LIU, Y., PENG, X., YAN, C., LIU, S. & HU, N. 2011. Pull-out simulations on interfacial properties of carbon nanotube-reinforced polymer nanocomposites. *Computational Materials Science,* 50**,** 1854-1860.

LIU, F., HU, N., NING, H., LIU, Y., LI, Y. & WU, L. 2015. Molecular dynamics simulation on interfacial mechanical properties of polymer nanocomposites with wrinkled graphene. *Computational Materials Science,* 108**,** 160-167.

LV, S., LIU, J., SUN, T., MA, Y. & ZHOU, Q. 2014a. Effect of GO nanosheets on shapes of cement hydration crystals and their formation process. *Construction and Building Materials,* 64**,** 231-239.

LV, S., MA, Y., QIU, C., SUN, T., LIU, J. & ZHOU, Q. 2013. Effect of graphene oxide nanosheets of microstructure and mechanical properties of cement composites. *Construction and Building Materials,* 49**,** 121-127.

LV, S., TING, S., LIU, J. & ZHOU, Q. 2014b. Use of graphene oxide nanosheets to regulate the microstructure of hardened cement paste to increase its strength and toughness. *CrystEngComm,* 16**,** 8508-8516.

MAKAR, J. M. & CHAN, G. W. 2009. Growth of Cement Hydration Products on Single-Walled Carbon Nanotubes. *Journal of the American Ceramic Society,* 92**,** 1303-1310.

MANZANO, H., DOLADO, J. & AYUELA, A. 2009. Elastic properties of the main species present in Portland cement pastes. *Acta Materialia,* 57**,** 1666-1674.

MANZANO, H., DOLADO, J., GUERRERO, A. & AYUELA, A. 2007. Mechanical properties of crystalline calcium-silicate-hydrates: comparison with cementitious C-S-H gels. *physica status solidi (a),* 204**,** 1775-1780.

MANZANO, H., MASOERO, E., LOPEZ-ARBELOA, I. & JENNINGS, H. M. 2013. Shear deformations in calcium silicate hydrates. *Soft Matter,* 9**,** 7333-7341.

MANZANO, H., MOEINI, S., MARINELLI, F., VAN DUIN, A. C., ULM, F.-J. & PELLENQ, R. J.-M. 2012. Confined water dissociation in microporous defective silicates: mechanism, dipole distribution, and impact on substrate properties. *Journal of the American Chemical Society,* 134**,** 2208-2215.

MANZANO, H., MOHAMED, A. K., MISHRA, R. K. & BOWEN, P. 2017. A discussion on the paper "Role of porosity on the stiffness and stability of (001) surface of the nanogranular C–S–H gel". *Cement and Concrete Research,* 102**,** 227-230.

MEHANDZHIYSKI, A. Y., RICCARDI, E., VAN ERP, T. S., KOCH, H., ÅSTRAND, P.-O., TRINH, T. T. & GRIMES, B. A. 2015. DFT Study on the Interactions of Metal Ions with Long Chain Deprotonated Carboxylic Acids. *The Journal of Physical Chemistry A*.

MERLINO, S., BONACCORSI, E. & ARMBRUSTER, T. 2000. The real structures of clinotobermorite and tobermorite 9 Å: OD character, polytypes, and structural relationships. *European Journal of Mineralogy***,** 411-429.

MERLINO, S., BONACCORSI, E. & ARMBRUSTER, T. 2001. The real structure of tobermorite 11A: normal and anomalous forms, OD character and polytypic modifications. *European Journal of Mineralogy,* 13**,** 577-590.

MKHOYAN, K. A., CONTRYMAN, A. W., SILCOX, J., STEWART, D. A., EDA, G., MATTEVI, C., MILLER, S. & CHHOWALLA, M. 2009. Atomic and electronic structure of graphene-oxide. *Nano letters,* 9**,** 1058-1063.

MOON, J., YOON, S. & MONTEIRO, P. J. 2015. Mechanical properties of jennite: A theoretical and experimental study. *Cement and Concrete Research,* 71**,** 106-114.

MOOSAVI, M. & BAWDEN, W. F. 2003. Shear strength of Portland cement grout. *Cement and Concrete Composites,* 25**,** 729-735.

NIELSON, K. D., VAN DUIN, A. C., OXGAARD, J., DENG, W.-Q. & GODDARD, W. A. 2005. Development of the ReaxFF reactive force field for describing transition metal catalyzed reactions, with application to the initial stages of the catalytic formation of carbon nanotubes. *The Journal of Physical Chemistry A,* 109**,** 493-499.

NOSÉ, S. 1984. A unified formulation of the constant temperature molecular dynamics methods. *The Journal of chemical physics,* 81**,** 511-519.

ONUAGULUCHI, O., PANESAR, D. K. & SAIN, M. 2014. Properties of nanofibre reinforced cement composites. *Construction and Building Materials,* 63**,** 119-124.

PAN, Z., HE, L., QIU, L., KORAYEM, A. H., LI, G., ZHU, J. W., COLLINS, F., LI, D., DUAN, W. H. & WANG, M. C. 2015. Mechanical properties and microstructure of a graphene oxide–cement composite. *Cement and Concrete Composites,* 58**,** 140-147.

PARRINELLO, M. & RAHMAN, A. 1981. Polymorphic transitions in single crystals: A new molecular dynamics method. *Journal of Applied physics,* 52**,** 7182-7190.

PEIGNEY, A., LAURENT, C., FLAHAUT, E., BACSA, R. & ROUSSET, A. 2001. Specific surface area of carbon nanotubes and bundles of carbon nanotubes. *Carbon,* 39**,** 507-514.

PELISSER, F., NETO, A. B. D. S. S., LA ROVERE, H. L. & DE ANDRADE PINTO, R. C. 2010. Effect of the addition of synthetic fibers to concrete thin slabs on plastic shrinkage cracking. *Construction and building materials,* 24**,** 2171-2176.

PELLENQ, R. J.-M., KUSHIMA, A., SHAHSAVARI, R., VAN VLIET, K. J., BUEHLER, M. J., YIP, S. & ULM, F.-J. 2009. A realistic molecular model of

cement hydrates. *Proceedings of the National Academy of Sciences,* 106**,** 16102-16107.

PELLENQ, R. J.-M. & VAN DAMME, H. 2004. Why does concrete set?: The nature of cohesion forces in hardened cement-based materials. *Mrs Bulletin,* 29**,** 319-323.

PETERSON, P. 1980. Fracture energy of concrete: Method of determination. *Cement and Concrete research,* 10**,** 79-89.

PETERSSON, P.-E. 1981. *Crack growth and development of fracture zones in plain concrete and similar materials.* Division, Inst.

PLIMPTON, S. 1995. Fast parallel algorithms for short-range molecular dynamics. *Journal of computational physics,* 117**,** 1-19.

QIU, L., YANG, X., GOU, X., YANG, W., MA, Z. F., WALLACE, G. G. & LI, D. 2010. Dispersing carbon nanotubes with graphene oxide in water and synergistic effects between graphene derivatives. *Chemistry-A European Journal,* 16**,** 10653-10658.

RAKI, L., BEAUDOIN, J., ALIZADEH, R., MAKAR, J. & SATO, T. 2010. Cement and concrete nanoscience and nanotechnology. *Materials,* 3**,** 918-942.

REJMAK, P., DOLADO, J. S., STOTT, M. J. & AYUELA, A. S. 2012. 29Si NMR in cement: a theoretical study on calcium silicate hydrates. *The Journal of Physical Chemistry C,* 116**,** 9755-9761.

RICHARDSON, I. 1999. The nature of CSH in hardened cements. *cement and concrete research,* 29**,** 1131-1147.

RICHARDSON, I. 2004. Tobermorite/jennite-and tobermorite/calcium hydroxide-based models for the structure of CSH: applicability to hardened pastes of tricalcium silicate, β-dicalcium silicate, Portland cement, and blends of Portland cement with blast-furnace slag, metakaolin, or silica fume. *Cement and Concrete Research,* 34**,** 1733-1777.

RICHARDSON, I. & GROVES, G. 1992. Models for the composition and structure of calcium silicate hydrate (C S H) gel in hardened tricalcium silicate pastes. *cement and concrete research,* 22**,** 1001-1010.

RICHARDSON, I. & GROVES, G. 1993. Microstructure and microanalysis of hardened ordinary Portland cement pastes. *Journal of Materials science,* 28**,** 265-277.

RICHARDSON, I. G. 2014. Model structures for C-(A)-SH (I). *Acta Crystallographica Section B: Structural Science, Crystal Engineering and Materials,* 70**,** 903-923.

RUESS, G. 1946. Zur Wasserbindung im Halloysit. *Monatshefte für Chemie/Chemical Monthly,* 76**,** 168-173.

SCHOLZ, W. & BOEHM, H. 1969. Untersuchungen am graphitoxid. VI. Betrachtungen zur struktur des graphitoxids. *Zeitschrift für anorganische und allgemeine Chemie,* 369**,** 327-340.

SEDAGHAT, A., RAM, M. K., ZAYED, A., KAMAL, R. & SHANAHAN, N. 2014. Investigation of physical properties of graphene-cement composite for structural applications. *Open Journal of Composite Materials,* 2014.

SELVAM, R. P., SUBRAMANI, V. J., MURRAY, S. & HALL, K. D. 2009. Potential application of nanotechnology on cement based materials.

SHAHSAVARI, R., BUEHLER, M. J., PELLENQ, R. J. M. & ULM, F. J. 2009. First-principles study of elastic constants and interlayer interactions of complex hydrated oxides: Case study of tobermorite and jennite. *Journal of the American Ceramic Society,* 92**,** 2323-2330.

SHAHSAVARI, R., PELLENQ, R. J.-M. & ULM, F.-J. 2011. Empirical force fields for complex hydrated calcio-silicate layered materials. *Physical Chemistry Chemical Physics,* 13**,** 1002-1011.

SHAO, G., LU, Y., WU, F., YANG, C., ZENG, F. & WU, Q. 2012. Graphene oxide: the mechanisms of oxidation and exfoliation. *Journal of Materials Science,* 47**,** 4400-4409.

SHEN, X., LIN, X., YOUSEFI, N., JIA, J. & KIM, J.-K. 2014. Wrinkling in graphene sheets and graphene oxide papers. *Carbon,* 66**,** 84-92.

SIDDIQUE, R. & MEHTA, A. 2014. Effect of carbon nanotubes on properties of cement mortars. *Construction and Building Materials,* 50**,** 116-129.

STANKOVICH, S., DIKIN, D. A., DOMMETT, G. H., KOHLHAAS, K. M., ZIMNEY, E. J., STACH, E. A., PINER, R. D., NGUYEN, S. T. & RUOFF, R. S. 2006. Graphene-based composite materials. *Nature,* 442**,** 282-286.

SUZUKI, H., BAE, S. & KANEMATSU, M. 2016. Nanostructural deformation analysis of calcium silicate hydrate in portland cement paste by atomic pair distribution function. *Advances in Materials Science and Engineering,* 2016.

SWOPE, W. C., ANDERSEN, H. C., BERENS, P. H. & WILSON, K. R. 1982. A computer simulation method for the calculation of equilibrium constants for the formation of physical clusters of molecules: Application to small water clusters. *The Journal of Chemical Physics,* 76**,** 637-649.

TAYLOR, H. F. 1966. Chemistry of cements.

TAYLOR, H. F. 1986. Proposed structure for calcium silicate hydrate gel. *Journal of the American Ceramic Society,* 69**,** 464-467.

TAYLOR, H. F. 1997. *Cement chemistry*, Thomas Telford.

TRENS, P., DENOYEL, R. & GUILLOTEAU, E. 1996. Evolution of surface composition, porosity, and surface area of glass fibers in a moist atmosphere. *Langmuir,* 12**,** 1245-1250.

ULM, F.-J., CONSTANTINIDES, G. & HEUKAMP, F. 2004. Is concrete a poromechanics materials?—A multiscale investigation of poroelastic properties. *Materials and structures,* 37**,** 43-58.

VAN AARDT, J. & VISSER, S. 1975. Thaumasite formation: A cause of deterioration of Portland cement and related substances in the presence of sulphates. *Cement and Concrete Research,* 5**,** 225-232.

VAN DAMME, H. & GMIRA, A. 2006. Cement Hydrates. *Developments in Clay Science,* 1**,** 1113-1127.

VAN DUIN, A. C., DASGUPTA, S., LORANT, F. & GODDARD, W. A. 2001. ReaxFF: a reactive force field for hydrocarbons. *The Journal of Physical Chemistry A,* 105**,** 9396-9409.

VERLET, L. 1967. Computer" experiments" on classical fluids. I. Thermodynamical properties of Lennard-Jones molecules. *Physical review,* 159**,** 98.

WANG, Y., LI, V. C. & BACKER, S. 1990. Tensile properties of synthetic fiber reinforced mortar. *Cement and Concrete Composites,* 12**,** 29-40.

WU, W., AL-OSTAZ, A., CHENG, A. H.-D. & SONG, C. R. 2010. Concrete as a hierarchical structural composite material. *International Journal for Multiscale Computational Engineering,* 8.

WU, W., AL-OSTAZ, A., CHENG, A. H.-D. & SONG, C. R. 2011. Computation of elastic properties of Portland cement using molecular dynamics. *Journal of Nanomechanics and Micromechanics,* 1**,** 84-90.

YAN, J.-A. & CHOU, M. 2010. Oxidation functional groups on graphene: Structural and electronic properties. *Physical Review B,* 82**,** 125403.

YAN, Z. 2000. General thermal wavelength and its applications. *European Journal of physics,* 21**,** 625.

YAO, W., LI, J. & WU, K. 2003. Mechanical properties of hybrid fiber-reinforced concrete at low fiber volume fraction. *Cement and Concrete Research,* 33**,** 27-30.

YAZICI, Ş., İNAN, G. & TABAK, V. 2007. Effect of aspect ratio and volume fraction of steel fiber on the mechanical properties of SFRC. *Construction and Building Materials,* 21**,** 1250-1253.

YU, M.-F., LOURIE, O., DYER, M. J., MOLONI, K., KELLY, T. F. & RUOFF, R. S. 2000. Strength and breaking mechanism of multiwalled carbon nanotubes under tensile load. *Science,* 287**,** 637-640.

ZHANG, J. & JIANG, D. 2014. Molecular dynamics simulation of mechanical performance of graphene/graphene oxide paper based polymer composites. *Carbon,* 67**,** 784-791.

ZHU, Y., MURALI, S., CAI, W., LI, X., SUK, J. W., POTTS, J. R. & RUOFF, R. S. 2010. Graphene and graphene oxide: synthesis, properties, and applications. *Advanced materials,* 22**,** 3906-3924.